

The Vera C. Rubin Observatory Data Preview 1

VERA C. RUBIN OBSERVATORY TEAM,¹ TATIANA ACERO-CUELLAR ² EMILY ACOSTA ¹ CHRISTINA L. ADAIR ³
PRAKRUTH ADARI ⁴ JENNIFER K. ADELMAN-MCCARTHY ⁵ ANASTASIA ALEXOV ¹ RUSS ALLBERY ¹
ROBYN ALLSMAN,¹ YUSRA ALSAYYAD ⁶ JHONATAN AMADO ⁵ NATHAN AMOUROUX ⁷ PIERRE ANTILOGUS ⁸
ALEXIS ARACENA ALCAYAGA,⁹ GONZALO ARAVENA-ROJAS ⁹ CLAUDIO H. ARAYA CORTES,⁹ ÉRIC AUBOURG ¹⁰
TIM S. AXELROD ¹¹ JOHN BANOVETZ ¹² CARLOS BARRÍA,⁹ AMANDA E. BAUER ¹³ BRIAN J. BAUMAN,¹⁴
ELLEN BECHTOL ¹⁵ KEITH BECHTOL ^{1,16} ANDREW C. BECKER ¹⁷ VALERIE R. BECKER ¹⁸
MARK G. BECKETT ¹⁹ ERIC C. BELLM ²⁰ PEDRO H. BERNARDINELLI ²¹ FEDERICA BETTINA BIANCO ^{2,22,23}
ROBERT D. BLUM ¹⁸ JOANNE BOGART,²⁴ ADAM BOLTON ³ MICHAEL T. BOOTH,¹ JAMES F. BOSCH ⁶
ALEXANDRE BOUCAUD ²⁵ DOMINIQUE BOUTIGNY ⁷ ROBERT A. BOVILL,¹ ANDREW BRADSHAW,^{3,24}
JOHAN BREGEON ²⁶ MASSIMO BRESCIA ²⁷ BRIAN J. BRONDEL ²⁸ ALEXANDER BROUGHTON ²⁴
AUDREY BUDLONG ²⁹ DIMITRI BUFFAT,²⁶ RODOLFO CANESTRARI ³⁰ NEVEN CAPLAR ²⁰ JEFFREY L. CARLIN ¹
ROSS CEBALLO ¹⁸ COLIN ORION CHANDLER ^{31,20,32} CHIHWAY CHANG ³³ GLENAVER CHARLES-EMERSON,¹
HSIN-FANG CHIANG ³ JAMES CHIANG ²⁴ YUMI CHOI ³⁴ ERIC J. CHRISTENSEN ⁹ CHARLES F. CLAVER,¹
ANDY W. CLEMENTS,¹ JOSEPH J. COCKRUM,¹ JOHANN COHEN-TANUGI ³⁵ FRANCO COLLEONI,⁹ CÉLINE COMBET ²⁶
ANDREW J. CONNOLLY ²¹ JULIO EDUARDO CONSTANZO CÓRDOVA ⁹ HANS E CONTRERAS,⁹
JOHN FRANKLIN CRENSHAW ²¹ SYLVIE DAGORET-CAMPAGNE ³⁶ SCOTT F. DANIEL,²⁰ FELIPE DARUICH,⁹
GUILLAUME DAUBARD ⁸ GREG DAUES,³⁷ ERIK DENNIHY ¹ STEPHANIE J. H. DEPPE ¹⁸ SETH W. DIGEL ³
PETER E. DOHERTY,³⁸ CYRILLE DOUX ²⁶ ALEX DRLICA-WAGNER ⁵ GREGORY P. DUBOIS-FELSMANN ³⁹
FROSSIE ECONOMOU ¹ ORION EIGER ^{3,24} LUKAS EISERT ³ ALAN M. EISNER ⁴⁰ ANTHONY ENGLERT ⁴¹
BADEN ERB,⁹ JUAN A. FABREGA,⁹ PARKER FAGRELIUS,¹ KEVIN FANNING ³ ANGELO FAUSTI NETO ¹
PETER S. FERGUSON ^{21,16} AGNÈS FERTÉ ³ KRZYSZTOF FINDEISEN ²⁰ MERLIN FISHER-LEVINE ⁴²
GLORIA FONSECA ALVAREZ ³⁴ MICHAEL D. FOSS,³ DOMINIQUE FOCHEZ ⁴³ DAN C. FUCHS ³ SHENMING FU ²⁴
EMMANUEL GANGLER ⁴⁴ IGOR GAPONENKO,³ JULEN GARCIA ⁴⁵ JOHN H GATES,³ RANPAL K. GILL ²⁸
ENRICO GIRO ⁴⁶ THOMAS GLANZMAN ³ ROBINSON GODOY,⁹ IAIN GOODENOW,¹ MIRANDA R. GORSUCH ¹⁶
MICHELLE GOWER ³⁷ MELISSA L. GRAHAM ^{20,21} MIKAEL GRANVIK ^{47,48} SARAH GREENSTREET ³⁴ WEN GUAN ¹²
THIBAUT GUILLEMIN ⁷ LEANNE P. GUY ⁹ DIANE HASCALL,³ PATRICK A. HASCALL,³ AREN NATHANIEL HEINZE ²¹
FABIO HERNANDEZ ⁴⁶ KENNETH HERNER ⁵ ARDIS HERROLD,¹ CLARE R. HIGGS ¹⁸ JOSHUA HOBLITT ¹
ERIN LEIGH HOWARD ²⁰ MINHEE HYUN ⁹ AMANDA IBSEN,²⁸ PATRICK INGRAHAM ¹¹ DAVID H. IRVING ¹⁸
ŽELJKO IVEZIĆ ^{1,20} SUZANNE H. JACOBY,¹ BUELL T. JANNUZI ⁵⁰ SREEVANI JARUGULA ⁵ M. JAMES JEE ^{51,52}
TIM JENNESS ¹ TOBY C. JENNINGS ³ ANDREA JEREMIE ⁷ GARRETT JERNIGAN,^{53,*} DAVID JIMÉNEZ MEJÍAS,⁹
ANTHONY S. JOHNSON ³ R. LYNNE JONES ²⁰ ROGER WILLIAM LEWIS JONES ⁵⁴ CLAIRE JURAMY-GILLES ⁸
MARIO JURIĆ ²¹ STEVEN M. KAHN ⁵⁵ J. BRYCE KALMBACH ³ YIJUNG KANG ^{24,9} ARUN KANNAWADI ^{56,6}
JEFFREY P. KANTOR,¹ EDWARD KARAVAKIS ¹² KSHITIJ KELKAR ⁹ LEE S. KELVIN ⁶ SCOT J. KLEINMAN,⁵⁷
IVAN V. KOTOV,¹² GÁBOR KOVÁCS ²¹ MIKOLAJ KOWALIK ³⁷ VICTOR L. KRABBENDAM,¹ K. SIMON KRUGHOFF ^{1,*}
PETR KUBÁNEK ⁹ JACOB A. KURLANDER ²¹ MILE KUSULJA,²⁶ CRAIG S. LAGE ⁵² PAULO J. A. LAGO ²⁸
KATHERINE LALIOTIS ⁵⁸ TRAVIS LANGE ³ DIDIER LAPORTE,⁸ RYAN M. LAU ³⁴ JUAN CARLOS LAZARTE,³
QUENTIN LE BOULC'H ⁴⁹ PIERRE-FRANÇOIS LÉGET ⁶ LAURENT LE GUILLOU ⁸ BENJAMIN LEVINE ⁴ MING LIANG,¹
SHUANG LIANG,³ KIAN-TAT LIM ³ ANJA VON DER LINDEN ⁴ HUAN LIN ⁵ MARGAUX LOPEZ ³
JUAN J. LOPEZ TORO,⁹ PETER LOVE,⁵⁴ ROBERT H. LUPTON ⁶ NATE B. LUST ⁶ LAUREN A. MACARTHUR ⁶
SEAN PATRICK MACBRIDE ⁵⁹ GREG M. MADEJSKI,²⁴ GABRIELE MAINETTI ⁴⁹ STEVEN J. MARGHEIM ²⁸
THOMAS W. MARKIEWICZ ³ PHIL MARSHALL ³ STUART MARSHALL,²⁴ GUIDO MAULEN,⁹ SIDNEY MAU ⁵⁶
MORGAN MAY,^{60,12} JEREMY MCCORMICK ³ DAVID MCKAY ⁶¹ ROBERT MCKERCHER,¹ GUILLEM MEGIAS HOMAR ⁶²
AARON M. MEISNER ³⁴ FELIPE MENANTEAU,³⁷ HEATHER R. MENTZER ⁴⁰ KRISTEN METZGER,¹⁸
JOSHUA E. MEYERS ²⁴ MICHELLE MILLER,³⁴ DAVID J. MILLS,¹ JOACHIM MOEYENS ²¹ MARC MONIEZ,³⁶
FRED E. MOOLEKAMP ⁶³ C. A. L. MORALES MARÍN ⁹ FRITZ MUELLER ³ JAMES R. MULLANEY ⁶⁴
FREDDY MUÑOZ ARANCIBIA,¹ KATE NAPIER ²⁴ HOMER NEAL,³ ERIC H. NEILSEN, JR. ⁵ JEREMY NEVEU ³⁶
TIMOTHY NOBLE,⁶⁵ ERFAN NOURBAKHSH ⁶ KNUT OLSEN ³⁴ WILLIAM O'MULLANE ⁹ DMITRY ONOPRIENKO,³
MARCO ORIUNNO ³ SHAWN OSIER,³ RUSSELL E. OWEN,²⁰ AASHAY PAI ³³ JOHN K. PAREJKO ²⁰ HYE YUN PARK ⁵⁶

JAMES B. PARSONS,^{37,*} MARIA T. PATTERSON^{id},²⁰ MARINA S. PAVLOVIC^{id},⁹ KARLA PEÑA RAMÍREZ^{id},⁹
 JOHN R. PETERSON^{id},⁶⁶ STEPHEN R. PIETROWICZ^{id},³⁷ ANDRÉS A. PLAZAS MALAGÓN^{id},^{3,24} REBEKAH POLEN,⁵⁶
 HANNAH MARY MARGARET POLLEK,³ PAUL A. PRICE^{id},⁶ BRUNO C. QUINT^{id},¹ JOSÉ MIGUEL QUINTERO MARIN,⁹
 MARKUS RABUS^{id},⁶⁷ BENJAMIN RACINE^{id},⁴³ VELJKO RADEKA,¹² MANON RAMEL,²⁶ ARIANNA RANABHAT^{id},⁶⁸
 ANDREW P. RASMUSSEN^{id},²⁴ DAVID A. RATHFELDER,⁶⁹ MEREDITH L. RAWLS^{id},^{20,21} SOPHIE L. REED^{id},⁶
 KEVIN A. REIL^{id},³ DAVID J. REISS,²⁰ MICHAEL A. REUTER^{id},¹ TIAGO RIBEIRO^{id},¹ MICKAEL RIGAULT^{id},⁷⁰
 VINCENT J. RIOT^{id},¹⁴ STEVEN M. RITZ^{id},⁴⁰ MARIO F. RIVERA RIVERA,⁹ BRANT E. ROBERTSON^{id},⁷¹
 WILLIAM ROBY^{id},³⁹ GABRIELE RODEGHIERO^{id},⁷² AARON ROODMAN^{id},²⁴ LUCA ROSIGNOLI^{id},^{73,72} CÉCILE ROUCELLE^{id},²⁵
 MATTHEW R. RUMORE^{id},¹² STEFANO RUSSO,⁸ ELI S. RYKOFF^{id},²⁴ ANDREI SALNIKOV^{id},³ BRUNO O. SÁNCHEZ^{id},⁴³
 DAVID SANMARTIM^{id},⁹ CLARE SAUNDERS^{id},⁶ RAFE H. SCHINDLER,²⁴ SAMUEL J. SCHMIDT^{id},⁵² JACQUES SEBAG,⁹
 NIMA SEDAGHAT^{id},²⁰ BRIAN SELVY,¹ EDGARD ESTEBAN SEPULVEDA VALENZUELA,⁹ GONZALO SERICHE^{id},⁹
 JACQUELINE C. SERON-NAVARRETE^{id},⁹ IGNACIO SEVILLA-NOARBE^{id},⁷⁴ ALYSHA B. SHUGART^{id},⁹ JONATHAN SICK^{id},^{75,1}
 CRISTIÁN SILVA^{id},⁹ MATHEW C. SIMS^{id},⁷⁶ JALADH SINGHAL^{id},³⁹ KEVIN BENJAMIN SIRUNO,⁹ COLIN T. SLATER^{id},²⁰
 BRIANNA M. SMART^{id},²⁰ ADAM SNYDER^{id},⁵² CHRISTINE SOLDAHL,³ IOANA SOTUELA ELORRIAGA^{id},⁹ BRIAN STALDER^{id},¹
 HERNAN STOCKEBRAND^{id},⁹ ALAN L. STRAUSS^{id},¹⁸ MICHAEL A. STRAUSS^{id},⁶ KRZYSZTOF SUBERLAK^{id},²⁰
 IAN S. SULLIVAN^{id},²⁰ JOHN D. SWINBANK^{id},^{77,6} DIEGO TAPIA^{id},⁹ ALESSIO TARANTO^{id},^{72,73} DAN S. TARANU^{id},⁶
 JOHN GREGG THAYER^{id},³ SANDRINE THOMAS^{id},¹⁸ ADAM J. THORNTON^{id},¹ ROBERTO TIGHE,⁹
 LAURA TORIBIO SAN CIPRIANO,⁷⁴ TE-WEI TSAI^{id},¹ DOUGLAS L. TUCKER^{id},⁵ MAX TURRI,³ J. ANTHONY TYSON^{id},⁵²
 ELANA K. URBACH^{id},⁷⁸ YOUSUKE UTSUMI^{id},⁷⁹ BRIAN VAN KLAVEREN,³ WOUTER VAN REEVEN^{id},⁹
 PETER ANTHONY VAUCHER^{id},³ PAULINA VENEGAS^{id},²⁸ APRAJITA VERMA^{id},⁸⁰ ANTONIA SIERRA VILLARREAL^{id},³
 STELIOS VOUTSINAS^{id},¹ CHRISTOPHER W. WALTER^{id},⁵⁶ YUANKUN (DAVID) WANG^{id},²¹ CHRISTOPHER Z. WATERS^{id},⁶
 CHRISTINA C. WILLIAMS^{id},³⁴ BETH WILLMAN^{id},⁸¹ MATTHIAS WITTGEN^{id},³ W. M. WOOD-VASEY^{id},⁸² WEI YANG^{id},³
 ZHAOYU YANG^{id},¹² BRIAN P. YANNY^{id},⁵ PETER YOACHIM^{id},²⁰ TIANQING ZHANG^{id},⁸² CONGHAO ZHOU^{id},⁴⁰ AND
 DANICA ŽILKOVÁ^{id},²⁸

¹ Vera C. Rubin Observatory Project Office, 950 N. Cherry Ave., Tucson, AZ 85719, USA

² Department of Physics and Astronomy, University of Delaware, Newark, DE 19716-2570, USA

³ SLAC National Accelerator Laboratory, 2575 Sand Hill Rd., Menlo Park, CA 94025, USA

⁴ Department of Physics and Astronomy, Stony Brook University, Stony Brook, NY 11794, USA

⁵ Fermi National Accelerator Laboratory, P. O. Box 500, Batavia, IL 60510, USA

⁶ Department of Astrophysical Sciences, Princeton University, Princeton, NJ 08544, USA

⁷ Université Savoie Mont-Blanc, CNRS/IN2P3, LAPP, 9 Chemin de Bellevue, F-74940 Annecy-le-Vieux, France

⁸ Sorbonne Université, Université Paris Cité, CNRS/IN2P3, LPNHE, 4 place Jussieu, F-75005 Paris, France

⁹ Vera C. Rubin Observatory, Avenida Juan Cisternas #1500, La Serena, Chile

¹⁰ Université Paris Cité, CNRS/IN2P3, CEA, APC, 4 rue Elsa Morante, F-75013 Paris, France

¹¹ Steward Observatory, The University of Arizona, 933 N. Cherry Ave., Tucson, AZ 85721, USA

¹² Brookhaven National Laboratory, Upton, NY 11973, USA

¹³ Yerkes Observatory, 373 W. Geneva St., Williams Bay, WI 53191, USA

¹⁴ Lawrence Livermore National Laboratory, 7000 East Avenue, Livermore, CA 94550, USA

¹⁵ Wisconsin IceCube Particle Astrophysics Center, University of Wisconsin—Madison, Madison, WI 53706, USA

¹⁶ Department of Physics, University of Wisconsin-Madison, Madison, WI 53706, USA

¹⁷ Amazon Web Services, Seattle, WA 98121, USA

¹⁸ Vera C. Rubin Observatory/NSF NOIRLab, 950 N. Cherry Ave., Tucson, AZ 85719, USA

¹⁹ Institute for Astronomy, University of Edinburgh, Royal Observatory, Blackford Hill, Edinburgh EH9 3HJ, UK

²⁰ University of Washington, Dept. of Astronomy, Box 351580, Seattle, WA 98195, USA

²¹ Institute for Data-intensive Research in Astrophysics and Cosmology, University of Washington, 3910 15th Avenue NE, Seattle, WA 98195, USA

²² Data Science Institute, University of Delaware, Newark, DE 19717 USA

²³ Joseph R. Biden, Jr., School of Public Policy and Administration, University of Delaware, Newark, DE 19717 USA

²⁴ Kavli Institute for Particle Astrophysics and Cosmology, SLAC National Accelerator Laboratory, 2575 Sand Hill Rd., Menlo Park, CA 94025, USA

²⁵ Université Paris Cité, CNRS/IN2P3, APC, 4 rue Elsa Morante, F-75013 Paris, France

²⁶ Université Grenoble Alpes, CNRS/IN2P3, LPSC, 53 avenue des Martyrs, F-38026 Grenoble, France

²⁷ Department of Physics "E. Pancini", University Federico II of Napoli, Via Cintia, 80126 Napoli, Italy

²⁸ Vera C. Rubin Observatory/NSF NOIRLab, Avenida Juan Cisternas #1500, La Serena, Chile

²⁹ University of Washington, Dept. of Physics, Box 351580, Seattle, WA 98195, USA

³⁰ INAF Istituto di Astrofisica Spaziale e Fisica Cosmica di Palermo, Via Ugo la Malfa 153, 90146, Palermo, Italy

- ³¹LSST Interdisciplinary Network for Collaboration and Computing, Tucson, USA
- ³²Department of Astronomy and Planetary Science, Northern Arizona University, P.O. Box 6010, Flagstaff, AZ 86011, USA
- ³³Department of Astronomy and Astrophysics, University of Chicago, 5640 South Ellis Avenue, Chicago, IL 60637, USA
- ³⁴NSF NOIRLab, 950 N. Cherry Ave., Tucson, AZ 85719, USA
- ³⁵LPCA, Université Clermont-Auvergne, CNRS/IN2P3, Clermont-Ferrand, France
- ³⁶Université Paris-Saclay, CNRS/IN2P3, IJCLab, 15 Rue Georges Clemenceau, F-91405 Orsay, France
- ³⁷NCSA, University of Illinois at Urbana-Champaign, 1205 W. Clark St., Urbana, IL 61801, USA
- ³⁸Smithsonian Astrophysical Observatory, 60 Garden St., Cambridge MA 02138, USA
- ³⁹Caltech/IPAC, California Institute of Technology, MS 100-22, Pasadena, CA 91125-2200, USA
- ⁴⁰Santa Cruz Institute for Particle Physics and Physics Department, University of California–Santa Cruz, 1156 High St., Santa Cruz, CA 95064, USA
- ⁴¹Department of Physics, Brown University, 182 Hope Street, Providence, RI 02912, USA
- ⁴²D4D CONSULTING LTD., Suite 1 Second Floor, Everdene House, Deansleigh Road, Bournemouth, UK BH7 7DU
- ⁴³Aix Marseille Université, CNRS/IN2P3, CPPM, 163 avenue de Luminy, F-13288 Marseille, France
- ⁴⁴Université Clermont Auvergne, CNRS/IN2P3, LPCA, 4 Avenue Blaise Pascal, F-63000 Clermont-Ferrand, France
- ⁴⁵C. Iñaki Goenaga, 5, 20600, Guipúzcoa, Spain
- ⁴⁶INAF Osservatorio Astronomico di Trieste, Via Giovan Battista Tiepolo 11, 34143, Trieste, Italy
- ⁴⁷Department of Physics, P.O. Box 64, 00014 University of Helsinki, Finland
- ⁴⁸Asteroid Engineering Laboratory, Luleå University of Technology, Box 848, SE-981 28 Kiruna, Sweden
- ⁴⁹CNRS/IN2P3, CC-IN2P3, 21 avenue Pierre de Coubertin, F-69627 Villeurbanne, France
- ⁵⁰University of Arizona, Department of Astronomy and Steward Observatory, 933 N. Cherry Ave, Tucson, AZ 85721, USA
- ⁵¹Department of Astronomy, Yonsei University, 50 Yonsei-ro, Seoul 03722, Republic of Korea
- ⁵²Physics Department, University of California, One Shields Avenue, Davis, CA 95616, USA
- ⁵³Space Sciences Lab, University of California, 7 Gauss Way, Berkeley, CA 94720-7450, USA
- ⁵⁴Lancaster University, Lancaster, UK
- ⁵⁵Physics Department, University of California, 366 Physics North, MC 7300 Berkeley, CA 94720, USA
- ⁵⁶Department of Physics, Duke University, Durham, NC 27708, USA
- ⁵⁷Astromanager LLC, 63 Hala St, Hilo, 96720 Hawaii, USA
- ⁵⁸Center for Cosmology and Astro-Particle Physics, The Ohio State University, Columbus, OH 43210, USA
- ⁵⁹Physik-Institut, University of Zurich, Winterthurerstrasse 190, 8057 Zurich, Switzerland
- ⁶⁰Department of Physics Columbia University, New York, NY 10027, USA
- ⁶¹EPCC, University of Edinburgh, 47 Potterrow, Edinburgh, EH8 9BT, UK
- ⁶²Division of Physics, Mathematics and Astronomy, California Institute of Technology, Pasadena, CA 91125, USA
- ⁶³soZen Inc., 105 Clearview Dr, Penfield, NY 14526
- ⁶⁴Astrophysics Research Cluster, School of Mathematical and Physical Sciences, University of Sheffield, Sheffield, S3 7RH, United Kingdom
- ⁶⁵Science and Technology Facilities Council, Rutherford Appleton Laboratory, Harwell, UK
- ⁶⁶Department of Physics and Astronomy, Purdue University, 525 Northwestern Ave., West Lafayette, IN 47907, USA
- ⁶⁷Departamento de Matemática y Física Aplicadas, Facultad de Ingeniería, Universidad Católica de la Santísima Concepción, Alonso de Rivera 2850, Concepción, Chile
- ⁶⁸Australian Astronomical Optics, Macquarie University, North Ryde, NSW, Australia
- ⁶⁹AURA, 950 N. Cherry Ave., Tucson, AZ 85719, USA
- ⁷⁰Université Claude Bernard Lyon 1, CNRS/IN2P3, IP2I, 4 Rue Enrico Fermi, F-69622 Villeurbanne, France
- ⁷¹Department of Astronomy and Astrophysics, University of California–Santa Cruz, 1156 High St., Santa Cruz, CA 95064, USA
- ⁷²INAF Osservatorio di Astrofisica e Scienza dello Spazio Bologna, Via P. Gobetti 93/3, 40129, Bologna, Italy
- ⁷³Department of Physics and Astronomy (DIFA), University of Bologna, Via P. Gobetti 93/2, 40129, Bologna, Italy
- ⁷⁴Centro de Investigaciones Energéticas, Medioambientales y Tecnológicas, Av. Complutense 40, 28040 Madrid, Spain
- ⁷⁵J.Sick Codes Inc., Penetanguishene, Ontario, Canada
- ⁷⁶Science and Technology Facilities Council, UK Research and Innovation, Polaris House, North Star Avenue, Swindon, SN2 1SZ, UK
- ⁷⁷ASTRON, Oude Hoogeveensedijk 4, 7991 PD, Dwingeloo, The Netherlands
- ⁷⁸Department of Physics, Harvard University, 17 Oxford St., Cambridge MA 02138, USA
- ⁷⁹National Astronomical Observatory of Japan, Chile Observatory, Los Abedules 3085, Vitacura, Santiago, Chile
- ⁸⁰Department of Physics, University of Oxford, Denys Wilkinson Building, Keble Road, Oxford, OX1 3RH, UK
- ⁸¹LSST Discovery Alliance, 933 N. Cherry Ave., Tucson, AZ 85719, USA
- ⁸²Department of Physics and Astronomy, University of Pittsburgh, 3941 O'Hara Street, Pittsburgh, PA 15260, USA

(Dated: March 25, 2026)

ABSTRACT

We present Rubin Data Preview 1 (DP1), the first data from the NSF-DOE Vera C. Rubin Observatory, comprising raw and calibrated single-epoch images, coadds, difference images, detection catalogs, and ancillary data products. DP1 is based on 1792 optical/near-infrared exposures acquired over 48 distinct nights by the Rubin Commissioning Camera, LSSTComCam, on the Simonyi Survey Telescope at the Summit Facility on Cerro Pachón, Chile in late 2024. DP1 covers $\sim 15 \text{ deg}^2$ distributed across seven roughly equal-sized non-contiguous fields, each independently observed in six broad photometric bands, *ugrizy*. The median FWHM of the point-spread function across all bands is approximately $1''.14$, with the sharpest images reaching about $0''.58$. The 5σ point source depths for coadded images in the deepest field, the Extended Chandra Deep Field South, are: $u = 24.55, g = 26.18, r = 25.96, i = 25.71, z = 25.07, y = 23.1$. Other fields are no more than 2.2 magnitudes shallower in any band, where they have nonzero coverage. DP1 contains approximately 2.3 million distinct astrophysical objects, of which 1.6 million are extended in at least one band in coadds, and 431 solar system objects, of which 93 are new discoveries. DP1 is approximately 3.5 TB in size and is available to Rubin data rights holders via the Rubin Science Platform, a cloud-based environment for the analysis of petascale astronomical data. While small compared to future LSST releases, its high quality and diversity of data support a broad range of early science investigations ahead of full operations in 2026.

Keywords: Rubin Observatory – LSST

1. INTRODUCTION

The National Science Foundation (NSF)–Department of Energy (DOE) Vera C. Rubin Observatory is a ground-based, wide-field optical/near-infrared facility located on Cerro Pachón in northern Chile. Named in honor of Vera C. Rubin, a pioneering astronomer whose groundbreaking work in the 20th century provided the first convincing evidence for the existence of dark matter (V. C. Rubin & W. K. Ford 1970; V. C. Rubin et al. 1980), the observatory’s prime mission is to carry out the Legacy Survey of Space and Time (LSST) (Ž. Ivezić et al. 2019a). This 10-year survey is designed to obtain rapid-cadence, multi-band imaging of the entire visible southern sky approximately every 3–4 nights. Over its main $18,000 \text{ deg}^2$ footprint, the LSST is expected to reach a depth of ~ 27 magnitude in the r-band, with ~ 800 visits per pointing in all filters (F. B. Bianco et al. 2022).

The Rubin Observatory system consists of four main components: the Simonyi Survey Telescope, featuring an 8.4 m diameter (6.5 m effective aperture) primary mirror that delivers a wide field of view; the 3.2-gigapixel LSST Science Camera (LSSTCam), capable of imaging 9.6 square degrees per exposure⁸³ with seeing-limited

quality in six broadband filters, *ugrizy* (320–1050 nm); an automated Data Management System that processes and archives tens of terabytes of data per night, generating science-ready data products within minutes for a global community of scientists; and an Education and Public Outreach (EPO) program that provides real-time data access, interactive tools, and educational content to engage the public. The integrated system’s étendue⁸⁴ of $319 \text{ m}^2 \text{ deg}^2$, is over an order of magnitude larger than that of any previous optical observatory, enabling a fast, large-scale survey with exceptional depth in a fraction of the time compared to other observatories.

The observatory’s design is driven by four key science themes: probing dark energy and dark matter; taking an inventory of the solar system; exploring the transient and variable optical sky; and mapping the Milky Way (Ž. Ivezić et al. 2019a). These themes inform the optimization of a range of system parameters, including image quality; photometric and astrometric accuracy; single-visit depth; coadded survey depth; the filter complement; the total number of visits per pointing and their distribution on the sky; and total sky coverage. Additionally, they inform the design of the data processing and access systems. By optimizing the system parameters to support a wide range of scientific goals, we maximize the observatory’s scientific output across

* Author is deceased

⁸³ We define an “exposure” as the process of exposing all detectors in the focal plane. It is synonymous with the term “visit” in DP1. By contrast, an “image” is the output of a single detector following an exposure.

⁸⁴ The product of the primary mirror area and the angular area of its field of view for a given set of observing conditions.

all areas, making Rubin a powerful discovery machine capable of addressing a broad range of astrophysical questions.

Throughout the duration of the LSST, Rubin Observatory will issue a series of Data Releases, each representing a complete reprocessing of all LSST data collected up to that point. Prior to the start of the LSST survey, commissioning activities generated a significant volume of science-grade data. To make this early data available to the community, the Rubin Early Science Program (L. P. Guy et al. 2026) was established. One key component of this program is a series of Data Previews; early versions of the LSST Data Releases. These previews include preliminary data products derived from both simulated and commissioning data, which, together with early versions of the data access services, are intended to support high-impact early science, facilitate community readiness, and inform the development of Rubin’s operational capabilities ahead of the start of full survey operations. All data and services provided through the Rubin Early Science Program are offered on a shared-risk basis⁸⁵.

This paper describes Rubin’s second of three planned Data Previews: Data Preview 1 (DP1) (NSF-DOE Vera C. Rubin Observatory 2025a). The first, Data Preview 0 (DP0), contained data products produced from the processing of simulated LSST-like data sets. These were released together with a very early version of the Rubin Science Platform (RSP) (M. Jurić et al. 2019), which provided the data access services. DP0 was released in multiple phases; DP0.1, DP0.2, and DP0.3, each building upon the previous and incorporating new data and functionalities. DP0.1 and DP0.2 uses data from the cosmoDC2 simulations (LSST Dark Energy Science Collaboration (LSST DESC) et al. 2021) prepared by the Dark Energy Science Collaboration (DESC), whereas DP0.3 is based on simulated datasets from the Solar System Science Collaboration (SSSC). Online documentation for DP0 is available at <https://dp0.lsst.io>.

DP1 contains data products derived from the reprocessing of science-grade exposures acquired by the Rubin Commissioning Camera (LSSTComCam) in late 2024. The third and final Data Preview, Data Preview 2 (DP2), is planned to be based on a reprocessing of all science-grade data taken with Rubin’s LSSTCam during commissioning.

All Rubin Data Releases and Previews are subject to a two-year proprietary period, with immediate access granted exclusively to LSST data rights holders⁸⁶ (R. Blum & the Rubin Operations Team 2020). After the two-year proprietary period, DP1 will be made public. However, even once the data become public, access for individuals without data rights will not be provided through Rubin Data Access Centers in the US and Chile (R. Blum & the Rubin Operations Team 2020). Alternative access mechanisms are still under discussion and have not yet been finalized.

In this paper, we describe the contents and validation of Rubin DP1, the first Data Preview to deliver data derived from observations conducted by the Vera C. Rubin Observatory, as well as the data-access mechanisms and community-support services that accompany it. DP1 is based on the reprocessing of 1792 science-grade exposures acquired during the first on-sky commissioning campaign, conducted over 48 nights between 2024-10-24 and 2024-12-11. It covers a total area of approximately ~ 15 deg² distributed across seven distinct non-contiguous fields. The data products include raw and calibrated single-epoch images, coadded images, difference images, detection catalogs, and other derived data products. DP1 is about 3.5 TB in size and contains around 2.3 million distinct astronomical objects, detected in 2644 coadded images. Full DP1 release documentation is available at <https://dp1.lsst.io>. Despite Rubin Observatory still being in commissioning and not yet complete at the time the observations were acquired, Rubin DP1 provides an important first look at the data, showcasing its characteristics and capabilities.

The structure of this paper is as follows. In section 2 we describe the observatory system and overall construction and commissioning status at the time of data acquisition, the seven fields included in DP1, and the observing strategy used. Section 3 summarizes the contents of DP1 and the data products contained in the release. The data processing pipelines are described in section 4, followed by a description of the data validation and performance assessment in section 5. Section 6 describes the RSP, a cloud-based data science infrastructure that provides tools and services to Rubin data rights holders to access, visualize and analyze peta-scale data generated by the LSST. Section 7 presents Rubin Observatory’s model for community support, which emphasizes self-help via documentation and tutorials, and employs an open platform for issue reporting that en-

⁸⁵ Shared risk means early access with caveats: the community benefits from getting a head start on science, preparing analyses, and providing feedback, while also accepting that the system may not work as well as it will during full operations.

⁸⁶ Individuals or institutions with formal authorization to access proprietary data collected by the Vera C. Rubin Observatory. See <https://www.lsst.org/scientists/international-drh-list>

ables crowd-sourced solutions. Finally, a summary of the DP1 release and information on expected future releases of data is given in section 8. The appendix contains a useful glossary of terms used throughout this paper.

All magnitudes quoted are in the AB system (J. B. Oke & J. E. Gunn 1983), unless otherwise specified.

2. ON-SKY COMMISSIONING CAMPAIGN

The primary objective of the first Rubin on-sky commissioning campaign was to optically align the Simonyi Survey Telescope and verify its ability to deliver acceptable image quality using the Commissioning Camera, LSSTComCam. Additionally, the campaign provided valuable operational experience to support commissioning the LSST Science Camera, LSSTCam (T. Lange et al. 2024; A. Roodman et al. 2024). We note that commissioning LSSTComCam was not an objective of the campaign; rather LSSTComCam was used as a tool to support broader observatory commissioning, including early testing of the Active Optics System (AOS) (§2.1) and the LSST Science Pipelines (§2.4). As a result, many artifacts present in the data are specific to LSSTComCam and will be addressed only if they persist with LSSTCam. Accordingly, the image quality achieved during this campaign, and in the DP1 data, may not reflect the performance ultimately expected from LSSTCam.

Approximately 16,000 exposures⁸⁷ were collected during this campaign, the majority in support of AOS commissioning, system-level verification, and end-to-end testing of the telescope’s hardware and software. This included over 10000 exposures for AOS commissioning, more than 2000 bias and dark calibration frames, and over 2000 exposures dedicated to commissioning the LSST Science Pipelines. For DP1, we have selected a subset of 1792 science-grade exposures from this campaign that are most useful for the community to begin preparing for early science.

At the time of the campaign, the observatory was still under construction, with several key components, such as dome thermal control, full mirror control, and the final AOS configuration either incomplete or still undergoing commissioning. As a result, image quality varied widely throughout the campaign and exhibited a broader distribution than is expected with LSSTCam. Despite these limitations, the campaign success-

fully demonstrated system integration and established a functional observatory.

2.1. Simonyi Survey Telescope

The Simonyi Survey Telescope (B. Stalder et al. 2024) features a unique three-mirror design, including an 8.4-meter Primary Mirror Tertiary Mirror (M1M3) fabricated from a single substrate and a 3.5-meter Secondary Mirror (M2). This compact configuration supports a wide 3.5-degree field of view while enabling exceptional stability, allowing the telescope to slew and settle in under five seconds. To achieve the scientific goals of the 10-year LSST, the Observatory must maintain high image quality across its wide field of view (Ž. Ivezić et al. 2019b). This is accomplished through the AOS (B. Xin et al. 2015; G. Megias Homar et al. 2024), which corrects, between successive exposures, wavefront distortions caused by optical misalignments and mirror surface deformations, primarily due to the effect of gravitational and thermal loads.

The AOS, which comprises an open-loop component and a closed-loop component, optimizes image quality by aligning the camera and M2 relative to M1M3, as well as adjusting the shapes of all three mirrors to nanometer precision. The AOS open-loop component corrects for predictable distortions and misalignments, while the closed-loop component addresses unpredictable or slowly varying aberrations using feedback from the corner wavefront sensors. The closed-loop wavefront sensing technique is curvature wavefront sensing, which infers wavefront errors in the optical system by analyzing extra- and intra-focal star images (S. Thomas et al. 2023). Since LSSTComCam lacks dedicated wavefront sensors, wavefront errors were instead estimated by defocusing the telescope ± 1.5 mm on either side of focus and applying the curvature wavefront sensing pipeline to the resulting images. Each night began with an initial alignment correction using a laser tracker to position the system within the capture range of the closed-loop algorithm (G. Megias Homar et al. 2024). Once this coarse alignment was complete, the AOS refined the optical alignment and applied mirror surfaces corrections to optimize the image quality across the LSSTComCam field of view.

During LSST Science Pipelines commissioning (§2.4), observations were conducted using the AOS in open-loop mode only, without closed-loop corrections between exposures. Closed-loop operation, which requires additional intra- and extra-focal images with LSSTComCam, was not compatible with the continuous data acquisition needed by the pipelines. The image quality for these data was monitored by measuring the Point

⁸⁷ We define an exposure as the process of exposing all LSSTComCam detectors. It is synonymous with visit in DP1. By contrast, an image is the output of a single LSSTComCam detector following an exposure.

Spread Function (PSF) at Full Width at Half-Maximum (FWHM), and closed-loop sequences were periodically run when image quality degradation was observed.

2.2. The LSST Commissioning Camera

LSSTComCam (B. Stalder et al. 2022, 2020; J. Howard et al. 2018; SLAC National Accelerator Laboratory & NSF-DOE Vera C. Rubin Observatory 2024) is a 144-megapixel version of the 3.2-gigapixel LSSTCam. It covers approximately 5% of the LSSTCam focal plane area, with a field of view of $\sim 0.5 \text{ deg}^2$ ($40' \times 40'$), compared to LSSTCam's 9.6 deg^2 . It was developed to validate camera interfaces with other observatory components and evaluate overall system performance prior to the start of LSSTCam commissioning. Although LSSTComCam has a smaller imaging area, it shares the same plate scale of $0''.2$ per pixel and is housed in a support structure that replicates the mass, center of gravity, and physical dimensions of LSSTCam. All mechanical and utility interfaces to the telescope are implemented identically, enabling full end-to-end testing of observatory systems, including readout electronics, image acquisition, and data pipelines. Although the LSSTComCam cryostat employs a different cooling system (Cryotels) to that of LSSTCam, it included a refrigeration pathfinder to validate the cryogenic system intended for LSSTCam.

The LSSTCam focal plane comprises 25 modular rafts arranged in a 5×5 grid, of which 21 are science rafts dedicated to imaging and 4 are corner rafts used for guiding and wavefront sensing. LSSTCam employs CCD sensors from two vendors: Imaging Technology Laboratory, University of Arizona (UA) (ITL) and Teledyne (E2V). In contrast, LSSTComCam contains only a single science raft equipped exclusively with ITL sensors. Figure 1 presents a schematic of the LSSTCam focal plane, with the LSSTComCam raft positioned at the center, corresponding to the LSSTCam central science raft location. The perspective is from above, looking down through the LSSTComCam lenses onto the focal plane.

Each science raft is a self-contained unit comprising nine $4\text{K} \times 4\text{K}$ Charge-Coupled Device (CCD) (G. E. Smith 2010) sensors arranged in a 3×3 mosaic, complete with integrated readout electronics and cooling systems. Each sensor is subdivided into 16 segments arranged in a 2×8 layout, with each segment consisting of 512×2048 pixels and read out in parallel using individual amplifiers. This design is identical across all science rafts. To maintain uniform performance and calibration, each raft is populated exclusively with sensors from a single vendor.

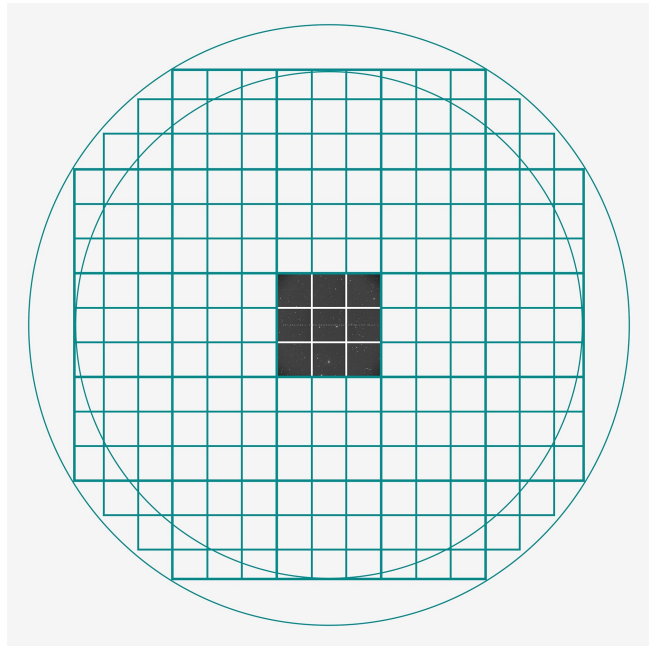


Figure 1. LSSTComCam focal plane layout illustrating the placement of its nine sensors, shown in gray, which form a raft. The view is looking down from above the focal plane through the LSSTComCam lenses. LSSTComCam is Raft 22 (R22). We also indicate the location of the LSSTCam sensors (open squares) to highlight the field-of-view of LSSTComCam in relation to that of LSSTCam.

LSSTComCam consists of a single science raft, designated Raft 22 (R22), equipped solely with ITL sensors. These sensors were selected from the best-performing remaining ITL devices after the LSSTCam rafts were fully populated. Some exhibit known issues such as high readout noise (e.g., Detector 8) and elevated Charge Transfer Inefficiency (CTI) (e.g., Detector 5). Consequently, certain image artifacts present in the DP1 dataset may be specific to LSSTComCam. Figure 2 shows the LSSTComCam R22 focal plane layout and the placement and numbering scheme of sensors (S) and amplifiers (C). This configuration is identical across all science rafts in LSSTCam. The LSSTCam and LSSTComCam focal planes are described in detail in A. A. Plazas Malagón et al. (2026).

2.2.1. Filter Complement

LSSTComCam supports imaging with six broadband filters *ugrizy* spanning 320–1050 nm, identical in design to LSSTCam. However, its filter exchanger can hold only three filters at a time, compared to five with LSSTCam. The full-system throughput of the six LSSTComCam filters, which encompasses contributions from a standard atmosphere at airmass 1.2, telescope optics, camera surfaces, and the mean ITL detector quan-

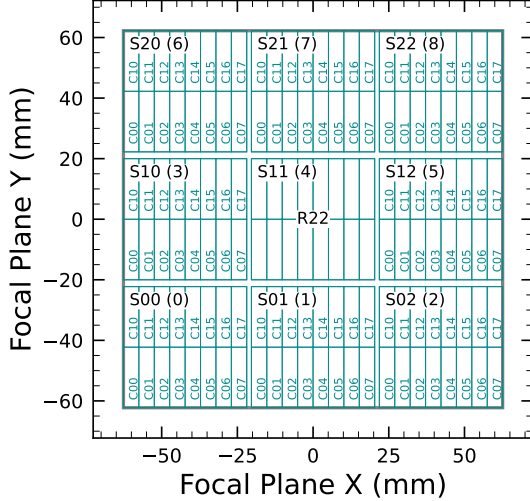


Figure 2. LSSTComCam focal plane layout, showing Raft 22 (R22) and the placement and numbering scheme of sensors (S) and amplifiers (C). The view is from above, looking through the LSSTComCam lenses onto the focal plane. Each sensor contains 16 amplifiers, and the raft is composed of a 3×3 array of sensors. The detector number for each sensor is indicated in parentheses.

tum efficiency is shown in Figure 3. The corresponding transmission curves are provided as a DP1 data product (§3.6.1).

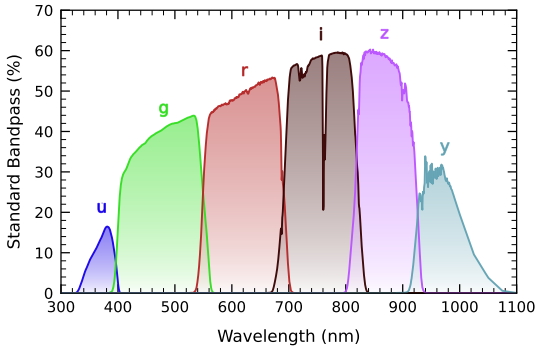


Figure 3. LSSTComCam standard bandpasses, illustrating full system throughput. The bandpasses include a standard atmosphere at airmass 1.2, telescope optics, camera surfaces, and mean ITL detector quantum efficiency. The corresponding transmission curves are provided as a DP1 data product.

2.2.2. Timing Calibration

The absolute time accuracy of data taken with LSST-ComCam relies on the Network Time Protocol (NTP) for clock synchronization, which should be accurate to approximately 1 millisecond. In order to evaluate the absolute timing accuracy of the entire system we observed the geosynchronous satellite EUTELSAT 117

West B with a set of 10 usable 10-second exposures over two nights. EUTELSAT 117 West B is part the Global Positioning System (GPS) system and serves as one of the Wide Area Augmentation System (WAAS) satellites operated for the U.S. Federal Aviation Administration (FAA) and used to broadcast GPS corrections to air traffic.

As these satellites are part of the GPS system, their positions are tracked very precisely and the record of their locations is published after the fact and can be downloaded. Following the technique previously employed by other surveys, (J. L. Tonry et al. 2018), we observed the satellite while tracking the sky and then downloaded the data-files with its precise locations from the National Satellite Test Bed web site⁸⁸. By comparing the measured and predicted locations of the start of the satellite track on the sky, we determined that (relative to the start of integration-time recorded in the Flexible Image Transport System (FITS) headers) our time was accurate to 53.6 ± 11.0 milliseconds.

This work continues to be an area of ongoing study, with the exact timing of when the shutter open command is issued, and the complete profile of the shutter movement not yet determined. However the open command is on average near 29 milliseconds later. Incorporating the delays into the fit reduces the offset to 24.8 ± 11.0 milliseconds.

The full shutter takes approximately 396 milliseconds to completely open. As the LSSTComCam sensors are centered in the aperture, the center of the focal plane should be exposed about half-way through the shutter open procedure, 198 milliseconds after the open command. There are uncertainties on the full motion profile, and the blade direction motions are currently not known, but the fraction of the shutter aperture subtended by the focal plane is 52%. This implies that that the shutter will pass any pixel between 198 ± 103 milliseconds. Subtracting this from the fitted delay of 24.8 milliseconds and adding the fitted error of 11.0 milliseconds in quadrature, results in a current conservative estimate of the delay of -173.2 ± 104.1 milliseconds, consistent with and smaller than the constraints on the timing offset determined using astrometric residuals from known asteroid associations presented in §5.9.2.

2.3. Flat Field System

During the on-sky campaign, key components of the Rubin calibration system (P. Ingraham et al. 2022), including the flat field screen, had not yet been installed. As a result, flat fielding for DP1 relied en-

⁸⁸ <https://www.nstb.tc.faa.gov/nstbarchive.html>

tirely on twilight flats. While twilight flats pose challenges such as non-uniform illumination and star print-through, they were the only available option during LSSTComCam commissioning and for DP1 processing. To mitigate these limitations, dithered, tracked exposures were taken over a broad range of azimuth and rotator angles to construct combined flat calibration frames. Exposure times were dynamically adjusted to reach target signal levels of between 10,000 and 20,000 electrons. Future campaigns with LSSTCam will benefit from more stable and uniform flat fielding using the Rubin flat field system, described in P. Fagrellius & E. S. Rykoff (2025).

2.4. LSST Science Pipelines Commissioning

Commissioning of the LSST Science Pipelines, (Rubin Observatory Science Pipelines Developers 2025), began once the telescope was able to routinely deliver sub-arcsecond image quality. The goals included testing the internal astrometric and photometric calibration across a range of observing conditions, validating the difference image analysis and prompt processing (K.-T. Lim 2023) framework, and accumulating over 200 visits per band to evaluate deep coadded images with integrated exposure times roughly equivalent to those of the planned LSST Wide-Fast-Deep (WFD) 10-year depth. To support these goals, seven target fields were selected that span a range of stellar densities, overlap with external reference datasets, and collectively span the full breadth of the four primary LSST science themes. These seven fields form the basis of the DP1 dataset. Figure 4 shows the locations of these seven fields on the sky, overlaid on the LSST baseline survey footprint (R. L. Jones et al. 2021; P. Yoachim 2022; Rubin’s Survey Cadence Optimization Committee et al. 2022, 2023, 2025), along with the sky coverage of both the LSSTCam and LSSTComCam focal planes. Each of the seven target fields was observed repeatedly in multiple bands over many nights. A typical observing epoch on a given target field consisted of 5-20 visits in each of the three loaded filters. Only images taken as 1x30 second exposures have been included in DP1. All images were acquired using the Rubin Feature-Based Scheduler (FBS), version 3.0 (E. Naghib et al. 2019; P. Yoachim et al. 2024). Table 1 lists the seven DP1 fields and their pointing centers, and provides a summary of the band coverage in each.

Figure 5 shows the temporal sampling of observations by filter and by night. The figure indicates the dates on which each field was observed in a given band but does not convey the total number of observations obtained per filter on any individual night. Gaps in coverage across some bands arise from the fact that LSSTComCam can only accommodate three filters at a time

(see §2.2). As the campaign progressed, the temporal sampling became denser across all fields, reflecting improved efficiency and increased time allocated for science observations. The Extended Chandra Deep Field-South Survey (ECDFS) field received the most consistent and densest temporal sampling. It is important to note that the time sampling in the DP1 dataset differs significantly from what will be seen in the final LSST data. All fields except for the low ecliptic latitude field, Rubin_SV_38_7, used a small random dithering pattern. The random translational dithers of the telescope boresight were applied for each visit, with offsets of up to 0.2 degrees around the pointing center. The rotational dithers of the camera rotator were typically approximately 1 degree per visit, with larger random offsets at each filter change, which worked to keep operational efficiency high. The Rubin_SV_38_7 field used a different dither pattern to optimize coverage of Solar System Objects and test Solar System Object linking across multiple nights. These observations used a 2x2 grid of LSSTComCam pointings to cover an area of about 1.3 degreex1.3 degrees. The visits cycled between the grid’s four pointing centers, each separated by 0.65 degrees, and used small random translational dithers to fill chip gaps with the goal of acquiring 3-4 visits per pointing center per band in each observing epoch. The RA and Dec values provided in Table 1 for this field represent approximately the center of the four fields.

Figure 6 shows sky coverage maps showing the distribution of visits in each of the seven DP1 fields, color coded by band. The images clearly show the focal plane chip gaps and dithering pattern. Only the detectors for which single frame processing succeeded are included in the plots, which explains why the central region of 47_Tuc looks thinner than the other fields (see §5.10). Table 2 reports the 5 σ point source depths for coadded images per field and per band, where coverage in a band is non-zero, together with the expected 10-year LSST depths derived from the baseline simulated survey (F. B. Bianco et al. 2022).

2.5. Delivered Image Quality

The delivered image quality is influenced by contributions from both the observing system (i.e., dome, telescope and camera) and the atmosphere. During the campaign, the Rubin Differential Image Motion Monitor (DIMM) was not operational, so atmospheric seeing was estimated using live data from the Southern Astrophysical Research Telescope (SOAR) Ring-Image Next Generation Scintillation Sensor (RINGSS) seeing monitor, also located on Cerro Pachón. Although accelerometers mounted on the mirror cell and top-end assembly were

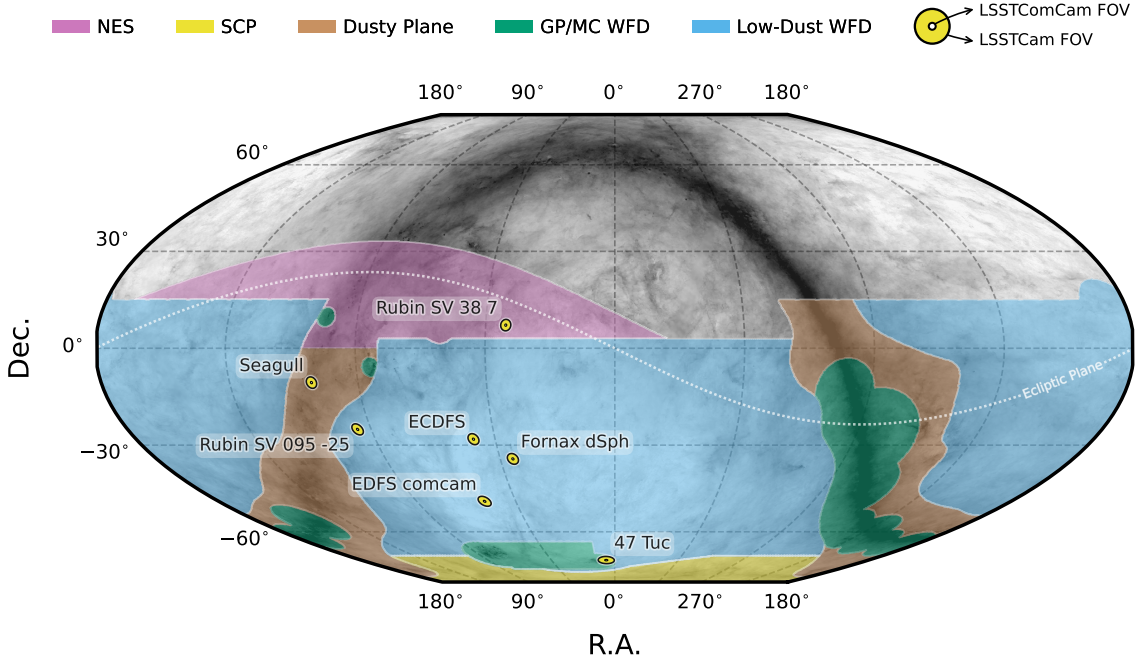


Figure 4. Locations of the seven DP1 fields overlaid on the LSST baseline survey footprint. NES: North Ecliptic Spur; SCP: South Celestial Pole; Low-Dust WFD: regions away from the Galactic Plane (GP) observed with a WFD cadence; GP/MC WFD: Galactic Plane and Magellanic Clouds regions observed with a WFD cadence. The fields of view of the LSSTCam and LSSTComCam focal planes are shown as concentric yellow circles about the pointing center of each field. The background Milky Way dust map is based on the FDS model (D. P. Finkbeiner et al. 1999).

Table 1. DP1 fields and pointing centers with the number of exposures in each band per field. ICRS coordinates are in units of decimal degrees, and are specified as J2000.

Field Code	Field Name	RA	Dec	Band					Total	
				deg	deg	<i>u</i>	<i>g</i>	<i>r</i>		<i>i</i>
47_Tuc	47 Tucanae Globular Cluster	6.128	-72.090	6	10	32	19	0	5	72
ECDFS	Extended Chandra Deep Field South	53.160	-28.100	43	230	237	162	153	30	855
EDFS_comcam	Rubin SV Euclid Deep Field South	59.150	-48.730	20	61	87	42	42	20	272
Fornax_dSph	Fornax Dwarf Spheroidal Galaxy	40.080	-34.450	0	5	25	12	0	0	42
Rubin_SV_095_-25	Rubin SV Low Galactic Latitude Field	95.040	-25.000	33	82	84	23	60	10	292
Rubin_SV_38_7	Rubin SV Low Ecliptic Latitude Field	37.980	7.015	0	44	40	55	20	0	159
Seagull	Seagull Nebula	106.300	-10.510	10	37	43	0	10	0	100
Total				112	469	548	313	285	65	1792

available to track dynamic optics effects, such as mirror oscillations that can degrade optical alignment, this data was not used during the campaign. Mount encoder data were used to measure the mount jitter in every image, with a measured median contribution of 0.004 arcseconds to image degradation. As the pointing model was not fine tuned, tracking errors could range from 0.2 to 0.4 arcseconds per image, depending on RA and Dec.

Dome and mirror-induced seeing were not measured during the campaign.

The DP1 median delivered image quality, quantified as the PSF at FWHM across all filters and target fields, is $1''.14$. The best images achieve a PSF FWHM of approximately $0''.58$. Both the per-sensor PSF FWHM and the overall median vary depending on the filter and the specific target field. The median delivered image quality per band and target field is provided in Table 3. Fig-

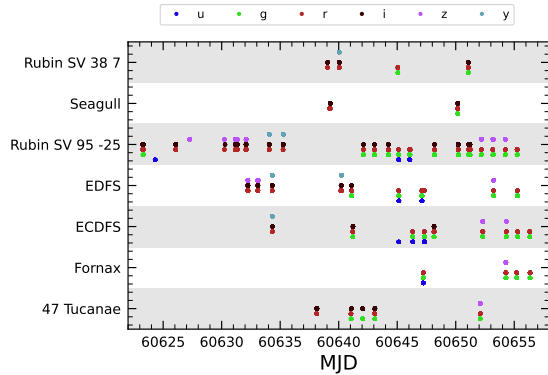


Figure 5. Temporal distribution of DP1 observations, grouped by field as a function of Modified Julian Date (MJD) and color-coded by filter. Each point indicates that a given field was observed at least once in the corresponding filter on that date.

Table 2. DP1 median 5σ coadded point-source detection limits per field and band, expressed in magnitudes, compared with the expected 10-year LSST values derived from the baseline simulated survey (F. B. Bianco et al. 2022).

Field Code	Band					
	<i>u</i>	<i>g</i>	<i>r</i>	<i>i</i>	<i>z</i>	<i>y</i>
47_Tuc	-	24.03	24.24	23.90	-	21.79
ECDFS	24.55	26.18	25.96	25.71	25.07	23.10
EDFS_comcam	23.42	25.77	25.72	25.17	24.47	23.14
Fornax_dSph	-	24.53	25.07	24.64	-	-
Rubin_SV_095_-25	24.29	25.46	24.95	24.86	24.32	22.68
Rubin_SV_38_7	-	25.46	25.15	24.86	23.52	-
Seagull	23.51	24.72	24.19	-	23.30	-
LSST 10-year	25.73	26.86	26.88	26.34	25.63	24.87

Figure 7 shows the distribution of PSF FWHM (in arcsec) over all 16071 individual sensors images. Ongoing efforts aim to quantify all sources of image degradation, including contributions from the camera system; static and dynamic optical components; telescope mount motion; observatory-induced seeing from the dome and primary mirror; and atmospheric conditions. For the LSST, the design specification for the median delivered image quality, referenced to the zenith and 550 nm, is $0''.7$. This value corresponds to the measured median atmospheric seeing at the Cerro Pachón site and a system contribution to delivered image quality of $0''.35$ added in quadrature.

Table 3. DP1 Median image quality per field and per band quantified as the PSF at FWHM in arcseconds.

Field Code	Band						All
	<i>u</i>	<i>g</i>	<i>r</i>	<i>i</i>	<i>z</i>	<i>y</i>	
47_Tuc	-	1.27	1.25	1.11	-	1.33	1.22
ECDFS	1.40	1.14	1.08	1.00	1.00	1.07	1.08
EDFS_comcam	1.88	1.25	1.20	1.10	1.18	0.99	1.19
Fornax_dSph	-	1.16	0.82	0.93	-	-	0.85
Rubin_SV_095_-25	1.40	1.25	1.14	0.97	1.17	0.82	1.19
Rubin_SV_38_7	-	1.13	1.13	1.10	1.22	-	1.13
Seagull	1.50	1.34	1.19	-	1.19	-	1.25
All	1.48	1.17	1.12	1.03	1.11	1.01	1.13

3. OVERVIEW OF THE CONTENTS OF RUBIN DP1

In this section we describe the Rubin DP1 data products and provide summary statistics for each. For more detailed information, we refer the reader to the DOI-registered DP1 release documentation available at <https://dp1.lsst.io> and the catalog schemas available at <https://sdm-schemas.lsst.io>.⁸⁹

The DP1 science data products are derived from the 15972 individual CCD images taken across 1792 exposures in the seven LSSTComCam commissioning fields (§2.4). To aid legibility, we have separated the descriptions of the data products from the description of the data release processing pipeline (§4). Similarly, as the DP1 data products can be accessed via one or both of International Virtual Observatory Alliance (IVOA) Services (§6.2.1) or the Data Butler (§6.2.2), we describe them here in a manner that is agnostic to the means of access.

The data products that comprise DP1 provide an early preview of future LSST data releases and are strongly dependent on the type and quality of the data that was collected during the LSSTComCam on-sky campaign (§2.4). Consequently not all anticipated LSST data products, as described in the Data Product Definition Document (DPDD) (M. Jurić et al. 2023), were produced for the DP1 dataset.

Rubin Observatory has adopted the convention by which single-epoch detections are referred to as “Sources”, and the astrophysical object associated with

⁸⁹ Searchable catalog schemas are also available to Data Rights Holders via the Rubin Science Platform at <https://data.lsst.cloud>.

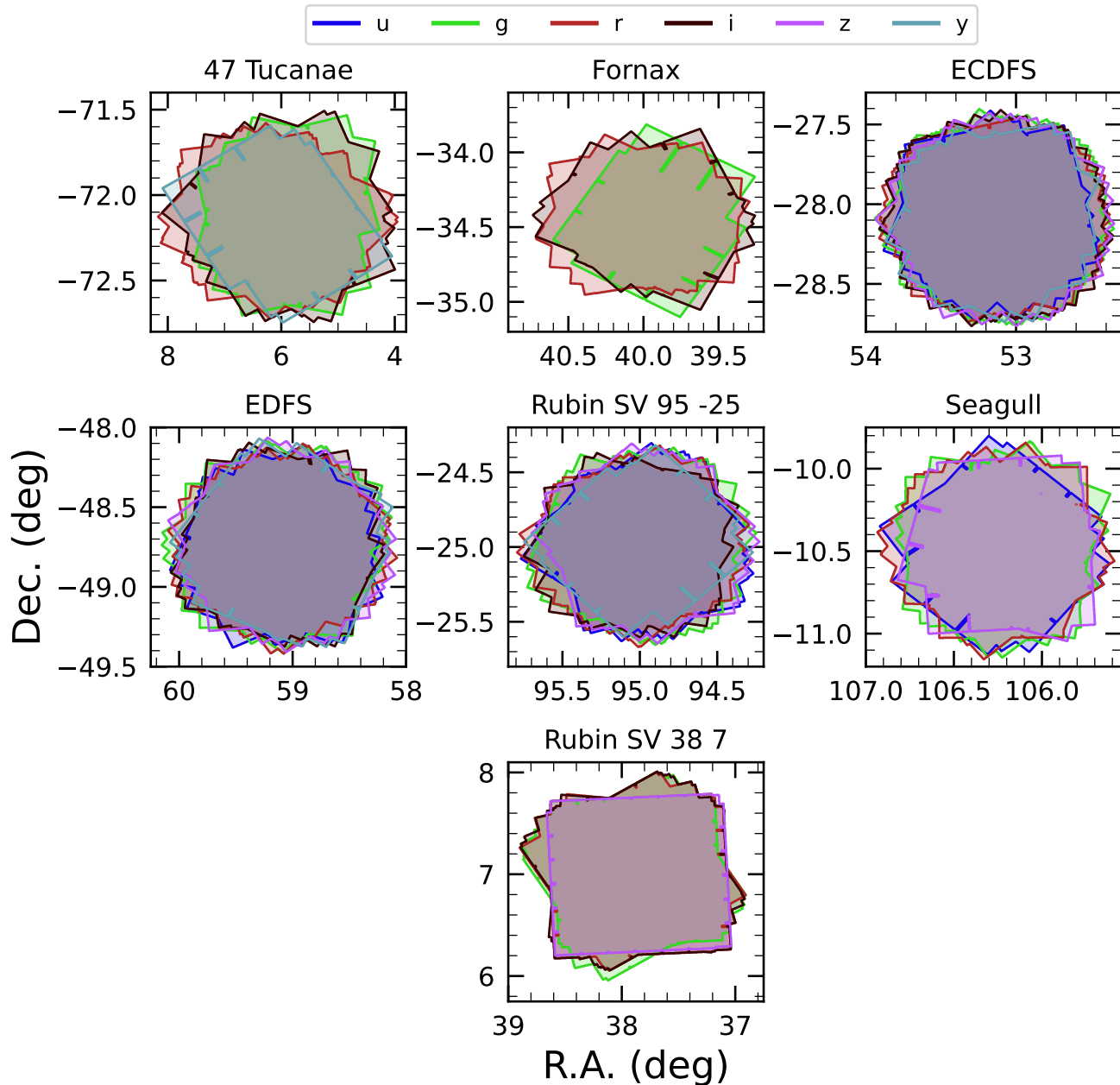


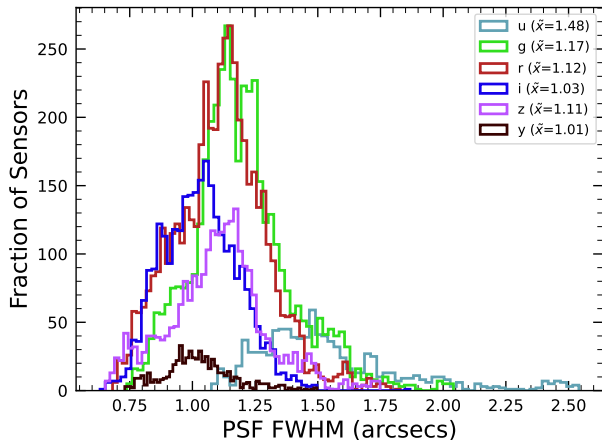
Figure 6. Sky coverage maps showing the distribution of visits in each field, color coded by band. The images clearly show the focal plane chip gaps and dithering pattern. Only the detectors for which single frame processing succeeded are included in the plots, which explains why the central region of 47_Tuc looks thinner than the other fields.

a given detection is referred to as an “Object”⁹⁰. As such, a given Object will likely have multiple associated Sources, since it will be observed in multiple epochs.

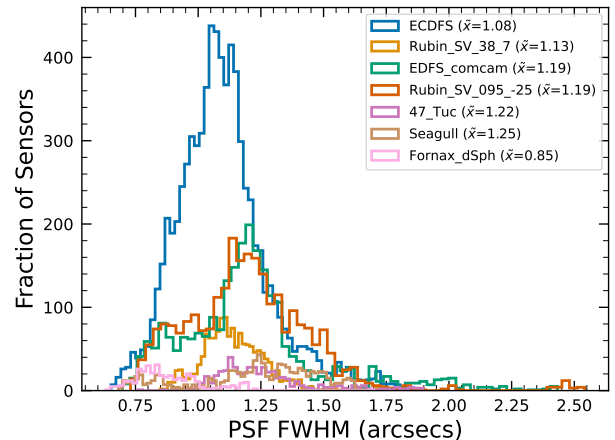
At the highest level, the DP1 data products fall into one of five types:

- **Science Images**, including single-epoch images, deep and template coadded images, and difference images (§3.1);
- **Catalogs** of astrophysical Sources and Objects detected and measured in the aforementioned images. We also provide the astrometric and photometric reference catalog generated from external

⁹⁰ We caution that this nomenclature is not universal; for example, some surveys use “detections” for what we call “sources”, and “sources” for what we call “objects”.



(a) PSF FWHM (arcsecs) per passband across all DP1 target fields.



(b) PSF FWHM (arcsecs) per DP1 target field across all passbands

Figure 7. Histograms showing the distribution of delivered image quality for all 16071 single-epoch individual sensors in the DP1 dataset per passband (a) and per field (b). The median values are given in the legend.

sources that was used during processing to generate the DP1 data products (§3.2);

- **Maps**, which provide non-science-level visualizations of the data within the release. They include, for example, zoomable multi-band images and coverage maps (§3.4.1);
- **Ancillary data products**, including, for example, the parameters used to configure the data processing pipelines, log and processing performance files, and **calibration** data products (§3.6);
- **Metadata** in the form of tables containing information about each visit and processed image, such as pointing, exposure time, and a range of image quality summary statistics (§3.5).

While images and catalogs are expected to be the primary data products for scientific research, we also recognize the value of providing access to other data types to support investigations and ensure transparency.

To facilitate processing, Rubin DP1 uses a single skymap⁹¹ that covers the entire sky area encompassing the seven DP1 fields. The DP1 skymap divides the entire celestial sphere into 18938 **tracts**, each covering approximately 2.8 deg^2 . The **tracts** are arranged in rings of declination, ordered from south to north, then with increasing right ascension within a ring. Each **tract** is further subdivided into 10×10 equally-sized patches.

⁹¹ A skymap is a tiling of the celestial sphere, organizing large-scale sky coverage into manageable sections for processing and analysis. While the skymap described here is specific to DP1, we do not anticipate major changes to the skymap in future data releases.

Both **tracts** and patches overlap with their neighboring regions. The amount of overlap between **tracts** changes with declination, with **tracts** nearest the poles having the greatest degree of overlap; the minimum overlap between **tracts** is $1'.0$. By contrast, the amount of overlap between patches is constant, with each **patch** overlapping each of its neighbouring patches by 80% . Each patch covers 0.036 deg^2 which, due to the patch overlap, is slightly larger than the tract area divided by the number of patches in a tract. The aerial coverage of a patch is comparable to, but somewhat smaller than, the 0.058 deg^2 field-of-view of a single LSSTComCam or LSSTCam detector, meaning each detector image spans multiple patches. The size of a tract is larger than the LSSTComCam field of view. However, since each observed field extends across more than one tract, each field covers multiple tracts.

The skymap is integral to the production of co-added images. To create a coadded image, the processing pipeline selects all calibrated science images in a given field that meet specific quality thresholds (§3.1 and §4.5.1) for a given **patch**, warps them onto a single consistent pixel grid for that **patch**, as defined by the skymap, then coadds them. Each individual coadd image therefore covers a single **patch**.

Throughout this section, the data product names are indicated using monospace font. Data products are accessed via either the IVOA Services (§6.2.1) or the Data Butler (§6.2.2).

3.1. Science Images

Science images are exposures of the night sky, as distinct from **calibration** images (§3.6.3). Although the release includes **calibration** images, thereby allowing users

Table 4. Number of **raw** images per field and band. Each raw image corresponds to a single 30-second LSSTComCam exposure on one CCD. Most exposures produce nine raw images, one per sensor in the focal plane, however some yield fewer due to occasional hardware or readout issues.

Field Code	Band						Total
	<i>u</i>	<i>g</i>	<i>r</i>	<i>i</i>	<i>z</i>	<i>y</i>	
47_Tuc	54	90	288	171	0	45	648
ECDFS	387	2070	2133	1455	1377	270	7692
EDFS_comcam	180	549	783	378	378	180	2448
Fornax_dSph	0	45	225	108	0	0	378
Rubin_SV_095_-25	297	738	756	207	540	90	2628
Rubin_SV_38_7	0	396	360	495	180	0	1431
Seagull	90	333	387	0	90	0	900
Total	1008	4221	4932	2814	2565	585	16125

to reprocess the raw images if needed, this is expected to be necessary only in rare cases. Users are strongly encouraged to start from the `visit_image` provided. The data product names shown here are those used by the Data Butler, but the names used in the IVOA Services differ only slightly in that they are prepended by “`lsst.`”.

3.1.1. Raw Image

raw images (NSF-DOE Vera C. Rubin Observatory 2025b) are unprocessed data received directly from the camera. Each **raw** corresponds to a single CCD from a single LSSTComCam exposure of 30 s duration. Each LSSTComCam exposure typically produces up to nine **raws**, one per sensor in the focal plane. However, a small number of exposures resulted in fewer than nine **raw** images due to temporary hardware issues or readout faults.

In total, DP1 includes 16125 raw images. Table 4 provides a summary by target and band. A **raw** contains 4608×4096 pixels, including prescan and overscan, and occupies around 18 MB of disk space.⁹² The field of view of a single **raw**, excluding prescan and overscan regions, is roughly $0^\circ 23' \times 0^\circ 22' \approx 0.051 \text{ deg}^2$, corresponding to a plate scale of $0''.2$ per pixel.

⁹² Each amplifier image contains 3 and 64 columns of serial prescan and overscan pixels, respectively, and 48 rows of parallel overscan pixels, meaning a **raw** contains 4072×4000 exposed pixels.

3.1.2. Visit Image

`visit_images` (NSF-DOE Vera C. Rubin Observatory 2025c) are fully-calibrated processed images. They have undergone instrument signature removal (§4.2.1) and all the single frame processing steps described in §4.2 which are, in summary: PSF modeling, background subtraction, and astrometric and photometric calibration. As with **raws**, a `visit_image` contains processed data from a single CCD resulting from a single 30 s LSSTComCam exposure. As a consequence, a single LSSTComCam exposure typically results in nine `visit_images`. The handful of exposures with fewer than nine **raw** images also have fewer than nine `visit_images`, but there are an additional 153 **raw** images that failed processing and for which there is thus no corresponding `visit_image`. The majority of failures – 131 in total – were due to challenges with astrometric fits or PSF models in the 47_Tuc crowded field. The other failures were in the Rubin_SV_095_-25 (9 failures), ECDFS (8), Fornax_dSph (3), and EDFs_comcam (2) fields.

In total, there are 15972 `visit_images` in DP1. Each `visit_image` comprises three images: a calibrated science image, a variance image, and a pixel-level bit-mask that flags issues such as saturation, cosmic rays, or other artifacts. Each `visit_image` also contains a position-dependent PSF model, World Coordinate System (WCS) information, and various metadata providing information about the observation and processing. The science and variance images and the pixel mask each contain 4072×4000 pixels. In total, a single `visit_image`, including all extensions and metadata, occupies around 110 MB of disk space. A plot showing the normalized cumulative histogram of the 5σ depths of all the `visit_images` in DP1 is shown in Figure 8.

3.1.3. Deep Coadd

`deep_coadds` are created on a per-band basis, meaning only data from exposures taken with a common filter are coadded. As such, there are up to six `deep_coadds` covering each `patch` – one for each of the six LSSTComCam bands. The process of producing `deep_coadds` is described in §4.5 but, to summarize, it involves the selection of suitable `visit_images` (both in terms of `patch` coverage, band, and image quality), the warping of those `visit_images` onto a common pixel grid, and the co-adding of the warped `visit_images`. To be included in a DP1 `deep_coadd`, a `visit_image` needed to have a PSF FWHM smaller than $1''.7$. Of the 15972 `visit_images`, 15375 satisfied this criterion and were therefore used to create `deep_coadds`.

There are a total of 2644 `deep_coadds` in DP1. As mentioned above, a single `deep_coadd` covers one `patch`,

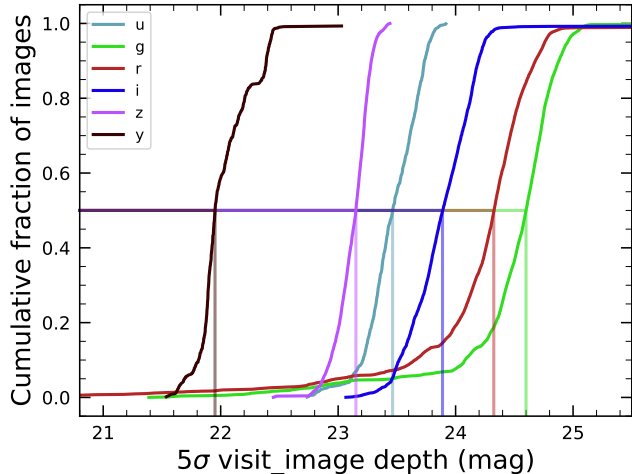


Figure 8. Normalized cumulative histograms of the 5σ depths of all `visit_images` in each band. The vertical lines indicate the 50th percentiles for each band (see legend).

and includes a small amount of overlap with its neighboring `patch`. The skymap used for DP1 defines a `patch` as having an on-sky area of 0.028 deg^2 excluding overlap, and 0.036 deg^2 including overlap. A single `deep_coadd` – including overlap – contains 3400×3400 equal-sized pixels, corresponding to a platescale of $0''.2$ per pixel. Each `deep_coadd` contains the science image (i.e., the coadd), a variance image, and a pixel mask; all three contain the same number of pixels. Each `deep_coadd` also contains a position-dependent PSF model (which is the weighted sum of the PSF models of the input `visit_images`), WCS information, plus various `meta-data`.

The number of `visit_images` that contributed to a given `deep_coadd` varies across the patch; the Survey Property Maps can be consulted to gain insights into the total exposure time at all locations covered by the survey. Similarly, since coadds always cover an entire `patch`, it is common for a `deep_coadd` to contain regions that were not covered by any of the selected `visit_images`, particularly if the `patch` is on the outskirts of a field and was thus not fully observed. By the nature of how coadds are produced, such regions may contain seemingly valid `flux` values (i.e., not necessarily zeros or NaNs), but will instead be flagged with the `NO_DATA` flag in the pixel mask. It is therefore crucial that the pixel mask be referred to when analyzing `deep_coadds`.

3.1.4. Template Coadd

`template_coadds` (NSF-DOE Vera C. Rubin Observatory 2025d) are those created to use as templates for difference imaging, i.e., the process of subtracting a template image from a `visit_image` to identify either vari-

able or `transient` objects. It should be noted, however, that `template_coadds` are not themselves subtracted from `visit_images` but are, instead, warped to match the WCS of a `visit_image`. It is this warped template that is subtracted from the `visit_image` to create a difference image.⁹³ As with `deep_coadds`, `template_coadds` are produced by warping and co-adding multiple `visit_images` covering a given skymap-defined `patch`. The process of building `template_coadds` is the same as that for `deep_coadds`, but the selection criteria differ between the two types of coadd. In the case of `template_coadds`, one third of `visit_images` covering the `patch` in question with the narrowest PSF FWHM are selected. If one third corresponds to fewer than twelve `visit_images` (i.e., there are fewer than 36 `visit_images` covering the `patch`), then the twelve `visit_images` with the narrowest PSF FWHM are selected. Finally, if there are fewer than twelve `visit_images` covering the `patch`, then all `visit_images` are selected. Of the 15972 `visit_images`, 13113 were used to create `template_coadds`. This selection strategy is designed to optimize for `seeing` when a `patch` is well-covered by `visit_images`, yet still enable the production of `template_coadds` for poorly-covered patches. As with `deep_coadds`, the number of `visit_images` that contributed to a `template_coadd` varies across the patch.

DP1 contains a total of 2730 `template_coadds`.⁹⁴ As with `deep_coadds`, a single `template_coadd` covers a single `patch`. Since the same skymap is used when creating both `deep_coadd` and `template_coadds`, the on-sky area and pixel count of `template_coadds` are the same as that of a `deep_coadd` (see above). Similarly, `template_coadds` contain the science image (i.e., the coadd), a variance image, and a pixel mask; all three contain the same number of pixels. Also included are the PSF model, WCS information, and `metadata`. As is the case for `deep_coadds`, those pixels within `template_coadds` that are not covered by any of the selected `visit_images` may still have seemingly valid values, but are indicated with the `NO_DATA` flag within the pixel mask.

3.1.5. Difference Image

`difference_images` (NSF-DOE Vera C. Rubin Observatory 2025e) are generated by the subtraction of the warped, scaled, and PSF-matched `template_coadd`

⁹³ For storage space reasons, warped templates are not retained for DP1, as they can be readily and reliably recreated from the `template_coadds`.

⁹⁴ The difference in the number of `deep_coadds` and `template_coadds` is due to the difference in the `visit_image` selection criteria for each coadd.

from the `visit_image` (see §4.6.1). In principle, only those sources whose `flux` has changed relative to the `template_coadd` should be apparent (at a significant level) within a `difference_image`. In practice, however, there are numerous spurious sources present in `difference_images` due to unavoidably imperfect template matching.

In total, there are 15972 `difference_images` in DP1, one for each `visit_image`.

Like `visit_images`, `difference_images` contain the science (i.e., difference) image, a variance image, and a pixel mask; all three contain the same number of pixels, which is the same as that of the input `visit_image`. Also included is the PSF model, WCS information, and `metadata`.

3.1.6. Background Images

Background images contain the model `background` that has been generated and removed from a science image. `visit_images`, `deep_coadds` and `template_coadds` all have associated `background` images.⁹⁵ Background images contain the same number of pixels as their respective science image, and there is one `background` image for each `visit_image`, `deep_coadd`, and `template_coadd`. Difference imaging analysis also measures and subtracts a `background` model, but the `difference_background` data product is not written out by default and is not part of DP1.

Background images are not available via the IVOA Service; they can only be accessed via the Butler Data Service.

3.2. Catalogs

In this section we describe science-ready tables produced by the science pipelines. All catalogs contain data for detections in the images described in §3.1, except the `Calibration` catalog, which contains reference data obtained from previous surveys. Observatory-produced `metadata` tables are described in §3.5.

The catalogs contains measurements for either Sources detected in `visit_images` and `difference_images`, or Objects detected in `deep_coadds`. All catalogs store fluxes rather than magnitudes, with fluxes measured in nanojansky ($1 \text{ nJy} = 10^{-35} \text{ Wm}^{-2}\text{Hz}^{-1}$). Fluxes are preferred for multi-epoch observations, as they can be averaged across epochs, unlike magnitudes. Additionally, flux measurements on difference images (§3.1) are computed against a template, representing a flux difference. As a result, flux measurements on difference

images can be negative, particularly for faint sources in the presence of noise.

The `Source`, `Object`, `ForcedSource`, `DiaSource`, `DiaObject`, and `ForcedSourceOnDiaObject` catalogs described below each vary in terms of their specific columns but generally contain: one or more unique identification numbers, positional information, multiple types of `flux` measurements (e.g., aperture fluxes, PSF fluxes, Gaussian fluxes, etc.), and a series of boolean flags indicating characteristics such as saturation or cosmic ray contamination for each source/object. The Solar System catalogs `SSObject` and `SSSource` deviate from this general structure in that they instead contain orbital parameters for all known asteroids.

Where applicable, quantities are prefixed with the band in which they were measured, and all measured properties are reported with their associated 1σ uncertainties. For example, `g_ra` and `g_raErr` refer to right ascension and its uncertainty, measured in the g-band.

Fluxes for various apertures are provided together with an uncertainty and a flag, and named in the format `[band]_ap[size]Flux`, where `[size]` is the aperture diameter in pixels. For example, `g_ap03Flux`, `g_ap03FluxErr`, `g_ap03Flux_flag` provide the flux, uncertainty and flag measured within a 3.0-pixel aperture in the g-band. Similarly for flux measurements using difference algorithms, e.g. `g_psfFlux` provides the flux derived using the PSF model as a weight function, forced on g-band.

A complete list of columns with description and units for all tables in DP1 is available at <https://sdm-schemas.lsst.io/dp1.html> Since DP1 is a preview release, it does not include all the catalogs expected in a full LSST Data Release. Additionally, some catalogs may be missing columns, as not all quantities have been computed yet. These quantities will be included in future releases, and, where it is known to be the case, missing data are noted in the catalog descriptions that follow.

Catalog data are stored in the Qserv database (§6.5.1) and are accessible via Table Access Protocol (IVOA standard) (IVOA), and an online DP1 catalog schema is available at <https://sdm-schemas.lsst.io/dp1.html>. Catalog data are also accessible via the Data Butler (see §6.2.2).

3.2.1. Source Catalog

The `Source` catalog (NSF-DOE Vera C. Rubin Observatory 2025f) contains data on all sources which are, prior to deblending (§4.5.2), detected with a greater than 5σ significance in each individual visit. The detections reported in the `Source` catalog have undergone deblending; in the case of blended detections, only the

⁹⁵ In future data releases, `background` images may be included as part of their respective science image data product.

deblended sources are included in the `Source` catalog. It is important to note that while the criterion for inclusion in a `Source` catalog is a $> 5\sigma$ detection in a `visit_image` prior to deblending, the positions and fluxes are reported post-deblending. Hence, it is possible for the `Source` catalog to contain sources whose `flux-to-error` ratios – potentially of all types (i.e., aperture `flux`, `PSF flux`, etc.) – are less than 5.

In addition to the general information mentioned above (i.e., IDs, positions, fluxes, flags), the `Source` catalog also includes basic `shape` and extendedness information.

The `Source` catalog contains data for 46 million sources in DP1.

A cumulative histogram showing the PSF magnitudes of all sources contained within the `Source` catalogue is presented in the top panel of Figure 9

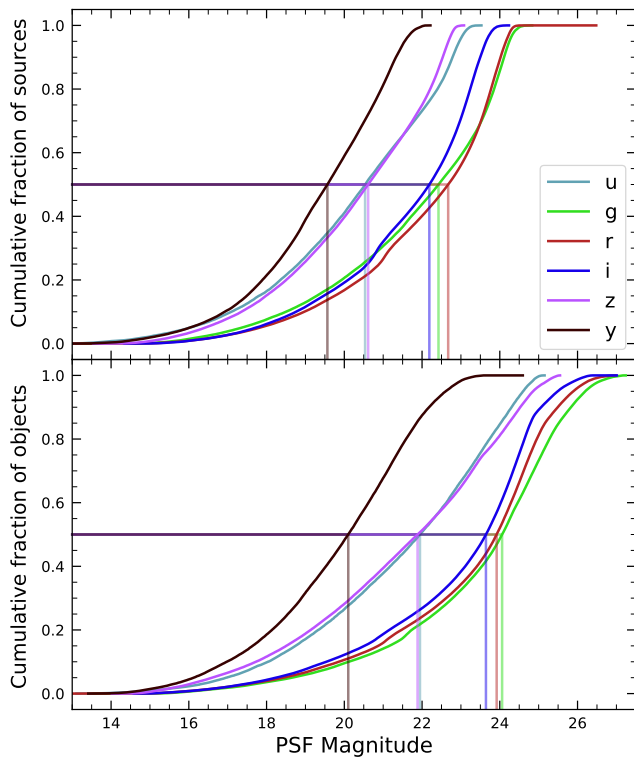


Figure 9. Normalized cumulative histograms of the PSF magnitudes of all $> 5\sigma$ -detected `sources` (top panel) and `objects` (bottom panel) contained in the `Source` and `Object` catalogs, respectively, separated according to band (see legend). The vertical lines indicate the 50th percentile for each band.

3.2.2. Object Catalog

The `Object` catalog (NSF-DOE Vera C. Rubin Observatory 2025g) contains data on all objects detected with a greater than 5σ significance in the `deep_coadds`.

With `coadd` images produced on a per-band basis, a $> 5\sigma$ detection in one or more of the bands will result in an object being included in the `Object` catalog. For cases where an object is detected at $> 5\sigma$ in more than one band, a cross-matching has been performed between bands to associate an object in one band with its counterpart(s) in the other bands. As such, the `Object` catalog contains data from multiple bands. The objects reported in the `Object` catalog have also undergone deblending; in the case of blended detections, only the deblended child objects are included in the catalog. As with the `Source` catalog, the criterion for inclusion in the `Object` catalog is a $> 5\sigma$ detection in one of the `deep_coadds` prior to deblending, yet the positions and fluxes of objects are reported post-deblending. Hence, it is possible for `Object` catalog to contain `objects` whose `flux-to-error` ratios — potentially of all types and in all bands — are less than 5.

In addition to the general information mentioned above (i.e., IDs, positions, fluxes, flags), the `Object` catalog also includes basic `shape` and extendedness information. While they may be included in future data releases, no photometric redshifts, Petrosian magnitudes (V. Petrosian 1976), proper motions or periodicity information are included in the DP1 object catalogs.

The `Object` catalog contains data for 2.3 million objects in DP1.

3.2.3. ForcedSource Catalog

The `ForcedSource` catalog (NSF-DOE Vera C. Rubin Observatory 2025h) contains forced PSF photometry measurements performed on both `difference_images` (i.e., the `psfDiffFlux` column) and `visit_images` (i.e., the `psfFlux` column) at the positions of all the objects in the `Object` catalog, to allow assessment of the time variability of the fluxes. We recommend using the `psfDiffFlux` column when generating light curves because this quantity is less sensitive to `flux` from neighboring sources than `psfFlux`. In addition to `forced photometry PSF fluxes`, a number of boolean flags are also included in the `ForcedSource` catalog.

The `ForcedSource` catalog contains a total of 269 million entries across 2.3 million unique objects.

3.2.4. DiaSource Catalog

The `DiaSource` catalogs (NSF-DOE Vera C. Rubin Observatory 2025i) contains data on all the sources detected at $> 5\sigma$ significance — including those associated with known Solar System objects — in the `difference_images`. Unlike sources detected in `visit_images`, sources detected in difference images (hereafter, “DiaSource”) have gone through an association step in which an attempt has been made to associate them into

underlying objects called “DiaObject”. The `DiaSource` catalog consolidates all this information across multiple visits and bands. The detections reported in the `DiaSource` catalog have not undergone deblending.

The `DiaSource` catalog contains data for 3.1 million `DiaSources` in [DP1](#).

3.2.5. *DiaObject Catalog*

The `DiaObject` catalog ([NSF-DOE Vera C. Rubin Observatory 2025j](#)) contains the astrophysical objects that `DiaSources` are associated with (i.e., the `DiaObjects`). The `DiaObject` catalog contains only non-Solar System Objects; Solar System Objects are, instead, recorded in the `SSObject` catalog. When a `DiaSource` is identified, the `DiaObject` and `SSObject` catalogs are searched for objects to associate it with. If no association is found, a new `DiaObject` is created and the `DiaSource` is associated to it. Along similar lines, an attempt has been made to associate `DiaObjects` across multiple bands, meaning the `DiaObject` catalog, like the `Object` catalog, contains data from multiple bands. Since `DiaObjects` are typically [transient](#) or variable (by the nature of their means of detection), the `DiaObject` catalog contains summary statistics of their fluxes, such as the mean and standard deviation over multiple epochs; users must refer to the `ForcedSourceOnDiaObject` catalog (see below) or the `DiaSource` catalog for single [epoch flux](#) measurements of `DiaObjects`.

The `DIAObject` catalog contains data for 1.1 million `DiaObjects` in [DP1](#).

3.2.6. *ForcedSourceOnDiaObject Catalog*

The `ForcedSourceOnDiaObject` catalog ([NSF-DOE Vera C. Rubin Observatory 2025k](#)) is equivalent to the `ForcedSource` catalog, but contains [forced photometry](#) measurements obtained at the positions of all the `DiaObjects` in the `DiaObject` catalog.

The `ForcedSourceOnDiaObject` catalog contains a total of 197 million entries across 1.1 million unique `DiaObjects`.

3.3. *SSObject Catalog*

The `SSObject` catalog ([NSF-DOE Vera C. Rubin Observatory 2025l](#)) and the [Minor Planet Center Orbit database \(MPCORB\)](#) carry information about solar system objects. The `MPCORB` table provides the [Minor Planet Center](#)-computed orbital elements for all known asteroids, including those that Rubin discovered. For [DP1](#), the `SSObject` catalog serves primarily to provide the mapping between the [International Astronomical Union \(IAU\)](#) designation of an object (listed in `MPCORB`), and the internal `ssObjectId` identifier,

which is used as a key to find solar system object observations in the `DiaSource` and `SSSource` tables. The `SSObject` catalog contains data for 431 `SSObjects` in [DP1](#).

3.3.1. *SSSource Catalog*

The `SSSource` catalog ([NSF-DOE Vera C. Rubin Observatory 2025m](#)) contains data on all `DiaSources` that are either associated with previously-known Solar System Objects, or have been confirmed as newly-discovered Solar System Objects by confirmation of their orbital properties. As entries in the `SSSource` catalog stem from the `DiaSource` catalog, they have all been detected at $> 5\sigma$ significance in at least one band. The `SSSource` catalog contains data for 5988 Solar System Sources.

3.3.2. *CcdVisit Catalog*

The `CcdVisit` catalog ([NSF-DOE Vera C. Rubin Observatory 2025n](#)) contains data for all `CCD` images from a single visit. In principle, this means nine entries per visit, however due to a variety of technical reasons, not all `CCDs` have data for each visit, and so the catalog may contain fewer than nine entries per visit. In addition to technical information, such as the on-sky coordinates of the central pixel and measured pixel scale, the `CcdVisit` catalog contains a range of data quality measurements, such as whole-image summary statistics for the `PSF` size, zeropoint, sky [background](#), sky noise, and quality of astrometric solution. It provides an efficient method to access `visit_image` properties without needing to access the image data. When combined with the data contained in the `Visit` table described in [§3.5](#), it provides a full picture of the telescope pointing and sky conditions at the time of observation.

The `CcdVisit` catalog contains 16071 entries (nine entries for each of the 1786 visits, minus three entries for one incomplete visit). This differs from the number of `visit_images` due to the more stringent requirements imposed to generate a science-ready image.

3.3.3. *Calibration Catalog*

The `Calibration` catalog is the reference catalog that was used to perform astrometric and photometric [calibration](#). It is a whole-sky catalog built specifically for [LSST](#), as no single prior reference catalog had both the depth and coverage needed to calibrate [LSST](#) data. It combines data from multiple previous reference catalogs and contains only stellar sources. Full details on how the `Calibration` catalog was built are provided in [P. S.](#)

Ferguson et al. (2025)⁹⁶. We provide a brief summary here.

For the *grizy* bands, the input catalogs were (in order of decreasing priority): Dark Energy Survey (DES) Y6 Calibration Stars (E. S. Rykoff et al. 2023); Gaia-B or R Photometry (Gaia) (XP) Synthetic Magnitudes (Gaia Collaboration et al. 2023a); the Panoramic Survey Telescope and Rapid Response System (Pan-STARRS)1 3PI Survey (K. C. Chambers et al. 2016); Data Release 2 of the SkyMapper survey (C. A. Onken et al. 2019); and Data Release 4 of the VLT Survey Telescope (VST) Asteroid Terrestrial-impact Last Alert System (ATLAS) survey (T. Shanks et al. 2015). For the *u*-band, the input catalogs were (in order of decreasing priority): Standard Stars from Sloan Digital Sky Survey (SDSS) Data Release 16 (R. Ahumada et al. 2020); Gaia-XP Synthetic Magnitudes (Gaia Collaboration et al. 2023a); and synthetic magnitudes generated using Single Lens Reflex (SLR), which estimates the *u*-band flux from the *g*-band flux and *g-r* colors. This SLR estimates were used to boost the number of *u*-band reference sources, as otherwise the source density from the *u*-band input catalogs is too low to be useful for the LSST.

Only stellar sources were selected from each input catalog. Throughout, the Calibration catalog uses the DES bandpasses for the *grizy* bands and the SDSS bandpass for the *u*-band; color transformations derived from high quality sources were used to convert fluxes from the various input catalogs (some of which did not use the DES/SDSS bandpasses) to the respective bandpasses. All sources from the input catalogs are matched to Gaia-Data Release 3 (DR3) sources for robust astrometric information, selecting only isolated sources (i.e., no neighbors within 1").

After collating the input catalogs and transforming the fluxes to the standard DES/SDSS bandpasses, the catalog was used to identify sources within a specific region of the sky. This process generated a set of standard columns containing positional and flux information, along with their associated uncertainties.

3.3.4. Source and Object Designations

To refer to individual sources or objects from the DP1 catalogs, one should follow the LSST DP1 naming convention that has been registered with the International Astronomical Union. Because the Source, Object, DiaSource, DiaObject, and SSObject tables each have their own unique IDs, their designations should differ.

In general, source and object designations should begin with the string “LSST-DP1” (denoting the Legacy Survey of Space and Time, Data Preview 1), followed by a string specifying the table from which the source was obtained. These strings should be “O” (for the Object table), “S” (Source), “DO” (DiaObject), “DS” (DiaSource), or “SSO” (SSObject). Following the table identifier, the designation should contain the full unique numeric identifier from the specified table (i.e., the objectId, sourceId, diaObjectId, diaSourceId, or ssObjectId). Each component of the identifier should be separated by dashes, resulting in a designation such as “LSST-DP1-TAB-123456789012345678”. In summary, source designations should adhere to the formats listed below:

- Object: LSST-DP1-O-609788942606161356 (for objectId 609788942606161356)
- Source: LSST-DP1-S-600408134082103129 (for sourceId 600408134082103129)
- DiaObject: LSST-DP1-DO-609788942606140532 (for diaObjectId 609788942606140532)
- DiaSource: LSST-DP1-DS-600359758253260853 (for diaSourceId 600359758253260853)
- SSObject: LSST-DP1-SSO-21163611375481943 (for ssObjectId 21163611375481943)

Tables that were not explicitly mentioned in the description above do not have their own unique IDs, but are instead linked to one of the five tables listed above via a unique ID. For example, the ForcedSource table uses objectId, ForcedSourceOnDiaObject uses diaObjectId, SSSource uses diaSourceId and ssObjectId, and MPCORB uses ssObjectId.

3.4. Maps

Maps are two-dimensional visualizations of survey data. In DP1, these fall into two categories: Survey Property Maps and Hierarchical Progressive Survey (HiPS) Maps (P. Fernique et al. 2015).

3.4.1. Survey Property Maps

Survey Property Maps (NSF-DOE Vera C. Rubin Observatory 2025o) summarize how properties such as observing conditions or exposure time vary across the observed sky. Each map provides the spatial distribution of a specific quantity at a defined sky position for each band by aggregating information from the images used to make the deep_coadd. Maps are initially created per-tract and then combined to produce a final consolidated

⁹⁶ In P. S. Ferguson et al. (2025), the calibration reference catalog is referred to as “The Monster”. This terminology is also carried over to the DP1 Butler.

map. At each sky location, represented by a spatial pixel in the [Hierarchical Equal-Area iso-Latitude Pixelisation \(HEALPix\)](#) (K. M. Górski et al. 2005) grid, values are derived using statistical operations, such as minimum, maximum, mean, weighted mean, or sum, depending on the property.

DP1 contains 14 survey property maps. The available maps describe total exposure times, observation epochs (one each for the earliest, mean, and latest observation epoch), PSF size and *shape* (one for each of the e^1 and e^2 shape parameters; see §5.2), PSF magnitude limits, sky *background* and noise levels, as well as astrometric shifts (one each for right ascension and declination) and PSF distortions (one for each of the e^1 and e^2 shape parameters) due to wavelength-dependent atmospheric [Differential Chromatic Refraction \(DCR\)](#) effects. They all use the dataset type format `deep_coadd_<PROPERTY>_consolidated_map_<STATISTIC>`. For example, `deep_coadd_exposure_time_consolidated_map_sum` provides a spatial map of the total exposure time accumulated per sky position in units of seconds. All maps are stored in [HealSparse](#)⁹⁷ format. Survey property maps are only available via the [Data Butler](#) (§6.2.2).

Figure 10 presents three survey property maps for exposure time, PSF magnitude limit, and sky noise, computed for representative tracts and bands. Because full consolidated maps cover widely separated tracts, we use clipped *per-tract* views here to make the spatial patterns more discernible.

3.4.2. HiPS Maps

HiPS Maps (P. Fernique et al. 2015), offer an interactive way to explore seamless, multi-band tiles of the sky regions covered by DP1, allowing for smooth panning and zooming. DP1 provides multi-band HiPS images created by combining data from individual bands of `deep_coadd` and `template_coadd` images, using an improved version (Lust et al. in prep) of the algorithm presented in R. Lupton et al. (2004). These images are false-color representations generated using various filter combinations for the red, green, and blue channels.

The available filter combinations include *gri*, *izy*, *riz*, and *ugr* for both `deep_coadd` and `template_coadd`. Additionally, for `deep_coadd` only, we provide color blends such as *uug* and *grz*. Post-DP1, we plan to also provide single-band HiPS images for all *ugrizy* bands in both [Portable Network Graphics \(PNG\)](#) and [FITS](#) formats.

HiPS maps are only accessible through the HiPS viewer in the [RSP Portal](#) (§6.3) and cannot be accessed via the [Data Butler](#) (§6.2.2). All multi-band HiPS images are provided in [PNG](#) format.

3.5. Metadata

DP1 also includes *metadata* about the observations, which are stored in the `Visit` table. We distinguish it from a catalog as the data it contains was produced by the observatory directly, rather than the science pipelines. The `Visit` table contains technical data for each visit, such as telescope pointing, camera rotation, *airmass*, exposure start and end time, and total exposure time. Some of the information contained within the `Visit` table is also contained in the `CCDVisit` catalogue described in §3.2 (e.g., exposure time), although the latter also includes information produced by the processing pipelines at a per-detector level, such as the PSF size and limiting magnitudes of a given `visit_image`.

3.6. Ancillary Data Products

DP1 also includes several ancillary data products. While we do not expect most users to need these, we describe them here for completeness. All the Data Products described in this section can only be accessed via the [Data Butler](#) (§6.2.2).

3.6.1. Standard Bandpasses

Figure 3 shows the full-system throughput of the six [LSSTComCam](#) filters. The corresponding transmission curves are provided as a DP1 data product. These datasets tabulate the full-system transmission of the six [LSSTComCam](#) filters as a function of wavelength and were used as a reference for the [LSSTComCam DP1](#) photometry. The `standard_passband` dataset is keyed by band and is stored in [Astropy Table](#) format.

3.6.2. Task configuration, log, and metadata

DP1 includes *provenance*-related data products such as task logs, *configuration* files, and task metadata. Configuration files record the parameters used in each processing task, while logs and *metadata* contain information output during processing. These products help users understand the processing setup and investigate potential processing failures.

3.6.3. Calibration Data Products

Calibration data products include a variety of images and models that are used to characterize and correct the performance of the camera and other system components. These include bias, dark, and flat-field images,

⁹⁷ A sparse [HEALPix](#) representation that efficiently encodes data values on the celestial sphere. <https://healsparse.readthedocs.io>

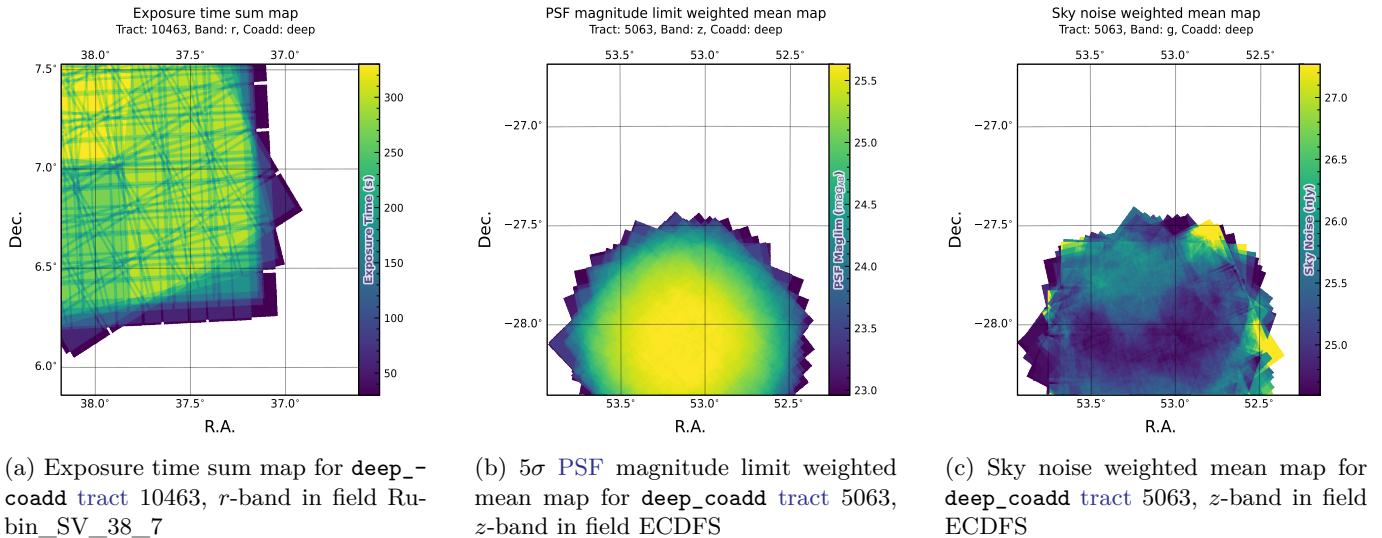


Figure 10. Examples of survey property maps from Rubin DP1 across different bands, clipped to the boundary of a single tract for visual clarity.

Photon Transfer Curve (PTC) gains, brighter-fatter kernels (P. Antilogus et al. 2014), charge transfer inefficiency (CTI) models, linearizers, and illumination corrections. For flat-field corrections, DP1 processing used combined flats, which are averaged from multiple individual flat-field exposures to provide a stable calibration. These calibration products are essential inputs to Instrument Signal Removal (ISR) (§4.2.1). While these products are included in DP1 for transparency and completeness, users should not need to rerun ISR for their science and are advised to start with the processed `visit_image`.

4. DATA RELEASE PROCESSING

Data Release Processing (DRP) is the systematic processing of all Rubin Observatory data collected up to a certain date to produce the calibrated images, catalogs of detections, and derived data products described in Section 3. DP1 was processed entirely at the United States Data Facility (USDF) at SLAC using 17,024 CPU hours.⁹⁸

This section describes the pipeline algorithms used to produce DP1 and how they differ from those planned for full-scale LSST data releases. Data Release Production consists of four major stages: (1) single-frame processing, (2) calibration, (3) coaddition, and (4) difference image analysis (DIA).

⁹⁸ For future Data Releases, data processing will be distributed across the USDF, the French (FrDF) and UK (UKDF) data facilities.

4.1. LSST Science Pipelines Software

The LSST Science Pipelines software (Rubin Observatory Science Pipelines Developers 2025; J. D. Swinbank et al. 2020) will be used to generate all Rubin Observatory and LSST data products. They provide both the algorithm and middleware frameworks necessary to process raw data into science-ready data products, enabling analysis by the Rubin scientific community. Version v29.1 of the pipelines was used to produce DP1⁹⁹.

4.2. Single Frame Processing

4.2.1. Instrument Signature Removal

The first step in processing LSSTComCam images is to correct for the effects introduced by the telescope and detector. Each sensor and its readout amplifiers can vary slightly in performance, causing images of even a uniformly illuminated focal plane to exhibit discontinuities and shifts due to detector effects. The ISR pipeline aims to recover the original astrophysical signal as best as possible and produce science-ready single-epoch images for source detection and measurement. A detailed description of the ISR procedures can be found in P. Fagrellius & E. S. Rykoff (2025) and A. A. Plazas Malagón et al. (2025). Figure 11 illustrates the model of detector components and readout electronics and their impact on the signal, tracing the process from photons incident on the detector surface to the final quantized values¹⁰⁰ recorded in the image files. The ISR pipeline essen-

⁹⁹ Documentation for this version is available at https://pipelines.lsst.io/v/v29_1_1

¹⁰⁰ The images written to disk by the camera have values that are integers that come from the ADC converting an analog voltage.

tially “works backward” through the signal chain, correcting the integer analog-to-digital units (ADU) raw camera output back to a floating-point number of photoelectrons created in the silicon. The physical detector, represented on the left in Figure 11, is the source of effects that arise from the silicon itself, such as the dark current and the brighter-fatter effect (A. A. Plazas et al. 2018; A. Broughton et al. 2024). After the integration time has elapsed, the charge is shifted to the serial register and read out, which can introduce charge transfer inefficiencies and a clock-injected offset level. The signals for all amplifiers are transferred via cables to the Readout Electronics Board (REB), during which crosstalk between the amplifiers may occur. The Analog Signal Processing Integrated Circuit (ASPIC) on the REB converts the analog signal from the detector into a digital signal, adding both quantization and a bias level to the image. Although the signal chain is designed to be stable and linear, the presence of numerous sources of non-linearity indicates otherwise.

The ISR processing pipeline for DP1 performs, in the following order: Analogue-to-Digital Unit (ADU) dithering to reduce quantization effects, serial overscan subtraction, saturation masking, gain normalization, crosstalk correction, parallel overscan subtraction, linearity correction, serial CTI correction, image assembly, bias subtraction, dark subtraction, brighter-fatter correction, defect masking and interpolation, variance plane construction, flat fielding, and amplifier offset (amp-offset) correction¹⁰¹. Flat fielding for DP1 was performed using combined flats produced from twilight flats acquired with sufficient rotational dithering to mitigate artifacts from print-through stars, as described in §2.3.

¹⁰¹ Amp-offset corrections are designed to address systematic discontinuities in background sky levels across amplifier boundaries. The implementation in the LSST Science Pipelines is based on the Pan-STARRS Pattern Continuity algorithm (C. Z. Waters et al. 2020).

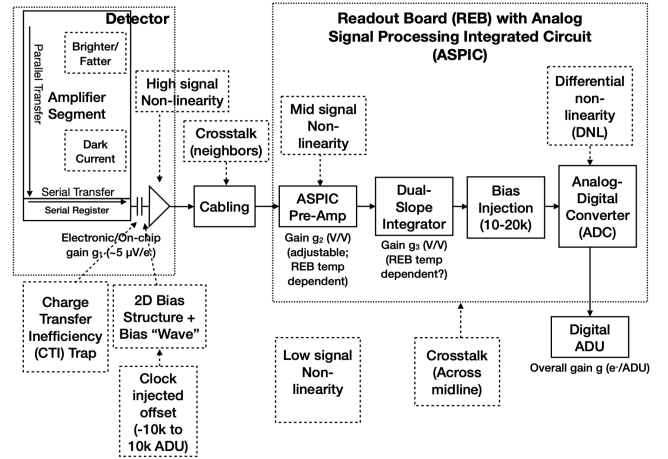


Figure 11. The model of the detector and REB components, labeled with the effects that they impart on signal.

4.2.2. Background Subtraction

The background subtraction algorithms in the LSST Science Pipelines estimate and remove large-scale background signals from science imaging. Such signals may include sky brightness from airglow, moonlight, scattered light instrumental effects, zodiacal light, and diffuse astrophysical emission. In so doing, true astrophysical sources are isolated to allow for accurate detection and measurement.

To generate a background model, each post-ISR image is divided into superpixels of 128×128 pixels. Pixels with a mask flag set that indicates that they contain no useful science data or that they contain flux from a preliminary source detection are masked. The iterative 3σ clipped mean of the remaining pixels is calculated for each superpixel, constructing a background statistics image. A sixth-order Chebyshev polynomial is fit to these values on the scale of a single detector to allow for an extrapolation back to the native pixel resolution of the post-ISR image.

4.3. Calibration

Stars are detected in each post-ISR image using a 5σ threshold. Detections of the same star across multiple images are then associated to identify a consistent set of isolated stars with repeated observations suitable for use in PSF modeling, photometric calibration, and astrometric calibration.

Initial astrometric and photometric solutions are derived using only the calibration reference catalogs (see §3.2), and an initial PSF model is fit using PSFEx (E. Bertin 2011). These preliminary solutions provide approximate source positions, fluxes, and PSF shapes that serve as essential inputs to the calibration process, en-

abling reliable source matching, selection of high-quality stars, and iterative refinement of the final astrometric, photometric, and PSF models. These preliminary solutions are subsequently replaced by more accurate fits, as described in the following sections.

4.3.1. PSF Modeling

PSF modeling in DP1 uses the Piff (M. Jarvis et al. 2021) package. Our configuration of Piff utilizes its `PixelGrid` model with a fourth-order polynomial interpolation per CCD, except in the *u*-band, where star counts are insufficient to support a fourth-order fit. In this case, a second-order polynomial is used instead. Details on the choice of polynomial order, overall PSF modeling performance, and known issues are discussed in §5.2.

4.3.2. Astrometric Calibration

Starting from the astrometric solution calculated in single frame processing (§4.2), the final astrometric solution is computed using the ensemble of visits in a given band that overlap a given tract. This allows the astrometric solution to be further refined by using all of the isolated point sources of sufficient signal-to-noise ratio in an image, rather than only those that appear in the reference catalog, as is done in single frame processing. Using multiple whole visits rather than a single detector also allows us to account for effects that impact the full focal plane, and for the proper motion and parallax of the sources.

In order to perform the fit of the astrometric solution, isolated point sources are associated between overlapping visits and with the Gaia DR3 (Gaia Collaboration et al. 2023b) reference catalog where possible. The model used for DP1 consists of a static map from pixel space to an intermediate frame (the per-detector model), followed by a per-visit map from the intermediate frame to the plane tangent to the telescope boresight (the per-visit model), then finally a deterministic mapping from the tangent plane to the sky. The fit is done using the `gbdes` package (G. M. Bernstein et al. 2017), and a full description is given in C. Saunders (2024).

The per-detector model is intended to capture quasi-static characteristics of the telescope and camera. During Rubin Operations, the astrometric solution will allow for separate epochs with different per-detector models, to account for changes in the camera due to warming and cooling and other discrete events. However, for DP1, LSSTComCam was assumed to be stable enough that all visits use the same per-detector model. The model itself is a separate two-dimensional polynomial for each detector. For DP1, a degree 4 polynomial was used; the degree of the polynomial mapping is tuned for each

instrument and may be different for LSSTCam. Further improvements may be made by including a pixel-based astrometric offset mapping, which would be fit from the ensemble of astrometric residuals, but this is not included in the DP1 processing.

The per-visit model attempts to account for the path of a photon from both atmospheric sources and those dependent on the telescope orientation. This model is also a polynomial mapping, in this case a degree 6 two-dimensional polynomial. Correction for DCR (§5.4) was not done for DP1, but will be included in LSSTCam processing during Rubin Operations. Future processing will also likely include a Gaussian Process fit to better account for atmospheric turbulence, as was demonstrated by W. F. Fortino et al. (2021) and P. F. Léget et al. (2021).

The final component of the astrometric calibration involves the positions of the isolated point sources included in the fit, which are described by five parameters: sky coordinates, proper motion, and parallax. While proper motions and parallaxes are not released for DP1, they are fitted for these sources in the astrometric solution to improve the astrometric calibration.

4.3.3. Photometric Calibration

Photometric calibration of the DP1 dataset is based on the Forward Global Calibration Method (FGCM) (D. L. Burke et al. 2018), adapted for the LSST Science Pipelines (H. Aihara et al. 2022; P. Fagrelius & E. S. Rykoff 2025). We used the FGCM to calibrate the full DP1 dataset with a forward model that uses a parameterized model of the atmosphere as a function of airmass along with a model of the instrument throughput as a function of wavelength. The FGCM process typically begins with measurements of the instrumental throughput, including the mirrors, filters, and detectors. However, because full scans of the LSSTComCam as-built filters and individual detectors were not available, we instead used the nominal reference throughputs for the Simonyi Survey Telescope and LSSTCam.¹⁰² These nominal throughputs were sufficient for the DP1 calibration, given the small and homogeneous focal plane consisting of only nine ITL detectors. The FGCM atmosphere model, provided by MODTRAN (A. Berk et al. 1999), was used to generate a look-up table for atmospheric throughput as a function of zenith distance at Cerro Pachón. This model accounts for absorption and scattering by molecular constituents of the atmosphere, including O_2 and O_3 ; absorption by water vapor; and Mie scattering by airborne aerosol particulates. Nightly

¹⁰² Available at: <https://github.com/lstt/throughputs/tree/1.9>

variations in the atmosphere are modeled by minimizing the variance in repeated observations of stars with a **Signal to Noise Ratio (SNR)** greater than 10, measured using “compensated aperture fluxes”. These fluxes include a local **background** subtraction (see §4.2.2) to mitigate the impact of **background** offsets. The model fitting process incorporates all six bands (*ugrizy*) but does not include any gray (achromatic) terms, except for a linear assumption of mirror reflectance degradation, which is minimal over the short duration of the **DP1** observation campaign. As an additional constraint on the fit, we use a subset of stars from the reference catalog (P. S. Ferguson et al. 2025), primarily to constrain the system’s overall throughput and establish the “absolute” calibration.

Photometric transformation relations between **LSST-Cam** and **LSSTComCam** systems and other photometric systems are under development and are provided in (M. N. Porter et al. 2026)

4.4. Visit Images and Source Catalogs

With the final **PSF** models, **WCS** solutions, and photometric calibrations in place, we reprocess each single-epoch image to produce a final set of calibrated visit images and source catalogs. Source detection is performed down to a 5σ threshold using the updated **PSF** models, followed by measurement of **PSF** and aperture fluxes. These catalogs represent the best single-epoch source characterization, but they are not intended for constructing light curves. For time-domain analysis, we recommend using the **forced photometry** tables described in §4.6.2.

4.5. Coaddition Processing

4.5.1. Coaddition

Only exposures with a **seeing** better than 1.7 arcseconds FWHM are included in the deep coadded images. For the template coadds, typically only the top third of visits with the best **seeing** are used (although see §3.1 for more details), resulting in an even tighter image quality cutoff for the template coadds. Exposures with poor **PSF** model quality, identified using internal diagnostics, are excluded to prevent contamination of the coadds with unreliable **PSF** estimates. The remaining exposures are combined using an inverse-variance weighted mean stacking **algorithm**.

To mitigate transient artifacts before coaddition, we apply the artifact rejection procedure described in Y. Al-Sayyad (2018) that identifies and masks features such as satellite trails, optical ghosts, and cosmic rays. It operates on a time series of **PSF**-matched images resampled onto a common pixel grid (“warps”) and leverages their

temporal behavior to distinguish persistent astrophysical sources from transient artifacts.

Artifact rejection uses both direct (where no **PSF**-matching is performed) and **PSF**-matched warps, homogenized to a standard **PSF** of 1.8 arcseconds FWHM, broadly consistent with the 1.7 arcsecond FWHM **seeing** threshold used in data screening. A sigma-clipped mean of the **PSF**-matched warps serves as a static sky model, against which individual warps are differenced to identify significant positive and negative residuals. Candidate artifact regions are classified as **transient** if they appear in less than a small percentage of the total number of exposures, with the threshold based on the number of visits, N , as follows:

- $N = 1$ or 2 : threshold = 0 (no clipping).
- $N = 3$ or 4 : threshold = 1.
- $N = 5$: threshold = 2.
- $N > 5$: threshold = $2 + 0.03N$.

Identified **transient** regions are masked before coaddition, improving image quality and reducing contamination in derived catalogs.

4.5.2. Detection, Deblending and Measurement

After constructing coadded images, sources are detected in each band, merged across bands, deblended, and measured to generate the final object catalogs (§3.2). For each coadd in all six bands, we perform source detection at a 5σ detection threshold and then adjust the background with a per-patch constant (coadds are built from background-subtracted images, but the deeper detection on coadds redefines what is considered source versus background). Detections across bands are merged in a fixed priority order, *irzygu*, to form a union detection catalog, which serves as input to deblending.

Deblending is performed using the **Scarlet Lite** algorithm, which implements the same model as **Scarlet** (P. Melchior et al. 2018), but operates on a single pixel grid. This allows the use of analytic gradients, resulting in greater computational speed and memory efficiency.

Object measurement is then performed on the deblended detection footprints in each band. Measurements are conducted in three modes: independent per-band measurements, forced measurements in each band, and multiband measurements.

Most measurement algorithms operate through a single-band plugin system, largely as originally described in J. Bosch et al. (2018). The same plugins are run separately for each object on a deblended image,

which uses the Scarlet model as a template to re-weight the original noisy coadded pixel values. This effectively preserves the original image in regions where objects are not blended, while dampening the noise elsewhere.

A reference band is chosen for each object based on detection significance and measurement quality using the same priority order as detection merging (*irzygu*) and a second round of measurements is performed in forced mode using the shape and position from the reference band to ensure consistent colors (J. Bosch et al. 2018).

Measurement algorithm outputs include object fluxes, centroids, and higher-order moments thereof like sizes and shapes. A variety of flux measurements are provided, from aperture fluxes and forward modeling algorithms.

Composite model (CModel) magnitudes (K. Abazajian et al. 2004; J. Bosch et al. 2018) are used to calculate the extendedness parameter, which functions as a star-galaxy classifier. Extendedness is a binary classifier that is set to 1 if the PSF model flux is less than 98.5% of the (free, not forced) CModel flux in a given band. Additionally, the extendedness in the reference band is provided as a separate column for convenience as a multiband star-galaxy classification, and is recommended generally but also specifically for objects with low signal-to-noise ratio in some bands.

Gaussian-Aperture-and-PSF (Gaussian Aperture and PSF (GAaP) K. Kuijken 2008; A. Kannawadi 2025) fluxes are provided to ensure consistent galaxy colors across bands. Sérsic model (J. L. Sérsic 1963; J. L. Sérsic 1968) fits are run on all available bands simultaneously (MultiProFit, D. S. Taranu 2025). The resulting Sérsic model fluxes are provided as an alternative to CModel and are intended to represent total galaxy fluxes. Like CModel, the Sérsic model is a Gaussian mixture approximation to a true Sérsic profile, convolved with a Gaussian mixture approximation to the PSF. Sérsic model fits also include a free centroid, with all other structural parameters shared across all bands. That is, the intrinsic model has no color gradients, but the convolved model may have color gradients if the PSF parameters vary significantly between bands.

CModel measurements use a double “shapelet” (A. Refregier 2003) PSF model with a single shared shape. The Sérsic fits are intended to use a double Gaussian with independent shape parameters for each component. Due to a pipeline misconfiguration, the Sérsic fits actually used the shapelet PSF parameters, with the higher-order terms ignored (since MultiProFit does not support shapelet PSFs). This bug is not expected to impact the galaxy fluxes significantly, since the higher-order shapelet PSF parameters tend to be small, and

the fix will be applied in future campaigns. Either way, the double Gaussian PSF parameters are included for each object.

Further details on the performance of these algorithms are found in §5.7.

4.6. Variability Measurement

4.6.1. Difference Imaging Analysis

Difference Image Analysis (DIA) uses the decorrelated Alard & Lupton image differencing algorithm (D. J. Reiss & R. H. Lupton 2016). We detected both positive and negative DIASources at 5σ in the difference image. Sources with footprints containing both positive and negative peaks due to offsets from the template position or blending were fit with a dipole centroid code, which simultaneously fits offset positive and negative PSFs. We filter the resulting DIASource catalog to remove detections with pixel flags indicative of artifacts, non-astrophysical trail lengths, or unphysically negative direct fluxes. Finally, we perform a simple spatial association of DIASources into DIAObjects using a one-arcsecond matching radius.

The Machine Learning reliability model applied to DP1 was developed with the aim to meet the latency requirements for Rubin Alert Production when executed on CPUs. Accordingly we developed a relatively simple model: a Convolutional Neural Network with three convolutional layers, and two fully connected layers. The convolutional layers have a 5×5 kernel size, with 16, 32, and 64 filters, respectively. A max-pooling layer of size 2 is applied at the end of each convolutional layer, followed by a dropout layer of 0.4 to reduce overfitting. The last fully connected layers have sizes of 32 and 1. The ReLU activation function is used for the convolutional layers and the first fully connected layer, while a sigmoid function is used for the output layer to provide a probabilistic interpretation. The cutouts are generated by extracting postage stamps of 51×51 pixels centered on the detected sources. The input data of the model consist of the template, science, and difference image stacked to have an array of shape (3, 51, 51). The model is implemented using PyTorch (J. Ansel et al. 2024). The Binary Cross Entropy loss function was used, along with the Adaptive Moment Estimation (Adam) optimizer with a fixed learning rate of 1×10^{-4} , weight decay of 3.6×10^{-2} , and a batch size of 128. The final model uses the weights that achieved the best precision/purity for the test set. Training was done on the SLAC Shared Scientific Data Facility (S3DF) with an NVIDIA model L40S GPU.

The model was initially trained using simulated data from the second DESC Data Challenge (DC2; (LSST Dark Energy Science Collaboration (LSST DESC) et al.

2021)) plus randomly located injections of PSFs to increase the number of real sources, for a total of 89,066 real sources. The same number of bogus sources were selected at random from non-injected DIASources. Once the LSSTComCam data were available, the model was fine-tuned on a subset of the data containing 183,046 sources with PSF injections. On the LSSTComCam test set, the model achieved an accuracy of 98.06%, purity of 97.87%, and completeness of 98.27%. As discussed in §5.8, the injections used to train this model version do not capture all types of astrophysical variability, so performance on the test set will not be representative for variable stars, comets, and other types of variable objects. The machine-learning reliability score, reported in the `reliability` column of the `DIASource` catalog, is a scalar value between 0 and 1 that quantifies the model’s confidence that a given detection is astrophysical.

4.6.2. Light Curves

To produce light curves, we perform multi-epoch forced photometry on both the direct visit images and the difference images. For light curves we recommend the forced photometry on the difference images (`psfDiffFlux` on the `ForcedSource` Table), as it isolates the variable component of the flux and avoids contamination from static sources. In contrast, forced photometry on direct images includes flux from nearby or blended static objects, and this contamination can vary with seeing. Centroids used in the multi-epoch forced photometry stage are taken either from object positions measured on the coadds or from the `DIAObjects` (the associated `DIASources` detected on difference images).

4.6.3. Solar System Processing

Solar system processing in DP1 consists of two key components: the association of observations (sources) with known solar system objects, and the discovery of previously unknown objects by linking sets of tracklets¹⁰³.

The association component begins by generating expected positions for all objects in the Minor Planet Center orbit catalog, using ephemerides computed with the `Sorcha` survey simulation toolkit (Merritt et al., in press)¹⁰⁴. To enable fast lookup of objects potentially present in an observed visit, we use the `mpsky` package (M. Juric 2025). In each image, the closest `DIASource` within 1 arcsecond of a known solar system object’s predicted position is associated to that object.

In DP1 we used a simple positional association to tag `DIASources` that are likely observations of known asteroids. The 1 arcsecond radius is intentionally generous; we did not see evidence of mismatches at DP1 depth and volume. This radius will be tuned for future processing campaigns.

The discovery component of Solar System processing uses the `heliolinx` package¹⁰⁵, which provides tools for asteroid identification and linking (A. Heinze et al. 2023). The repository contains code for the following tasks:

- Tracklet creation with `make_tracklets`
- Multi-night tracklet linking with an algorithm
- Linkage post processing (orbit fitting, outlier rejection, and de-duplication) with `link_purify`

The inputs to the discovery processing comprised all sources detected in difference images, regardless of whether they were tagged in the association step. These inputs were produced by an early processing of LSST-ComCam commissioning data, some of which were later rejected during DP1 processing and therefore do not appear in the final DP1 data products.

About 10% of all commissioning visits targeted the near-ecliptic field `Rubin_SV_38_7`, chosen to facilitate asteroid discovery. `Rubin_SV_38_7` produced the vast majority of asteroid discoveries in DP1, as expected, but a few were found in off-ecliptic fields as well.

Tracklet creation with `make_tracklets` used an upper limit angular velocity of 1.5 deg/day, faster than any main belt asteroid and in the range of many Near-Earth Object (NEO) discoveries. While no formal minimum angular velocity was imposed, in practice it would be unlikely to detect objects moving slower than about 0.01 deg day⁻¹. To minimize false tracklets from fields observed multiple times per night, the minimum tracklet length was set to three detections, and a minimum on-sky motion of five arcseconds was required for a valid tracklet. To claim a discovery candidate, we required tracklets to be linked across at least three nights.

Multi-night tracklet linking is the heart of Solar system discovery, which connects (“links”) tracklets belonging to the same object over a series of nights. It employs the `HelioLinC3D` algorithm (S. Eggl et al. 2020; A. Heinze et al. 2022), a refinement of the original `HelioLinC` algorithm of M. J. Holman et al. (2018). Each processing run tested each tracklet with 324 different hypotheses spanning heliocentric distances from 1.5 to

¹⁰³ A tracklet is defined as two or more detections of a moving object candidate taken in close succession in a single night.

¹⁰⁴ Available at <https://github.com/dirac-institute/sorcha>

¹⁰⁵ <https://github.com/heliolinx/heliolinx>

9.8 **astronomical unit (au)** and radial velocities spanning the full range of possible bound orbits (eccentricity 0.0 to nearly 1.0). The upper limit of 10 **au** was chosen because searches targeting more distant populations require different parameter choices. This range of distance encompasses all main belt asteroids and Jupiter Trojans, as well as many comets and Mars-crossers and some **NEOs**. A dedicated search for objects at heliocentric distances out to 50 **au** was also conducted; no distant objects were detected, consistent with expectations for the size of the **DP1** data set. Smaller heliocentric distances were not attempted here because nearby objects move rapidly across the sky and hence were not likely to remain long enough in an **LSSTComCam** field to be discovered.

Candidate linkages, defined as groups of tracklets whose propagated orbits cluster within a radius of 1.33×10^3 au at 1 au, are identified, then post-processed via `link_purify` to yield a final, non-overlapping set of high-confidence asteroid candidates, ranked by orbit-fit residuals and related metrics. While `heliolinx` can produce false-positive or redundant raw linkages by design, these are filtered during post-processing by `link_purify`, which applies a Rubin-specific, more stringent version of the MPC validation rules¹⁰⁶. This step both rejects spurious linkages and deduplicates multiple hypotheses for the same object, ensuring that only the highest-quality, non-redundant linkages are carried forward for orbit determination and for distinguishing new discoveries from rediscoveries of known objects.

5. PERFORMANCE CHARACTERIZATION AND KNOWN ISSUES

In this section, we provide an assessment of the **DP1** data quality and describe known issues.

5.1. Sensor Anomalies and ISR

In addition to the known detector features identified before **LSSTComCam** commissioning, most of which are handled by the ISR processing (see §4.2.1), we discovered a number of new types of anomalies in the **DP1** data. Since no corrections are currently available for these anomalies, they are masked and excluded from downstream data products.

5.1.1. Vampire Pixels

“Vampire” pixels are visible on the images as a bright defect surrounded by a region of depressed flux, as though the defect is stealing charge from its neighboring

pixels. **Figure 12** shows an example of a vampire pixel near the center of R22_S11 on an *r*-band flat.

From studies on evenly illuminated images, vampires appear to conserve charge. Unfortunately, no unique optimum way exists to redistribute this stolen flux so, following visual inspection, a defect mask was created to exclude them from processing. We have found some similar features on the ITL detectors on **LSSTCam**, and will use the same approach to exclude them.

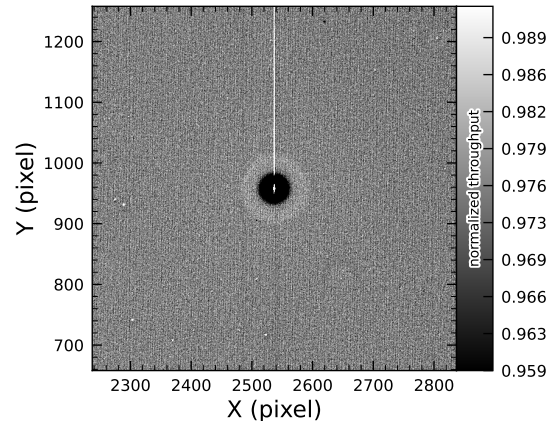


Figure 12. A large vampire pixel near the center of R22_S11, as seen on the *r*-band flat. This clearly shows the central hot “vampire” pixels, surrounded by a region of depressed signal, with a brighter ring surrounding that caused by the local electric field effects. The charge contained in the central pixels is incompletely shifted as the image is read, and that charge leaks out into subsequent rows as they are shifted through the remnant charge. The columns that contain the hot pixels are masked as defects in all processing, as this feature cannot be otherwise corrected.

5.1.2. Phosphorescence

Some regions of the **LSSTComCam** CCD raft were seen to contain large numbers of bright defects. An example is shown in **Figure 13** in a *g*-band flat. On further investigation, it appears that on some detectors a layer of photoresist wax was incompletely removed from the detector surface during production. As this wax is now trapped below the surface coatings, there is no way to physically clean these surfaces. If this wax responded to all wavelengths equally, then it would likely result in quantum efficiency dips, which might be removable during flat correction. However, it appears that this wax is slightly phosphorescent, with a decay time on the order of minutes, resulting in the brightness of these defects being dependent on the illumination of prior exposures. The worst of these regions were excluded with manual masks.

¹⁰⁶ <https://minorplanetcenter.net/mpcops/documentation/identifications/additional/>

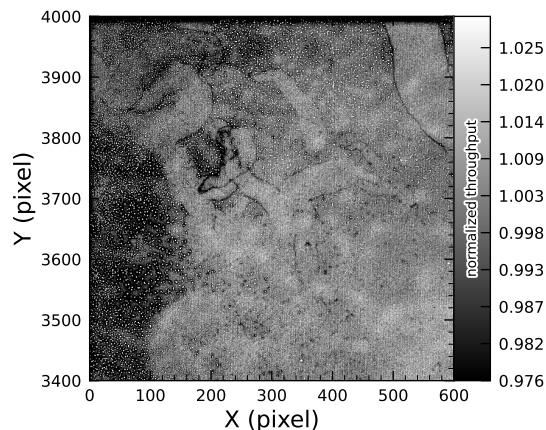


Figure 13. The top left corner of R22_S01 in the g-band flat, showing the many small defect features that are caused by the remnant photoresist wax. A single large defect box masks this region from further analysis to prevent these features from contaminating measurements.

5.1.3. Crosstalk

Crosstalk refers to unwanted signal interference between adjacent pixels or amplifiers. We use an average inter-amp crosstalk correction based on laboratory measurements with LSSTCam. These average corrections proved satisfactory, and so have been used as-is for DP1 processing. There are, however, some residual crosstalk features present post-correction, with a tendency towards over-subtraction. Figure 14 shows an example of a bright star with over-subtracted crosstalk residuals visible on neighboring amplifiers to both sides on exposure 2024120600239, detector R22_S02.

5.1.4. Bleed Trails

Bleed trails are produced when charge from saturated pixels spills into adjacent pixels. Bleed trails were anticipated on LSSTComCam sensors, but they appear in more dramatic forms than had been expected. As a bleed trail nears the serial register, it fans out into a “trumpet” shaped feature. Although bright, these features do not have consistently saturated pixels. In DP1 these “edge bleeds” were identified and masked.

Saturated sources can create a second type of bleed, where the central bleed drops below the background level. The depressed columns along these trails extend across the entire readout column of the detector, crossing the detector mid-line. We developed a model for these to identify which sources are sufficiently saturated to result in such a trail, which is then masked. As this kind of trail appears only on the ITL detectors, we’ve named these features “ITL dips”. Figure 15 shows an example of a bright star exhibiting the “ITL dip” phe-

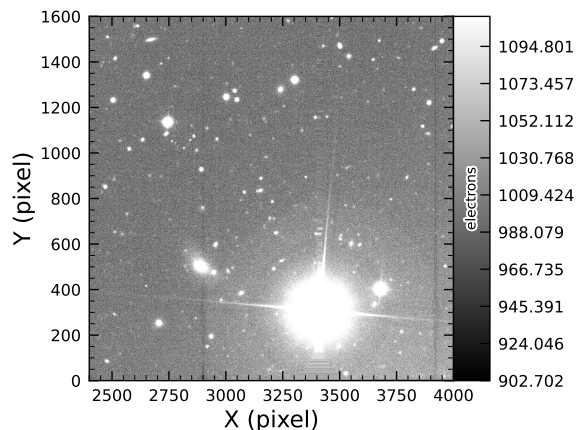


Figure 14. An example of a bright star with over-subtracted crosstalk residuals visible on neighboring amplifiers to both sides (exposure 2024120600239, detector R22_S02). The horizontal banding stretching from the center of the star shows the interpolation pattern covering the saturated core and the ITL edge bleed near the serial register.

nomenon on exposure: 2024121000503, detector: R22_S21.

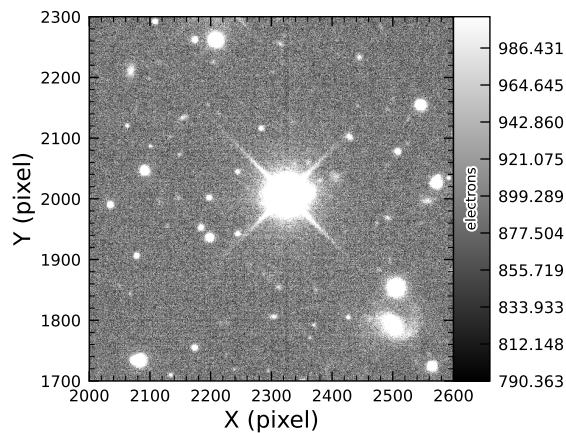


Figure 15. A bright star showing the “ITL dip” phenomenon, in which a dark trail extends out from the star to the top and bottom edges of the detector (exposure: 2024121000503, detector: R22_S21).

5.2. PSF Models

To characterize PSF performance, we use adaptive second moments (G. M. Bernstein & M. Jarvis 2002) measured on PSF stars and on the PSF model using the HSM implementation (C. Hirata & U. Seljak 2003; R. Mandelbaum et al. 2005). All measurements are expressed in the pixel coordinate frame of each detector. We characterize the performance of the PSF using the

classical trace of the second moment matrix T , along with the ellipticity parameters e^1 and e^2 . Measurements on the observed PSF stars are denoted as T_{PSF} , e_{PSF}^1 , e_{PSF}^2 , while those from PSF models are denoted as T_{model} , e_{model}^1 , e_{model}^2 . We compare two PSF modeling approaches:

- Piff with second-order polynomial interpolation (Piff O2), the pipeline’s default, and
- Piff with fourth-order polynomial interpolation (Piff O4), which serves as the final DP1 PSF model.

Table 5 summarizes each model’s ability to reconstruct the mean T , e^1 , and e^2 on LSSTComCam. Both models exhibit a negative residual bias in the reconstructed PSF size, with Piff O4 providing improved performance over Piff O2.

An alternative approach to evaluating the performance of the PSF model is to examine the average $\delta T/T$, where δT is $T_{\text{PSF}} - T_{\text{model}}$, across visits, projected onto focal-plane coordinates, as shown in Figure 16. Piff reveals strong spatial correlations in the residuals, including a systematic offset consistent with the results presented in Table 5. The presence of these spatial structures motivated the adoption of fourth-order polynomial interpolation in all bands except u -band. Although not shown in Figure 16, residual patterns persist even with third-order interpolation, indicating that it is insufficient to capture the complexity of the PSF variation. Increasing the interpolation order to five would nominally reduce the residuals further, but the limited number of stars available on some CCDs would not provide adequate constraints for such a model, while the resulting improvement would likely be minimal. Preliminary analysis of LSSTCam data in the laboratory at SLAC National Accelerator Laboratory (SLAC) shows that the ITL sensors exhibit the same pattern as ITL sensors on LSSTComCam.

Another way to look at the PSF modeling quality is via whisker plots of the PSF second and fourth moments and their modeling residuals projected on a part of the sky. In addition to the second moment, the spin-2 fourth moments, $e^{(4)}$, are defined as:

$$e_1^{(4)} = M_{40} - M_{04}$$

$$e_2^{(4)} = 2(M_{31} - M_{13}),$$

where M_{pq} are the standardized higher moments as defined in T. Zhang et al. (2023) measured on stars and PSF models. Figure 17 shows the whisker plots of e , $e^{(4)}$ (top rows), and δe , $\delta e^{(4)}$ in the ECDFS field. The direction of a whisker represents the orientation of the

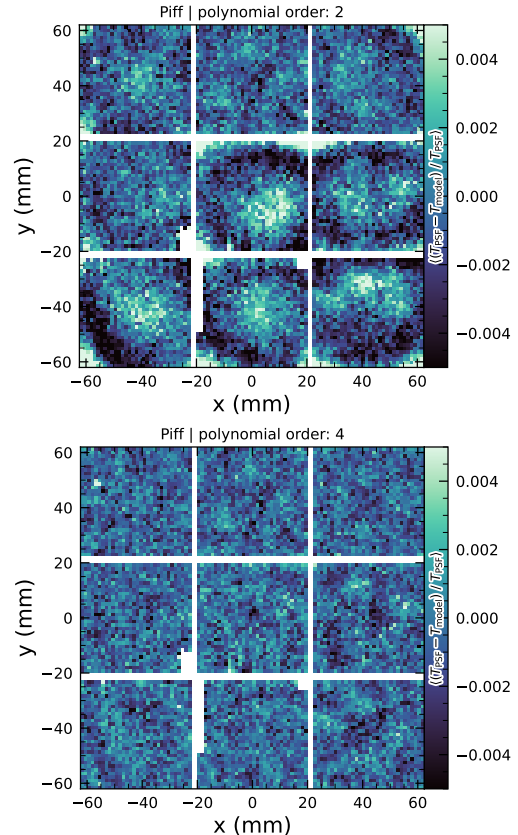


Figure 16. Average across all visits of $\delta T/T$ for Piff O2 and Piff O4 modeling on LSSTComCam. Averages are computed using a 120×120 binning.

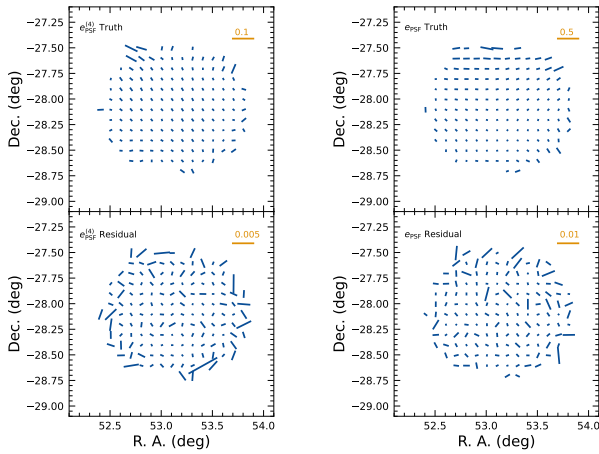
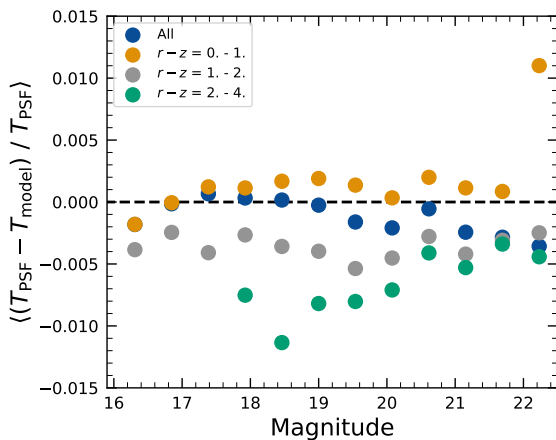
shape, while the length represents the amplitude $|e|$ or $|e^{(4)}|$. We observe coherent patterns in both the PSF moments and the residuals, the latter of which warrants further investigation if it persists in future data releases.

Figure 18 shows a plot of $\delta T/T$ versus stellar magnitude, which can reveal any dependencies between PSF size and flux. We also repeat this analysis in color bins to probe chromatic effects, as was also seen in DES (M. Jarvis et al. 2021). The residual is consistent with Table 5 and its cause is unknown. DP1 does not include the color correction implemented in the DES Year 6 analysis, T. Schutt et al. (2025). This will be included in processing of future data releases.

As noted in Rubin Observatory Science Pipelines Developers (2025), two key Piff features were not used in the DP1 processing. PSF color dependence was not implemented, and, while Rubin software allows Piff to work with sky coordinates (including WCS transformations), it does not yet correct for sensor-induced astrometric

Table 5. Observed mean values and comparison of model residuals, across all visits and filters

Quantity	Observed	Piff O2	Piff O4
		$\times 10^{-4}$	$\times 10^{-4}$
$\langle T \rangle$ (pixel ²)	11.366 ± 0.003		
$\langle e^1 \rangle$	$(-6.07 \pm 0.05) \times 10^{-3}$		
$\langle e^2 \rangle$	$(-4.57 \pm 0.05) \times 10^{-3}$		
$\langle e \rangle$	$(8.794 \pm 0.004) \times 10^{-2}$		
$\langle \delta T/T \rangle$		-4.0 ± 0.2	-5.0 ± 0.2
$\langle \delta e^1 \rangle$		0.6 ± 0.1	0.5 ± 0.1
$\langle \delta e^2 \rangle$		0.0 ± 0.1	0.0 ± 0.1

**Figure 17.** Whisker plots for the ECDFS field for e , $e^{(4)}$ and δe , $\delta e^{(4)}$.**Figure 18.** Binned $\delta T/T$ as a function of magnitude across all visits and filters and in bins of stellar colors.

distortions such as tree rings (H. Y. Park et al. 2017). Both features are planned for upcoming releases.

5.3. Astrometry

To characterize astrometric performance, we evaluate both internal consistency and agreement with an external reference. The primary measure of internal consistency is the repeatability of position measurements for the same object, defined as the RMS of the astrometric distance distribution for stellar pairs having a specified separation in arcminutes. We associate isolated point sources across visits and compute the rms of their fitted positions, rejecting any stars with another star within $2''$. Figure 19 shows the mean per-tract rms astrometric error in RA for all isolated point sources, both after the initial calibration and after the final calibration, which includes proper motion corrections. The results indicate that the astrometric solution is already very good after the initial calibration. Global calibration yields only modest improvement, likely due to the short time span of DP1 and the minimal distortions in the LSSTCom-Cam. In the main survey, the longer time baseline and greater distortions near the LSSTCam field edges will make global calibration more impactful. An additional measure of internal consistency is the repeatability of separations between objects at a given distance. To compute this, we identify pairs of objects that are separated by a specified distance and measure their precise separation during each visit in which both objects are observed. The scatter in these separation measurements provides an indication of the internal consistency of the astrometric model. Figure 20 shows the median separation for pairs of objects separated by approximately 5 arcminutes (referred to as “AM1”), computed per tract after the final calibration. These values are already approaching the design requirement of 10 mas.

To assess external consistency, we consider the median separation between sources not included in the astrometric fit and associated objects from a reference catalog (§3.3.3). For this, we use the Gaia DR3 catalog, with the

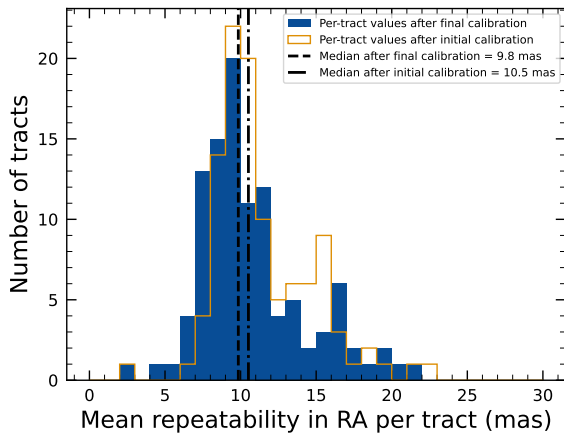


Figure 19. Mean per-tract astrometric repeatability of measurements of isolated point sources in RA in visits across all bands.

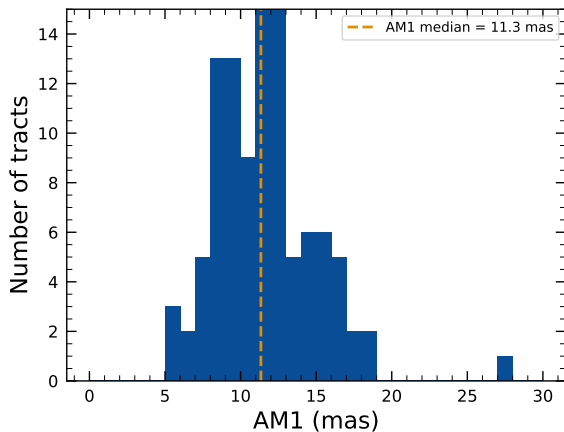


Figure 20. Median per-tract repeatability in separations between isolated point sources 5 arcmin apart (AM1) in visits across all bands.

object positions shifted to the observation epoch using the Gaia proper motion parameters. Figure 21 shows the median separation for each visit in the r -band in *tract* 4849 in the ECDFS fields. The calculated values are almost all within 5 mas, well below the design requirement of 50 mas for the main survey. By examining the astrometric residuals, we can assess whether there are distortions not accounted for by the astrometric model. In some cases, residuals from a single visit exhibit behavior consistent with atmospheric turbulence, as shown in Figure 22, which is characterized by a curl-free gradient field in the two-point correlation function of the residuals (E-mode), P. F. Léget et al. (2021) and W. F. Fortino et al. (2021). However, as seen in Figure 23, the residuals in many visits also have correlation functions with

a non-negligible divergence-free B-mode, indicating that some of the remaining residuals are due to unmodeled instrumental effects, such as rotations between visits.

We can see unmodeled camera distortions by stacking the astrometric residuals over many visits as a function of the focal plane position. Figure 24 shows the median residuals in x and y directions for 1792 visits. Spatial structures are evident at the CCD level, as well as at the mid-line break, the discontinuity between the two rows of amplifiers, in the y -direction residuals. Further stacking all the detectors makes certain effects particularly clear. Figure 25 shows distortions very similar to those measured for an LSSTCam ITL sensor in a laboratory setting in J. H. Esteves et al. (2023).

5.4. Differential Chromatic Refraction

DCR occurs when light passes through Earth’s atmosphere, refracting more for shorter wavelengths, which causes blue light to appear shifted closer to the zenith. This wavelength-dependent effect results in the smearing of point sources along the zenith direction, specifically parallel to the parallactic angle. The DCR effect is observable in LSSTComCam data, particularly in the angular offset versus $g - i$ band magnitude difference plots, as shown in Figure 26. These plots include 228 visits selected to maximize the range of observed airmass, which spans 1.01–1.30 with a mean value of 1.13. When looking at data perpendicular to the parallactic angle, sources exhibit no discernible DCR effect, which is expected, and form a clear vertical distribution on the two-dimensional density plots in Figure 26.

In contrast, sources aligned with the parallactic angle exhibit a tilted, linear distribution, clearly demonstrating that the relationship between angular offset and the $g - i$ band magnitude difference, thereby providing a visual indication of the DCR effect. The DCR effect will be addressed in future releases.

5.5. Stellar Photometry

The photometric repeatability for isolated bright unresolved sources following the FGCM fits was excellent. For the 10% of unresolved sources withheld from the fit and having signal-to-noise ratios greater than 100, the photometric repeatability after applying chromatic correction was 7.1, 5.4, 5.4, 5.1, 5.9, and 6.5 mmag in the *ugrizy* bands respectively, across all fields. After accounting for photometric noise, the intrinsic photometric repeatability was approximately 4.8, 2.7, 1.7, 1.0, 2.0, and 1.1 mmag in *ugrizy*. The DP1 processing does not yet include chromatic corrections in the final photometry. In this case the delivered photometric repeatability was 3–8 mmag for *grizy*.

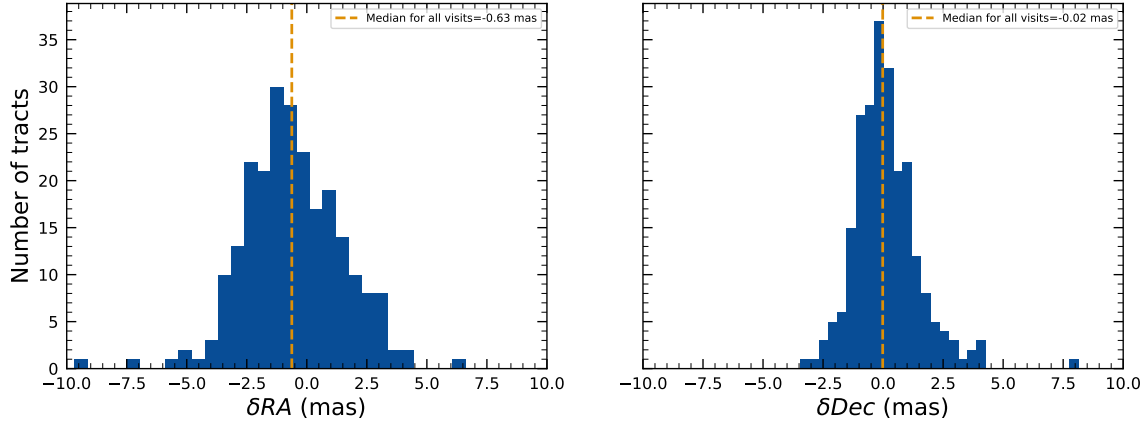


Figure 21. Median absolute offset for all visits in r -band in [tract 4849](#) in the ECDFS field. The offset is the difference between the positions of isolated point sources that were reserved from the astrometric fit and matched objects from the Gaia DR3 catalog.

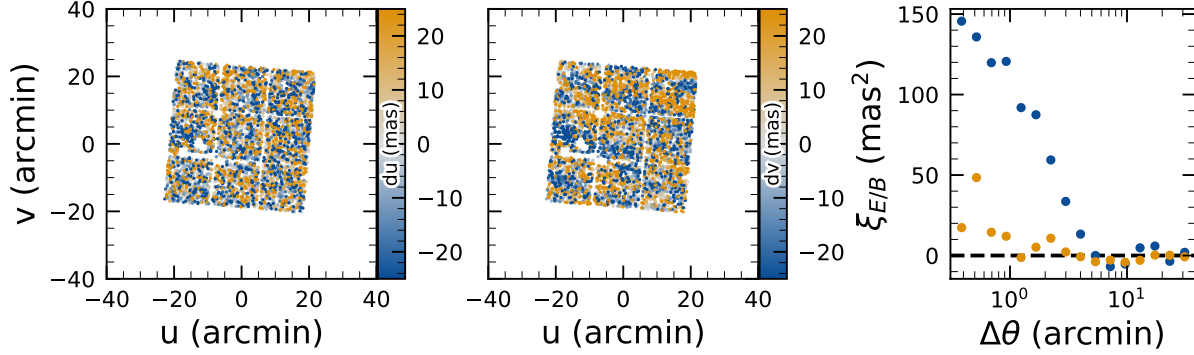


Figure 22. Astrometric residuals in u (left panel) and v (center panel) directions with the E (blue) and B (orange) modes of the two-point correlation function (right panel) seen in visit 2024120200359 in [tract 2393](#) in u band. The residuals show a wave-like pattern characteristic of atmospheric turbulence, and there is significant E-mode and negligible B-mode in the correlation function.

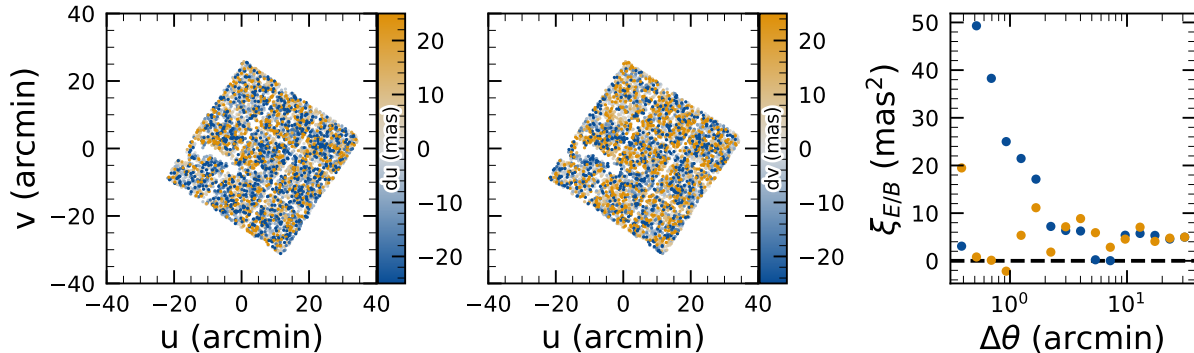


Figure 23. Astrometric residuals in u (left panel) and v (center panel) directions, with the E (blue) and B (orange) modes of the two-point correlation function (right panel) seen in visit 2024120700527 in [tract 2393](#) in u band. There are coherent residuals, but without the wave-like pattern seen in [Figure 22](#), and the correlation function has significant values for both E and B-modes.

In [Figure 27](#), we show the stellar loci for $ugriz$ for unresolved sources in the `DP1 Object` table (§3.2). These

unresolved sources were selected using the extendedness

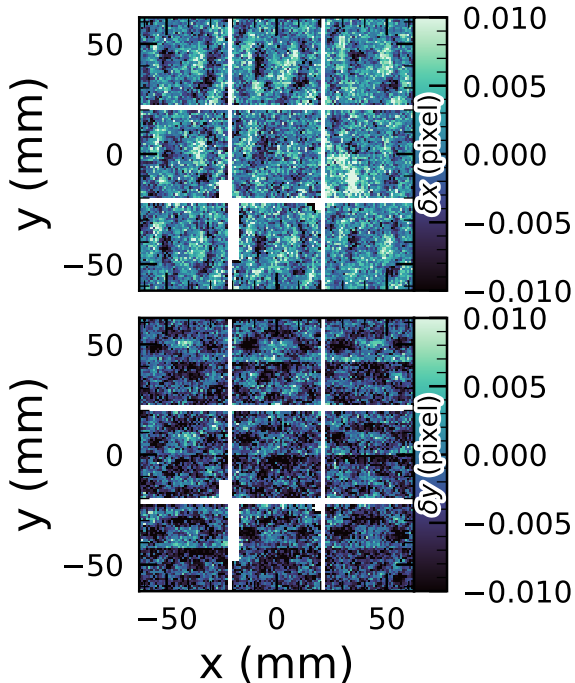


Figure 24. Median astrometric residuals as a function of focal plane position, shown in the left panel for the x direction and in the right panel for the y direction, for all nine LSSTComCam CCDs independently. The range of the color scale is ± 0.01 pixels, corresponding to 2 mas, showing that the effect is small.

parameter (§3.2) in the `Object` catalog. This parameter is assigned a value of 0 (unresolved) or 1 (resolved) in each band based on the difference between the PSF and CModel magnitudes. The extendedness is set to 1 when this magnitude difference exceeds 0.016 mag, as the PSF flux for extended sources is biased low relative to the CModel flux. This method has been previously employed by the SDSS pipelines, and its statistical properties, including the optimal combination of information from different bands and repeated measurements, are discussed in C. T. Slater et al. (2020).

Figure 28 illustrates the behavior of the extendedness parameter. Its behavior in the g and r bands is similar, with unresolved sources scattered around the vertical line centered on zero. The width of the distribution increases towards fainter magnitudes. Resolved sources are found to the right and the dashed lines in the top panels show the adopted “star-galaxy” separation boundary. The morphology of the two color-magnitude diagrams in the bottom panels suggest that the unresolved sample suffers from increasing contamination by galaxies for $r > 24$. This behavior is consistent with

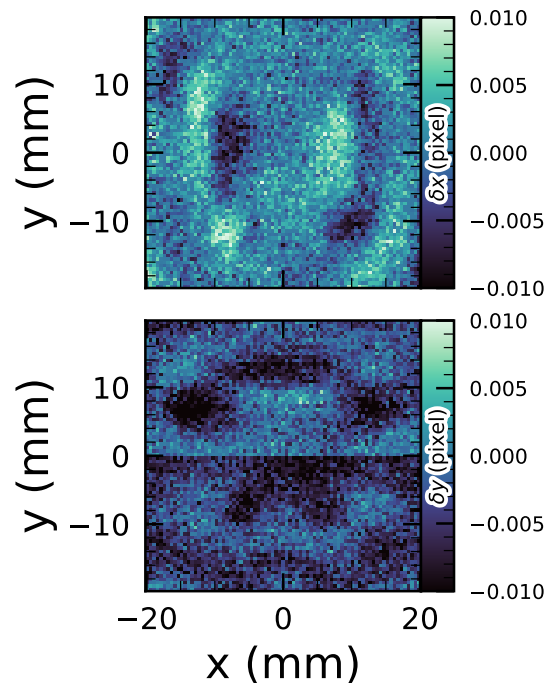


Figure 25. Median residuals as a function of pixel position, shown in the left panel for the x direction and in the right panel for the y direction. These residuals are aggregated across all nine CCDs that comprise the central LSSTComCam raft. The range of the color scale is ± 0.01 pixels, corresponding to 2 mas, showing that the effect is small.

simulation-based predictions from C. T. Slater et al. (2020).

5.6. Detection Completeness on Coadds

We characterize completeness by injecting synthetic sources into coadded images, and by comparing source detections to external catalogs. In both cases, we use a greedy, probabilistic matching algorithm that matches reference objects, in order of descending brightness, to the most likely target within a $0''.5$ radius.

We inject sources in 12 of the patches of the ECDFS region with the deepest coverage. The input catalog contains stars and galaxies from part of the Data Challenge 2 (DC2) simulations (LSST Dark Energy Science Collaboration (LSST DESC) et al. 2021), where the galaxies consist of an exponential disk and de Vaucouleurs (G. de Vaucouleurs 1948, 1953) bulge. To avoid deblender failures from excessive increases in object density, stars with a total flux (i.e., summed across all six bands) brighter than 17.5 mag are excluded, as are galaxies whose total flux is brighter than 15 mag or fainter than 26.5 mag. Half of the remaining objects are selected for injection. Afterwards, individual bulge and disk com-

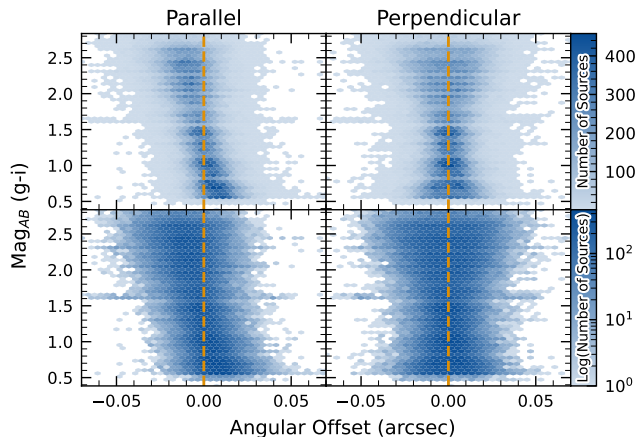


Figure 26. Visualization of [Differential Chromatic Refraction \(DCR\)](#) observed in the [LSSTComCam](#) commissioning campaign. The $g - i$ color is computed for every source in the reference catalog (§3.3.3) that is matched to a direct source in the science image, and the binned density for the full survey is plotted against the angular offset between the reference and detected positions. The angular offset is projected along coordinates parallel and perpendicular to the parallactic angle of the observation, and shows a characteristic correlation along the parallel axis with no correlation along the perpendicular axis. The orange vertical dashed line indicates the expected $g - i$ magnitude distribution at zero angular offset.

ponents fainter than 29 mag are also excluded, both for computational expediency and because their structural properties are less likely to be representative of real galaxies.

Figure 29 shows completeness as a function of magnitude for these injected objects in the [ECDFS](#) field. These completeness estimates are comparable to results from matching external catalogs. Matching to the Hubble Legacy Field catalog ([G. Illingworth et al. 2016](#); [K. E. Whitaker et al. 2019](#)) reaches 50% completeness at $F775W = 26.13$, or about $i = 25.83$ from differences in matched object magnitudes. Similarly, completeness drops below 90% at $VIS = 23.80$ from matching to [Euclid Q1](#) ([Euclid Collaboration et al. 2025](#)) objects, equivalent to roughly $i = 23.5$. The [Euclid](#) imaging is of comparable or shallower depth, so magnitude limits at lower completeness percentages than 90% are unreliable, whereas the [HST](#) images cover too small and irregular of an area to accurately characterize 80-90% completeness limits.

At the 80% completeness limit, nearly 20% of objects, primarily injected galaxies, are incorrectly classified as stars based on their reference band extendedness. Similarly, the fraction of correctly classified injected stars

drops to about 50% at $i = 23.8$ (corresponding to 90% completeness).

This analysis has several caveats. The selection of objects for matching in any catalog is not trivial. Some fraction of the detections are spurious, particularly close to bright stars and their diffraction spikes. Additionally, some objects lie in masked regions of one survey but not another, which has not been accounted for. For injected source matching, the reference catalog (§3.3.3) does not include real on-sky objects. Based on prior analyses of the [DC2](#) simulations, purity is generally greater than completeness at any given magnitude. Similarly, for bright ($i < 23$) objects classified as stars by reference band extendedness, < 5% are either unmatched to a [Euclid](#) or [HST](#) object, or misclassified - that is, selecting on extendedness alone yields a fairly pure but incomplete sample of stars. We expect to remedy some of these shortcomings in future releases.

5.7. Model Flux and Shape Measurement

Figure 30 shows i -band magnitude residuals for [CModel](#) and [Sérsic](#) measurements using the matched injected galaxies described in §5.6. Similar behavior is seen in other bands. [Sérsic](#) fluxes show reduced scatter for galaxies with $i < 22.5$, though [CModel](#) fluxes are less biased, with median residuals closer to zero and less magnitude-dependent. For fainter objects, [Sérsic](#) fluxes are more biased and less accurate. The magnitude of this bias is considerably larger than previously seen in simulated data. Subsequent testing indicates that this bias can be (roughly) halved by fitting an exponential model first, and then using those parameters to initialize a free [Sérsic](#) fit. This approach will be adopted in future releases. Aperture fluxes - including [Kron](#) and [GAaP](#) - are not shown as they are not corrected to yield total fluxes. The correction for [Kron](#) fluxes can be derived from the [Sérsic](#) index ([A. W. Graham & S. P. Driver 2005](#)), but this correction is not provided in object tables.

Figure 31 shows $g - i$ color residuals versus r -band magnitude for the same sample of galaxies as Figure 30. For this and most other colors, [GAaP](#) (with a $1''$ aperture) and [Sérsic](#) colors both yield lower scatter; however, the [CModel](#) colors have the smallest bias. Curiously, the [GAaP](#) bias appears to be magnitude-dependent, whereas the [Sérsic](#) bias remains stable from $19 < r < 26$. Any of these color measurements are suitable for use for deriving quantities like photometric redshifts, stellar population parameters, etc.

In addition to photometry, some algorithms include measurements of structural parameters like size, ellipticity, and [Sérsic](#) index. One particular known issue is

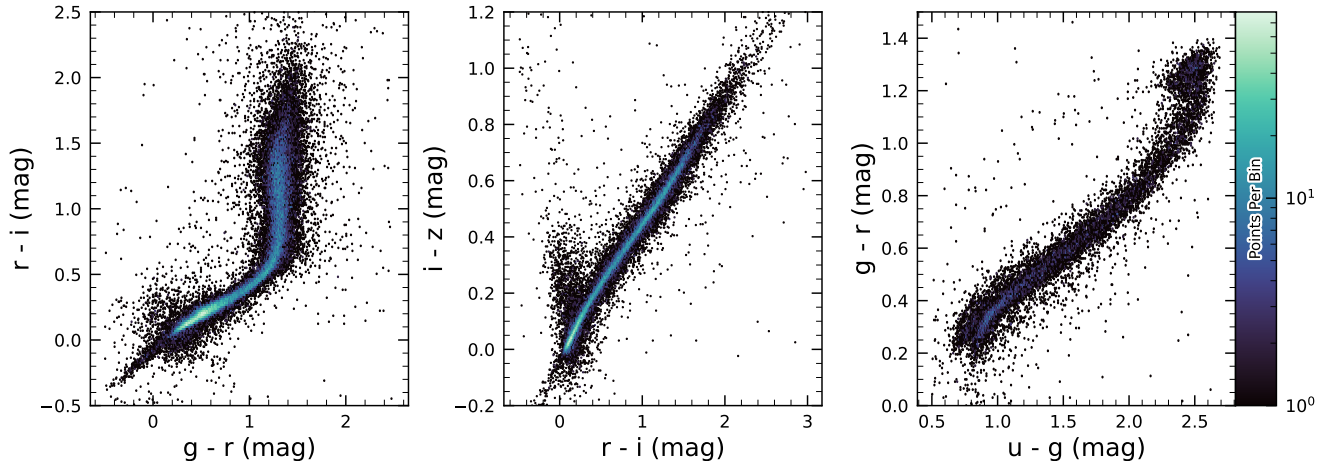


Figure 27. Examples of stellar loci for unresolved sources from the DP1 dataset. From left to right: *gri* stellar locus containing 63,236 stars with signal-to-noise ratio > 200 in the *i* band; *riz* stellar locus containing 46,760 stars with signal-to-noise ratio > 200 in the *i* band; *ugr* stellar locus containing 12,779 stars with signal-to-noise ratio > 50 in the *u* band.

that many (truly) faint objects have significantly overestimated sizes and fluxes. This was also seen in the Dark Energy Survey (K. Bechtol et al. 2025), who dubbed such objects “super-spreaders”. These super-spreaders contribute significantly to overestimated fluxes at the faint end (see e.g. Figure 30), and are particularly problematic for the Kron algorithm (R. G. Kron 1980), which should only be used with caution.

As mentioned in §4.5, the Sérsic fits include a free centroid, which is initialized from the fiducial centroid of the object. Preliminary analyses of matched injected objects suggest that the Sérsic model galaxy *astrometry* residuals are somewhat smaller than for the standard centroids used in other measurements, and so users of the Sérsic photometry should also use these centroid values. One caveat is that for faint objects and/or in crowded regions with unreliable deblending, free centroids can drift significantly and potentially towards other objects, so objects with large differences between the fiducial and Sérsic *astrometry* should be discarded or used with caution.

Sérsic model parameter uncertainties are estimated by computing and inverting the Hessian matrix with the best-fit parameter values, after replacing the pixel data (but not uncertainties) by the best-fit model values. Currently, only the on-diagonal dispersion term (square root of the variance) is provided as an error estimate for each parameter. Future releases may provide more off-diagonal terms of the covariance matrix - particularly for the structural parameters, which are known to be correlated.

A major outstanding issue is that many parameter uncertainties - including but not limited to those for

fluxes - are underestimated. This is at least partly (but not wholly) due to the fact that coaddition introduces covariance between pixels, which is not captured in per-pixel variances.

The degree to which uncertainties are underestimated can depend on the parameter in question and on the brightness of the object. In plots of uncertainty-scaled residuals, the ideal behavior is for the median (i.e. the bias) to lie close to zero, and for the $\pm 1\sigma$ lines to lie at ± 1 , without any dependence on magnitude. Figure 32 shows that flux and color uncertainties for PSF model magnitudes of injected stars are both underestimated, but by a factor of approximately 1.7–2 that is not very sensitive to SNR. This holds for astrometric/centroid parameters as well.

In turn, Figure 33 shows that CModel color uncertainties of galaxies are underestimated by a similar factor at the faint end, but with appreciable scaling with magnitude (and thereby SNR). Flux error underestimation is both larger than for colors and scales more strongly with SNR. This indicates that systematic effects dominate the errors in fluxes, particularly for bright galaxies. This is also at least partly but not wholly due to so-called model inadequacy - that is, the fact that galaxy models, parametric or otherwise, are insufficiently complex to capture the structure of real galaxies.

Figure 34 shows that Sérsic model fluxes and colors have similar behavior as CModel, but with a greater degree of overestimation. This may be partly due to the fact that Sérsic parameter uncertainties are estimated along with the free centroid and structural (shape and Sérsic index) parameters, whereas the forced CModel

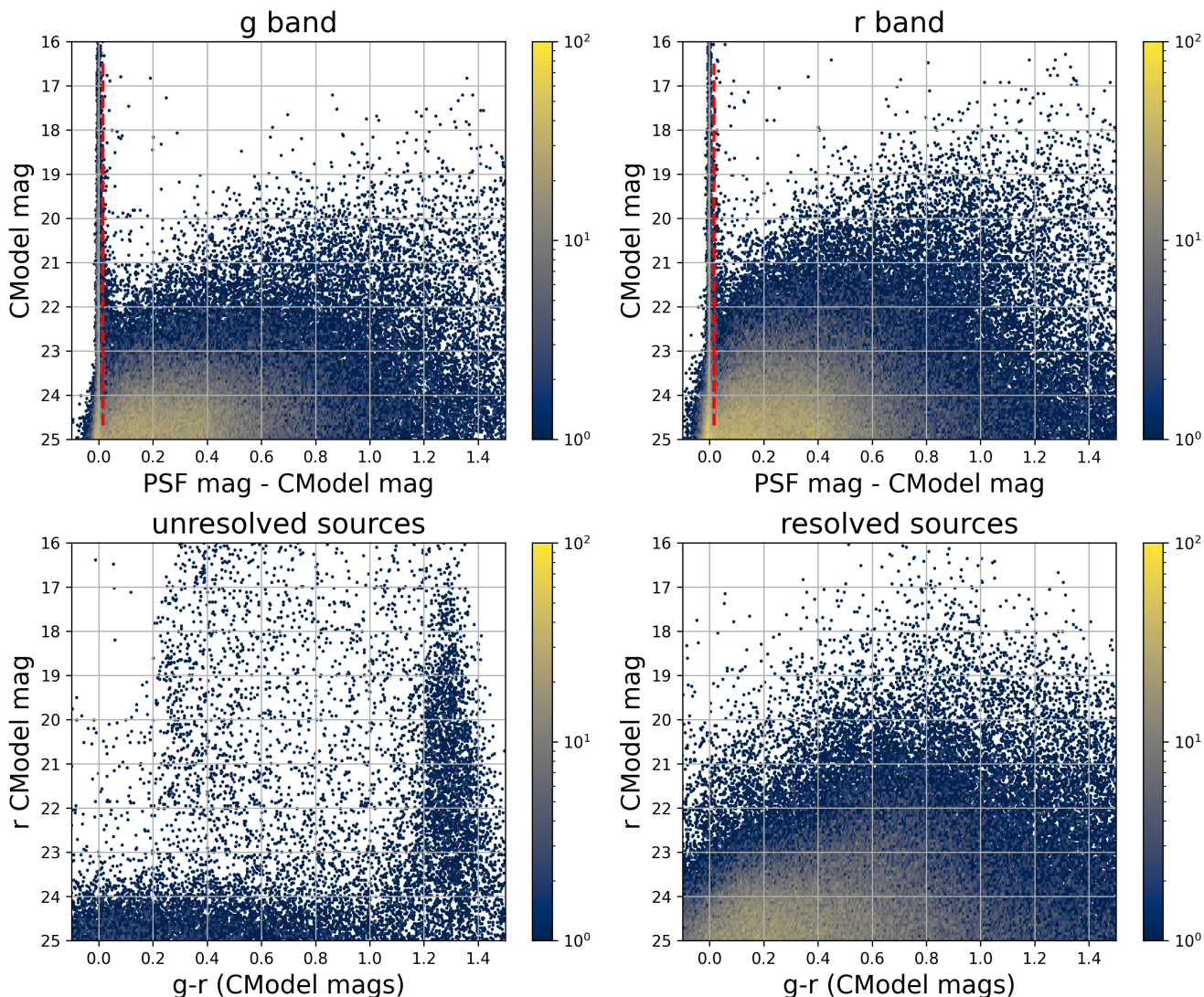


Figure 28. The top two panels show the difference between the PSF and CModel magnitudes as a function of CModel magnitude in the g and r bands for 178,547 sources with $CModel_r < 25$ from the ECDFS field. The vertical dashed line in each panel marks the minimum value (0.016 mag) for setting the extendedness parameter to 1. The bottom two panels show the r vs. $g - r$ color-magnitude diagrams for 14,701 unresolved (left) and 163,666 resolved (right) sources. Note the unresolved sample suffers from increasing contamination by galaxies for $r > 24$.

fluxes and errors are derived from linear flux fits with a fixed shape and centroid.

Efforts are underway to investigate and quantify the origin of uncertainty underestimates and future releases will, at the least, provide recommendations for mitigations.

5.8. Difference Imaging

We assessed the performance of image differencing using both human vetting (§5.8.1) and source injection (§5.8.2).

5.8.1. Difference Imaging Purity

Members of the DP1 team labeled more than 11,000 DIASource image triplets, each consisting of cutouts from the science, template, and difference images. An internal labeling service (`tasso`) was deployed within the USDF environment. A random subset of approximately 16,000 DIASources was selected and uploaded to the service, which remained active for roughly three months and labeled by members of the DP1 team. Users labeled DIASource PNG image triplets, each consisting of cutouts from the science, template, and difference images. Each stamp had dimensions of 51×51 pixels, matching the input size required by the machine-

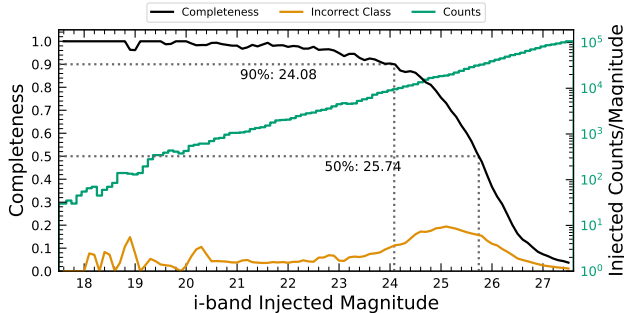


Figure 29. Completeness and incorrect classification fraction as a function of i -band CModel magnitude (Reference Magnitude) for DC2-based injected objects into a portion of the ECDFS field. The “Incorrect Class” line shows the proportion of objects that are matched but classified incorrectly by their reference-band extendedness, i.e. stars with extendedness of 1 or galaxies with extendedness of 0 in the reference band.

learning model. Access to the labeling service was granted to all individuals with commissioning data access. Each DIASource was classified exactly once, with a total of 35 volunteers contributing labels. Figure 35 show an example of one of the image triplets consisting of cutouts from the science, template, and difference images that volunteers were asked to label.

The labeled sources were classified into multiple categories representing real astrophysical events and artifacts. Prior to any filtering, the raw artifact-to-real ratio was approximately 9:1. Bright stars were identified as the dominant source of artifacts, while correlated noise, particularly in the u and g bands, also produced spurious detections near the flux threshold. We expect to be able to mitigate these effects in future LSSTCam data.

Applying a reliability threshold based on the Machine Learning reliability model described in §4.6.1 improved the purity of transient detections but had limited impact on variable stars. This limitation arises from technical constraints at the time of model training, which prevented the injection of variable stars into the synthetic training set. Future reliability models for LSST-Cam data, described in §4.6.1, will be trained using a broader and more representative range of input data.

The performance of the reliability model on the test data (§4.6.1) is shown in Figure 36. The rate of true positives and false negatives obtained by thresholding the reliability score at 0.5 is reported for transients (99 stamps), and variable stars (316 stamps) vetted in `tasso` in Table 6.

Additionally we crossmatched stamps with Solar System Objects with known orbits retrieving 5,988 Solar System Objects stamps.

Table 6. The rate of true positives (TP) and false negatives (FN) obtained by thresholding the reliability score at 0.5 for Solar system objects, transients and variable stars.

Object Type	Number	TP Rate	FN Rate
Solar System	5,988	93.5%	6.5%
Transients	99	73.7%	26.3%
Variables	316	3.5%	96.5%

5.8.2. Difference Imaging Detection Completeness

We assess the performance of our difference imaging pipeline using synthetic source injection on the science images prior to differencing. We construct a catalog of injected sources by joining two different samples of point sources, a set of hosted sources to emulate transients in galaxies and second set of hostless sources. The hosts are selected from the pipeline source catalog that is produced upstream by imposing a cut on their extendedness measurement and selecting $N_{\text{src}} = \min(100, N \times 0.05)$ of the N available sources per detector. For each host we pick a random position angle and radius using its light profile shape to decide where to place the source, and also a random value of brightness for the injected source, with magnitudes higher than the host source.

The hostless sources instead have random positions in the CCD focal plane, and magnitudes chosen from a random uniform distribution with $20 \geq m \geq m_{\text{lim}} + 1$, where m_{lim} is the limiting magnitude of the image. We used the LSST `source_injection` package¹⁰⁷ to include these sources in our test images. We performed a coordinate cross-match task, with a threshold of $0''.5$ to find which of these sources were detected and which were lost, enabling the calculation of a set of performance metrics.

In Figure 37 we show the detection completeness as a function of the SNR, for sources in the ECDFS field, for filters $griz$. We observe a completeness $> 95\%$ for sources with $\text{SNR} > 6$, with mean completeness $\simeq 99\%$ and standard deviation of $\simeq 0.7\%$. In Figure 38 we show the distribution of the residuals of the recovered sky coordinates for the detected synthetic sources. The marginal distributions are both centered at zero, and for sources of $\text{SNR} > 20$ the residuals are compatible with normal distributions $\mathcal{N}(\mu = 0, \sigma^2 = (0''.02)^2)$. In Figure 39 we show photometry results for our detected synthetic sources in the i filter, using PSF photometry

¹⁰⁷ <https://pipelines.lsst.io/modules/lsst.source.injection/index.html>

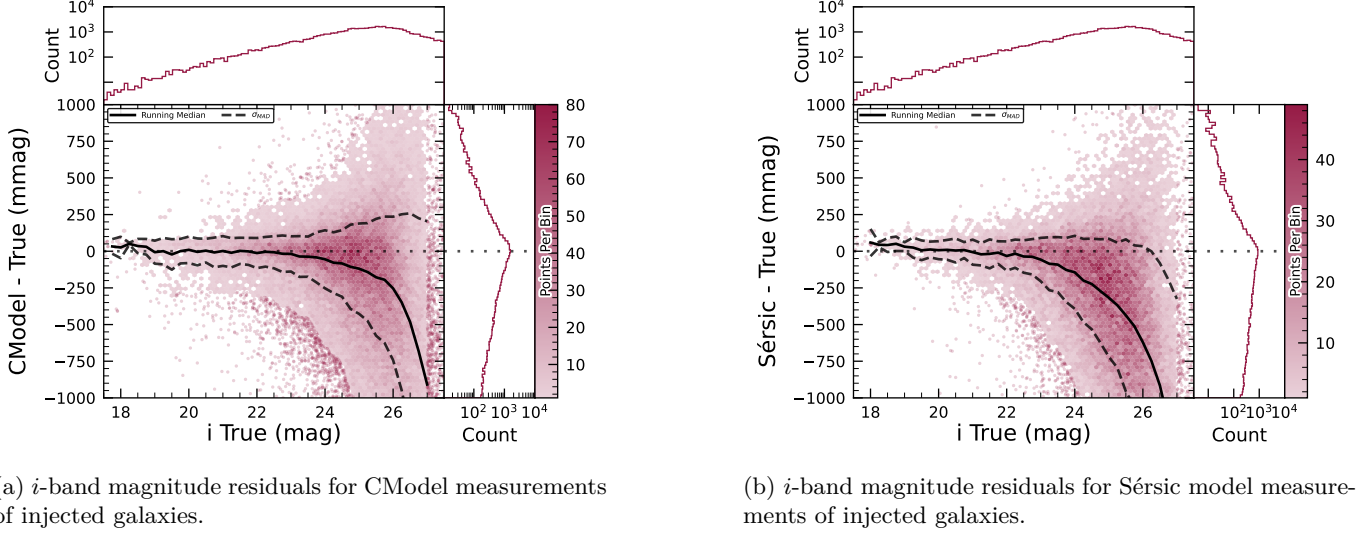


Figure 30. i -band magnitude residuals for matched injected DC2 galaxies with the CModel and Sérsic algorithms in a portion of the ECDFS region, including the median and scatter thereof. The black line is the median.

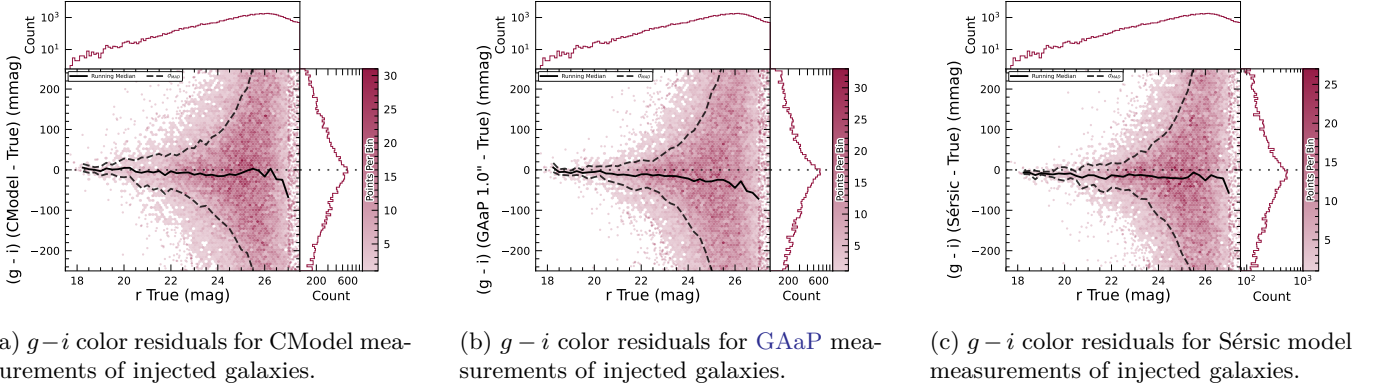


Figure 31. $g-i$ color residuals versus true r -band magnitude for matched injected DC2 galaxies with the CModel, GAaP and Sérsic algorithms in a portion of the ECDFS region.

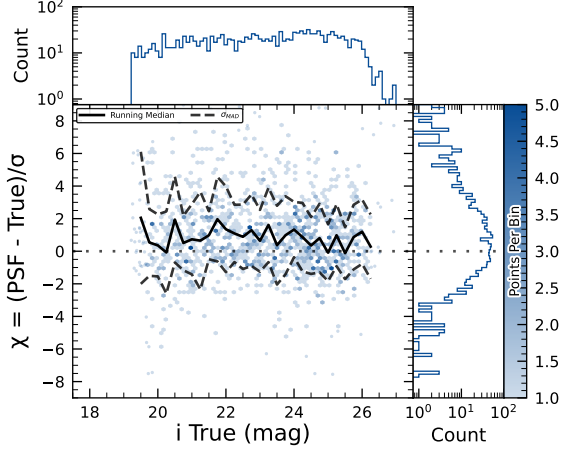
on the difference images. We include both the magnitude residuals as well as the flux pulls, defined as $(f_{PSF} - f_{True})/\sigma_{f_{PSF}}$, where f_{True} is the true flux, f_{PSF} is the PSF flux and $\sigma_{f_{PSF}}$ is its uncertainty, as a function of the true magnitude of the synthetic sources, including the running median and median absolute deviation (MAD) for the whole brightness range. We also include the true magnitude distribution as well as the detection completeness on the top panel, and for reference the 90% and 50% completeness magnitude values in vertical lines. On the right panels we include the marginal distribution for sources brighter than 22.5 mag, splitting the data into hosted and hostless, as well as the robust mean and standard deviation. From this figure we can see that our flux measurements are accurate within a wide range of magnitudes, for both hosted and hostless synthetic sources. We find that the median offset is below 0.002 mag for true magnitudes below 21, and with a

maximum σ_{MAD} scatter of about 0.02 mag in this range. For true $m_i < 22.5$, the robust running median PSF magnitudes residuals are < 0.02 mag, and when splitting into hosted and hostless both robust median are well below 0.01, and robust σ , i.e. σ_{MAD} are also well below 0.05. For all sources with $m_i < 21.5$ the running median is always $|\langle \delta \rangle| < 0.1$, and MAD $\sigma_\delta < 1$. Extending to sources with $m_i < 22.5$ then hostless sources have a robust mean pull below 0.02, with a robust standard deviation < 1.15 , while these parameters increase to 0.2 and 1.2 for hosted sources, suggesting that we might have contamination from host background sources potentially biasing our fluxes.

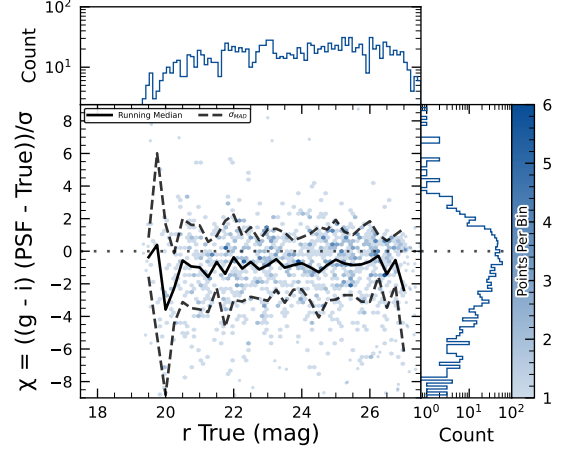
5.9. Solar System

5.9.1. Asteroid Linking Performance

The evaluation of asteroid linking performance in DP1 focused on demonstrating discovery capability. The so-

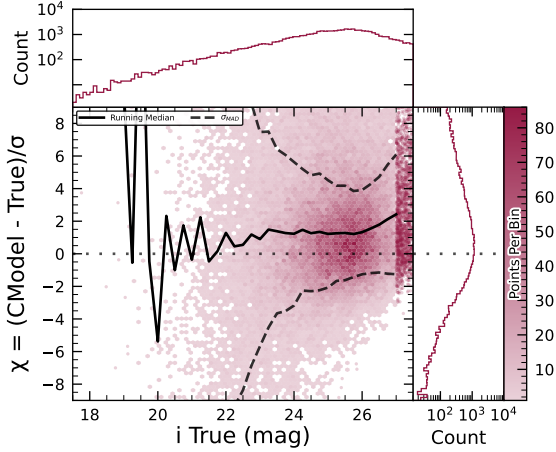


(a) i -band flux uncertainty-scaled residuals for PSF model measurements of injected stars.

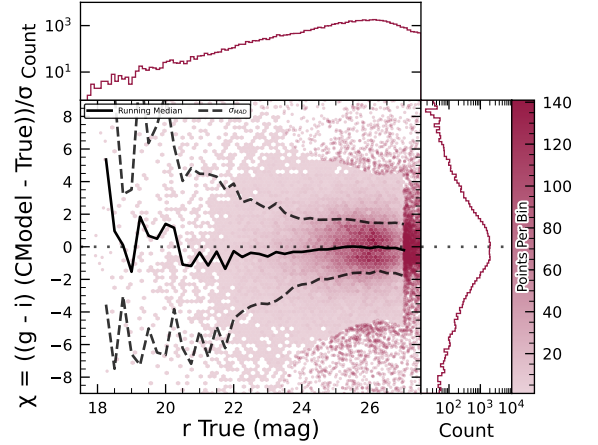


(b) $g - i$ color uncertainty-scaled residuals for PSF model measurements of injected stars.

Figure 32. Color and flux uncertainty-scaled residuals for matched injected DC2 stars' PSF model measurements in a portion of the ECDFS region.



(a) i -band flux uncertainty-scaled residuals for CModel measurements of injected galaxies.



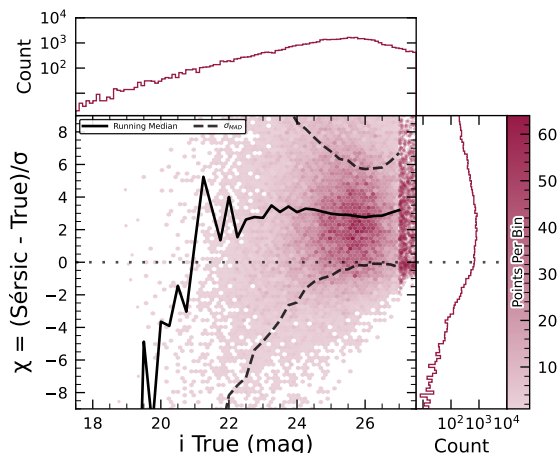
(b) $g - i$ color uncertainty-scaled residuals for CModel measurements of injected galaxies.

Figure 33. Color and flux uncertainty-scaled residuals for matched injected DC2 galaxies' CModel measurements in a portion of the ECDFS region.

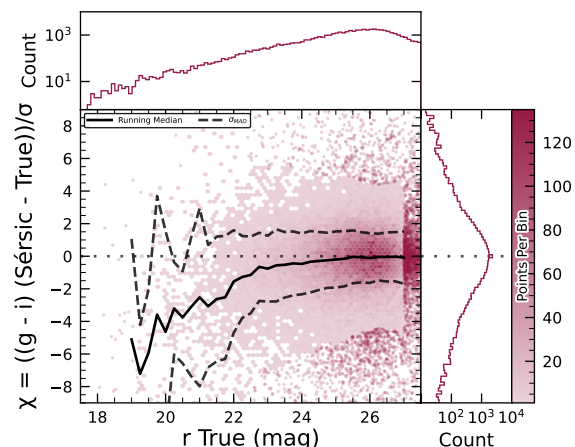
lar system discovery pipeline produced 269,581 tracklets, 5,691 linkages, and 281 post-processed candidates.

As described in §4.6.3, post-processing of the `heliolinc` output with `link_purify` produced a final set of 281 candidate linkages, ranked with the most promising first. We then used `find_orb` (B. Gray 2025) to derive orbit fits for each candidate, sorting the resulting list by χ_{dof}^2 , a measure of fit quality. A conservative manual investigation of these candidates yielded a curated list of 93 probable new asteroid discoveries. Manual inspection of the linkages indicated that those ranked 0–137 corresponded to unique real asteroids; ranks 138–200 contained additional real objects intermixed with some spurious linkages; and ranks higher than 200 were

essentially all spurious. This analysis indicates that it will be possible to identify cuts on quality metrics such as χ^2 to define discovery candidate samples with high purity; determining the exact quantitative cut values requires more data with `LSSTCam`. We next removed all observations matched to known asteroids (using `Minor Planet Center (MPC)`'s `MPCChecker` service), reducing the number of candidates to 97. Of these, four had strong astrometric and/or photometric outliers, likely due to self-subtraction in difference images due to the unavoidable limitations of template generation from the limited quantity of data available from `LSSTComCam`. We suspect these four linkages do correspond to real objects, but have chosen to discard them out of an abun-



(a) i -band flux uncertainty-scaled residuals for Sérsic model measurements of injected galaxies.



(b) $g-i$ color uncertainty-scaled residuals for Sérsic model measurements of injected galaxies.

Figure 34. Color and flux uncertainty-scaled residuals for matched injected DC2 galaxies' Sérsic measurements in a portion of the ECDFS region.

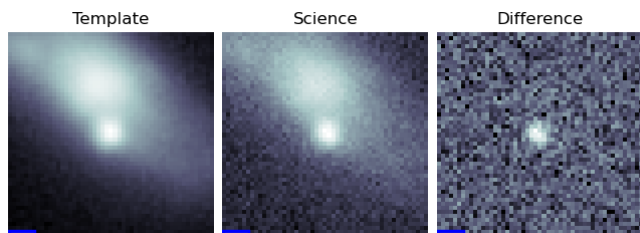


Figure 35. An example an image triplet consisting of cutouts showing, from left to right, the template, science, and difference images that volunteers were asked to label.

dance of caution. The remaining 93 were submitted to the Minor Planet Center and accepted as discoveries, demonstrating the LSST pipelines are able to successfully discover new solar system objects.

5.9.2. Asteroid Association Performance

During the Solar System association step, 5988 DiaSources were linked to 431 unique Solar System objects. These include 3,934 DiaSources with 338 previously known objects cataloged by the MPC, and 2,054 DiaSources with the 93 newly-discovered objects, all of which are main belt asteroids. An additional 143 detections of these newly discovered objects were also recovered. These detections were not initially identified by the discovery pipelines, as they did not meet the required criteria for tracklet formation, specifically the minimum number of detections and/or the maximum allowed time span between observations.

The astrometric residuals of known asteroid associations are shown in Figure 40. The astrometric precision for solar system sources is excellent, with the majority of objects detected within $0''.1$ of their expected positions.

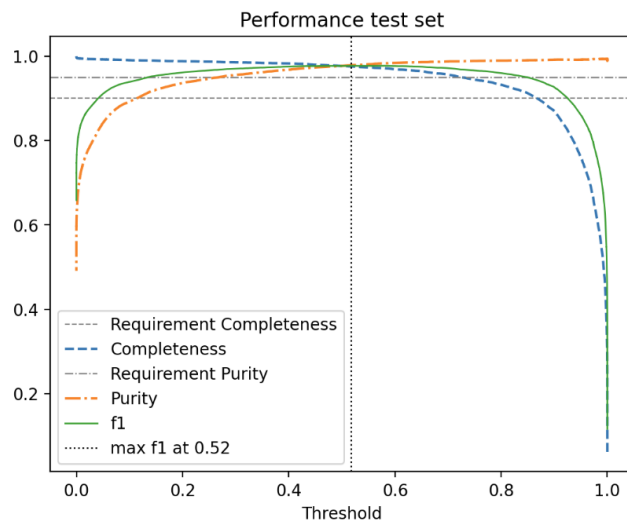


Figure 36. The purity and completeness of the reliability score is shown as a function of reliability threshold based on the testing data. A vertical line marks the threshold where the highest F1-score is obtained. The F1 score is the harmonic mean of completeness and purity. See §4.6.1 for details on the model and model training.

By analyzing the signed median residuals to search for biases, we find that previously-known objects have mean residuals of $0''.001$ and $-0''.016$ in the RA and Dec directions respectively, whereas newly-discovered objects have mean residuals of $-0''.035$ and $-0''.010$ in the RA and Dec directions, respectively. These mean residuals are small enough to eliminate the possibility of a timing offset greater than the second-scale shutter motion, which is consistent with the timing studies presented in §2.2.2.

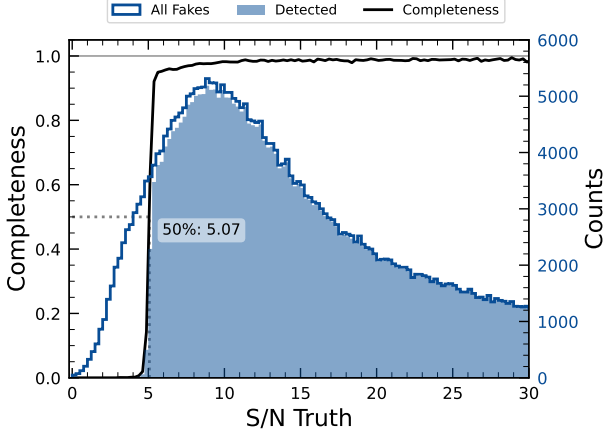


Figure 37. The difference image detection completeness for injected sources in the ECDFS field, for filters *griz*, as a function of the estimated signal to noise ratio SNR. This completeness is the ratio between the found fake sources (shaded histogram) and all the sources (solid line). The horizontal dashed line represents where the 50% completeness level is reached, at approximately $\text{SNR} \simeq 5.07$.

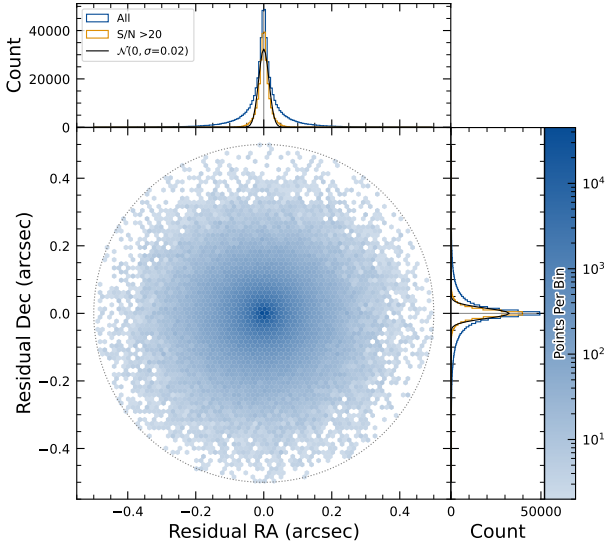


Figure 38. Coordinate residuals for detected synthetic sources in difference images, between recovered and true position of the sources in the ECDFS field. In the top and right panels we include the distribution of these offsets, for all sources as well as for sources with $\text{SNR} > 20$. These high SNR sources show gaussian coordinate residual distributions with $\sigma = 0''.02$ (black solid lines). The circle reflects the matching radius of $0''.5$.

The wider scatter in the RA residuals is due to objects whose measured orbital elements are less well con-

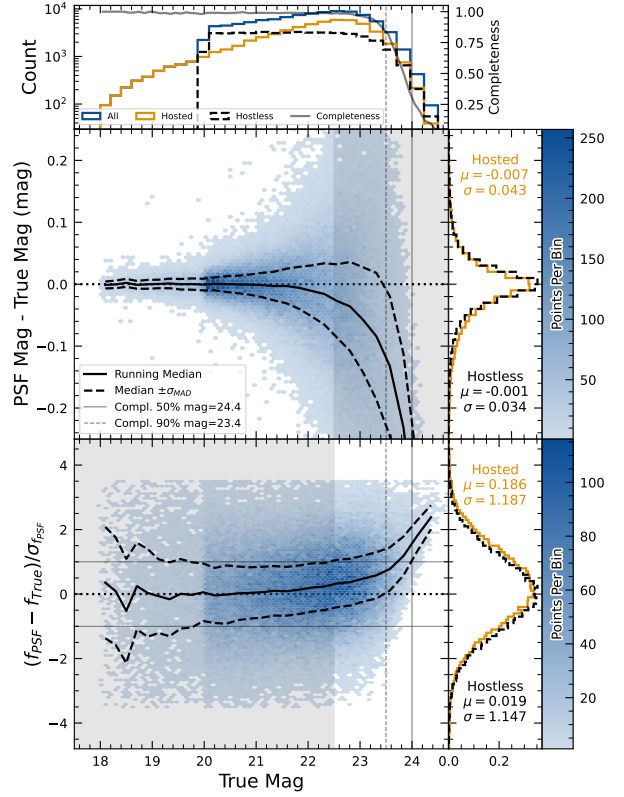


Figure 39. Magnitude residuals and flux pulls for *i*-band PSF photometry on difference images for ECDFS field in *i* for detected injected sources. Top panel: Distribution of true magnitudes for injected sources (blue), and split into hostless (black dash) and hosted (orange) sources, with detection completeness as a function of true magnitude (gray line). Vertical dashed lines indicate the 90% and 50% completeness magnitude limits. Center left panel: 2D hexbin plot of PSF magnitude residuals (measured minus true) versus true magnitude for detected sources, with running median (solid black) and σ_{MAD} (dashed black) overlaid. Center right panel: Marginalized distributions of PSF magnitude residuals for hostless (blue) and hosted (orange) sources with true magnitude $m_i < 22.5$, annotated with robust mean and standard deviation. Bottom left panel: 2D hexbin plot of PSF flux pulls versus true magnitude for detected sources, with running median (solid black) and σ_{MAD} (dashed black) overlaid. Bottom right panel: Marginalized distributions of PSF flux pulls for hostless (blue) and hosted (orange) sources with true magnitude $m_i < 22.5$, annotated with robust mean and standard deviation.

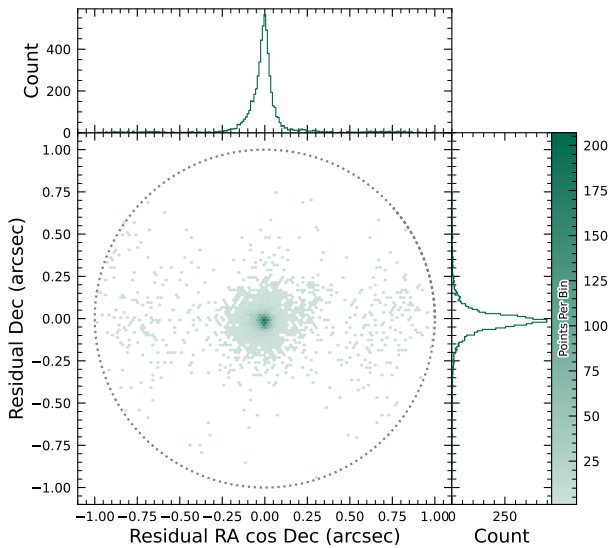


Figure 40. Astrometric residuals between expected and observed positions of Solar System Objects in DP1. The median residuals are $0''.001$ and $-0''.016$ in R.A./Dec direction, with standard deviations of $0''.19$ and $0''.10$, respectively. No detectable systematic offset from zero indicates there are no major errors in either timing or astrometry delivered by the Rubin system. The wider scatter in the RA direction is due to objects whose measured orbital elements are less well constrained, translating to larger along-track positional errors in the predicted positions.

strained, translating to larger along-track positional errors in the predicted positions. Observations of objects with large residuals are the most valuable ones from the point of view of improving the orbit, which is why we kept a generous matching radius. However, in future releases we are likely to couple this with either orbit fitting to verify the “singleton” match, or require two near-in-time observations (a tracklet) that match the expected motion vector as well.

Optimal moving source attribution is an area of active work that we expect to fully converge in time of Data Release 1 (DR1). In the meantime, for DP1 we’ve opted to start with simple, more easily understandable, criteria.

5.10. Crowded Fields

Among the seven Rubin DP1 target fields, two stand out for their severe stellar crowding: the globular cluster 47 Tucanae (47_Tuc) and the Fornax dwarf spheroidal galaxy (Fornax dSph). These fields were selected in part to stress-test the LSST Science Pipelines under high-density conditions. While both exhibit high stellar den-

sities, the nature and spatial extent of the crowding differ significantly.

47 Tuc presents extreme crowding across much of the field, encompassing its dense core and the eastern regions influenced by the Small Magellanic Cloud (SMC). This pervasive crowding leads to persistent challenges for deblending and reliable source detection, exposing field-wide limitations in the current pipeline performance (Y. Choi et al. 2025). In contrast, Fornax dSph shows significant crowding only in its central region, with outer areas remaining well resolved and easier to process.

In both 47 Tuc and Fornax, extreme crowding led to the deblending step being skipped frequently when memory or runtime limits were exceeded, typically due to an excessive number of peaks, or large parent footprints. However, the impact of these limitations differed: in 47 Tuc, deblending was often skipped across the entire field, resulting in large gaps and substantially reduced completeness. In Fornax, these issues were largely confined to the central region, with much better recovery in the outskirts. This contrast highlights how the pipeline’s limitations depend on the spatial extent of high-density regions: 47 Tuc exposed systematic, field-wide challenges, whereas Fornax revealed more localized, density-driven limits.

T. M. Wainer et al. (2025) explored the Rubin DP1 DiaObject catalog (§3.2) in the 47 Tuc field, which contains sources detected in difference images. Because forced photometry is performed at these positions across all single-epoch images, this dataset bypasses the coadd-based detection and deblending stages that often fail in crowded regions. By computing the median of the forced photometry for each DiaObject across available visits, they recovered approximately three times more candidate cluster members than found in the standard Object table (Y. Choi et al. 2025). This result underscores the value of difference-imaging-based catalogs for probing dense stellar regions inaccessible to standard coadd processing in DP1.

Although the DP1 pipeline was not optimized for crowded-field photometry, these early studies of 47 Tuc and Fornax provide critical benchmarks. They highlight both the limitations and opportunities for science with Rubin data in crowded environments, and they inform future pipeline development aimed at robust source recovery in complex stellar fields.

6. RUBIN SCIENCE PLATFORM

The RSP (M. Jurić et al. 2019) is a powerful, cloud-based environment for scientific research and analysis of petascale-scale astronomical survey data. It serves

as the primary interface for scientists to access, visualize, and conduct next-to-the-data analysis of Rubin and LSST data. The RSP is designed around a “bring the compute to the data” principle, eliminating the need for users to download massive datasets. Although DP1 is much smaller in size (3.5 TB) than many current survey datasets, future LSST datasets will be far larger and more complex, making it crucial to co-locate data and analysis for effective scientific discovery.

The RSP provides users with access to data and services through three distinct user-facing Aspects: a *Portal*, which facilitates interactive exploration of the data; a JupyterLab-based *Notebook* environment for data analysis using Python; and an extensive set of *Application Programming Interfaces (APIs)* that enable programmatic access to both data and services. The three Aspects are designed to be fully integrated, enabling seamless workflows across the RSP. The data products described in §3 are accessible via all three Aspects, and the system facilitates operations such as starting a query in one Aspect and retrieving its results in another. Figure 41 shows the Rubin Science Platform landing page in the Google cloud.

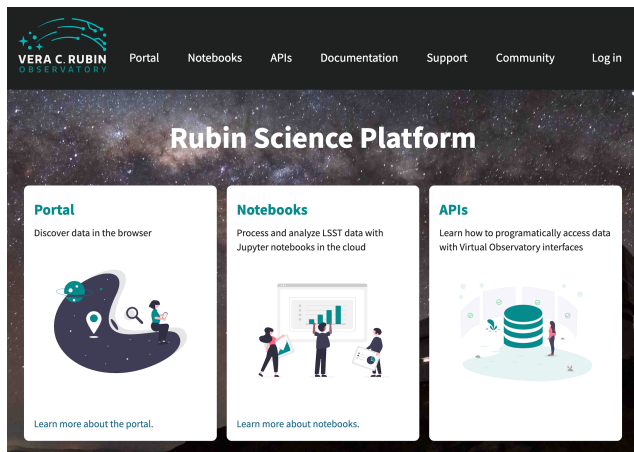


Figure 41. The Rubin Science Platform landing page at <https://data.lsst.cloud/> showing the three user-facing Aspects as well as links to documentation and support information.

The RSP is supported by a number of back-end services, including databases, files, and batch computing. Support for collaborative work through shared workspaces is also included in the RSP.

A preview of the RSP was launched on Google Cloud in 2022, operating under a shared-risk model to support Data Preview 0 (W. O’Mullane et al. 2024a). This allowed the community to test the platform, begin preparations for science, and provide valuable feedback to inform ongoing development. It was the first time an as-

tronomical research environment was hosted in a cloud environment. The DP1 release brings major updates to RSP services, enhancing scientific analysis capabilities. The RSP remains under active development, with incremental improvements being rolled out as they mature. During the Rubin Early Science Phase, the RSP will continue to operate under a shared-risk model. This section outlines the RSP functionality available at the time of the DP1 release and provides an overview of planned future capabilities.

6.1. Rubin Data Access Center

The Rubin US Data Access Center (US DAC) utilizes a novel hybrid on-premises-cloud architecture, which combines on-premises infrastructure at the USDF at SLAC with flexible and scalable resources in the Google cloud. This architecture has been deployed and tested using the larger simulated data set of DP0.2 (W. O’Mullane et al. 2024b).

In this hybrid model, user-facing services are deployed in the cloud to support dynamic scaling in response to user demand and to simplify the provisioning and management of large numbers of science user accounts. The majority of the static data products described in §3 are stored on-premises at the USDF to benefit from cost-effective mass storage and close integration with Rubin data processing infrastructure, also located at the USDF. For imaging data, the Data Butler (§6.2.2) provides the interface between the cloud-based users and data services, and the on-premises data. For catalog data, a cloud-based TAP client (§6.2.1) submits queries to the on-premises Qserv database cluster (§6.5) and retrieves the results. In the initial DP1 deployment, catalog data is hosted at the USDF while image data is stored in the cloud. The full hybrid model will be rolled out and further tested following the release of DP1. The RSP features a single-sign-on authentication and authorization system to provide secure access for Rubin data rights holders (R. Blum & the Rubin Operations Team 2020).

6.2. API Aspect

The API Aspect provides a comprehensive set of user-facing interfaces for programmatic access to the DP1 data products, through both IVOA-compliant services and the Rubin Data Butler. IVOA services enable standard queries and integration with existing tools, while the Butler facilitates advanced data processing within the LSST Science Pipelines.

At the time of the DP1 release, some IVOA services are unavailable, and certain data products are only accessible via the Butler. This section provides

an overview of the available *IVOA* services and Butler access.

6.2.1. *IVOA Services*

Rubin has adopted a *Virtual Observatory (VO)*-first design philosophy, prioritizing compliance with *IVOA* standard interfaces to foster interoperability, standardization, and collaboration. In cases where standardized protocols have yet to be established, additional services have been introduced to complement these efforts. This approach ensures that the RSP can be seamlessly integrated with community-standard tools such as *Tool for OPERations on Catalogues And Tables (TOPCAT)* (M. Taylor 2011) and *Aladin* (F. Bonnarel et al. 2000; T. Boch & P. Fernique 2014; M. Baumann et al. 2022), as well as libraries such as *PyVO* (M. Graham et al. 2014).

The user-facing *APIs* are also used internally within the RSP, creating a unified design that ensures consistent and reproducible workflows across all three Aspects. This reduces code duplication, simplifies maintenance, and ensures all users, both internal and external, access data in the same way. For example, an *Astronomical Data Query Language (IVOA standard) (ADQL)* query on the *Object* catalog via TAP yields identical results whether run from the Portal, Notebook, or an external client.

The following *IVOA* services are available at the time of the *DP1* release:

- **Table Access Protocol (TAP) Service:** A TAP service (P. Dowler et al. 2019) enables queries of catalog data via the *IVOA*-standard *ADQL*, a dialect of *SQL92* with spherical geometry extensions. The main TAP service for *DP1* runs on the Rubin-developed *Qserv* database (§ 6.5), which hosts the core science tables described in §3.2, as well as the Visit database. It also provides image metadata in the *IVOA ObsCore* format via the standard `ivoa.ObsCore` table, making it an “ObsTAP” service (ObsTAP; M. Louys et al. 2017). The TAP service is based on the *Canadian Astronomy Data Centre (CADC)*’s open-source Java TAP implementation¹⁰⁸, modified for the exact query language accepted by *Qserv*. It currently supports a large subset of *ADQL*, with limitations documented in the data release materials (see §7.1) and exposed via the TAP **capabilities** endpoint where possible.

The TAP service provides metadata annotations consistent with the standard, including table and

column descriptions, indications of foreign-key relationships between tables, and column metadata such as units and *IVOA* Unified Content Descriptors (UCDs).

- **Image Access Services:** Rubin image access services are compliant with *IVOA SIAv2* (Simple Image Access Protocol, version 2; T. Jenness et al. 2024; P. Dowler et al. 2015) for discovering and accessing astronomical images based on metadata. *SIAv2* is a *REpresentational State Transfer (REST)*-based protocol designed for the discovery and retrieval of image data. It allows, for instance, querying all images in a given band over a defined sky region and time period.

Users identify an image or observation of interest and query the service. The result set includes metadata about the image, such as the sky position, time, or band, and a data access URL, which includes an *IVOA* Identifier uniquely identifying the dataset (T. Jenness & G. P. Dubois-Felsmann 2025), allowing the dataset to be retrieved or a cutout requested via *Server-side Operations for Data Access (IVOA standard) (SODA)*.

- **Image Cutout Service:** The Rubin Cutout Service (R. Allbery 2023, 2024) is based on the *IVOA SODA* standard (F. Bonnarel et al. 2017). Users submit requests specifying sky coordinates and the cutout size as the radius from the coordinates, and the service performs the operation on the full image and returns a result set. For *DP1*, the cutout service is a single cutout service only where *N* cutout requests will require *N* independent synchronous calls. We expect some form of bulk cutout service by mid 2026.
- **HiPS Data Service:** An authenticated *HiPS* (P. Fernique et al. 2017) data service for seamless pan-and-zoom access to large-scale co-adds. It supports fast interactive progressive image exploration at a range of resolutions.
- **WebDAV:** A *Web Distributed Authoring and Versioning (WebDav)* service is provided to enable users to remotely manage, edit, and organize files and directories on the RSP as if they were local files on their own computer. This is especially useful for local development.

6.2.2. *Data Butler*

The Rubin Data Butler (T. Jenness et al. 2022; N. B. Lust et al. 2023), is a high-level interface designed to

¹⁰⁸ <https://github.com/opencadc/tap>

facilitate seamless access to data for both users and software systems. This includes managing storage formats, physical locations, data staging, and database mappings. A [Butler](#) repository contains two components:

- the *Data Store*: A physical storage system for datasets, e.g., a [Portable Operating System Interface \(POSIX\)](#) file system or S3 object store; and
- the *Registry*: An [Structured Query Language \(SQL\)](#)-compatible database that stores metadata about the datasets in the data store.

For DP1, the Butler repository is hosted in the Google Cloud, using an [\(Amazon\) Simple Storage Service \(S3\)](#)-compatible store for datasets and AlloyDB, a PostgreSQL-compatible database, for the registry.

In the context of the [Butler](#), a *dataset* refers to a unique data product, such as an image, catalog or map, generated by the observatory or processing pipelines. Datasets belong to one of the various types of data products, described in §3. The [Butler](#) ensures that each dataset is uniquely identifiable by a combination of three pieces of information: a data coordinate, a dataset type, and a run collection. For example, a dataset that represents a single raw image in the *i* band taken on the night starting 2024-11-11 with exposure ID 2024111100074 would be represented as `dataId='exposure':2024111100074, 'band':'i', 'instrument':'LSSTComCam'` and is associated with the `raw` DatasetType. For a deep coadd on a [patch](#) of sky in the Seagull field, there would be no exposure dimensions and instead the tract, [patch](#) and band would be specified as `dataId='tract':7850, 'patch':6, 'band':'g', 'instrument':'LSSTComCam', skymap='lsst_cells_v1'` and is associated with the `deep_coadd` DatasetType. The tract identification numbers and corresponding target names for these tracts are listed in [Table 7](#).

The data coordinate is used to locate a dataset in multi-dimensional space, where dimensions are defined in terms of scientifically meaningful concepts, such as instrument, visit, detector or band. For example, a calibrated single-visit image (§3.1) has dimensions including band, instrument, and detector. In contrast, the visit table (§3.2), a catalog of all calibrated single-epoch visits in DP1, has only the instrument dimension. The main dimensions used in DP1 are listed, together with a brief description, in [Table 8](#). To determine which dimensions are relevant for a specific dataset, the [Butler](#) defines dataset types, which associate each dataset with its specific set of relevant dimensions, as well as the associated Python type representing the dataset. The dataset

Table 7. Tract coverage of each DP1 field. The size of a tract is larger than the LSSTComCam field of view; however, since each observed field extends across more than one tract, each field covers multiple tracts.

Field Code	Tract ID
47_Tuc	453, 454
ECDFS	4848, 4849, 5062, 5063, 5064
EDFS_comcam	2234, 2235, 2393, 2394
Fornax_dSph	4016, 4017, 4217, 4218
Rubin_SV_095_-25	5305, 5306, 5525, 5526
Rubin_SV_38_7	10221, 10222, 10463, 10464, 10704, 10705
Seagull	7610, 7611, 7849, 7850

type defines the kind of data a dataset represents, such as a raw image (`raw`), a processed catalog (`object_forced_source`), or a sky map (`skyMap`). [Table 9](#) lists all the dataset types available via the Butler in DP1, together with the dimensions needed to uniquely identify a specific dataset and the number of unique datasets of each type.

It is important to highlight a key difference between accessing catalog data via the [TAP](#) service versus the Butler. While the [TAP](#) service contains entire catalogs, many of the same catalogs in the Butler are split into multiple separate catalogs. This is partly due to how these catalogs are generated, but also because of the way data is stored within and retrieved from the Butler repository – it is inefficient to retrieve the entire `Source` catalog, for example, from the file system. Instead, because the `Source` catalog contains data for sources detected in the `visit_images`, there is one `Source` catalog in the Butler for each `visit_image`. Similarly, there is one `Object` catalog for each `deep_coadd`. All the catalogs described in §3.2, aside from the `CcdVisit`, `SSObject`, `SSSource`, and `Calibration` catalogs, are split within the Butler.

A dataset is associated with one or more *Collections*; logical groupings of datasets within the Butler system that were created or processed together by the same batch operation. Collections allow multiple datasets with the same data coordinate to coexist without conflict. Collections support flexible, parallel processing by enabling repeated analyses of the same input data using different configurations. The DP1 Butler is read-only; a writable Butler is expected by mid-2026.

6.2.3. Remote Programmatic Access

The Rubin [RSP API](#) can be accessed from a local system by data rights holders outside of the [RSP](#), by creat-

Table 8. Descriptions of and valid values for the key data dimensions in DP1. YYYYMMDD signifies date and # signifies a single 0–9 digit.

Dimension	Format/Valid values	Description
day_obs	YYYYMMDD	A day and night of observations that rolls over during daylight hours.
visit	YYYYMMDD#####	A sequence of observations processed together; synonymous with “exposure” in DP1.
exposure	YYYYMMDD#####	A single exposure of all nine ComCam detectors.
instrument	LSSTComCam	The instrument name.
detector	0–8	A ComCam detector.
skymap	lsst_cells_v1	A set of tracts and patches that subdivide the sky into rectangular regions with simple projections and intentional overlaps.
tract	See Table 7	A large rectangular region of the sky.
patch	0–99	A rectangular region within a tract.
physical_filter	u_02, g_01, i_06, r_03, z_03, y_04	A physical filter.
band	u, g, r, i, z, y	An conceptual astronomical passband.

Table 9. The name and number of each type of data product in the Butler and the dimensions required to identify a specific dataset.

Data Product	Name in Butler	Required Dimensions	Number in DP1
Image Data Products			
raw	raw	instrument, detector, exposure	16125
visit_image	visit_image	instrument, detector, visit	15972
deep_coadd	deep_coadd	band, skymap, tract, patch	2644
template_coadd	template_coadd	band, skymap, tract, patch	2730
difference_image	difference_image	instrument, detector, visit	15972
Catalog Data Products			
Source	source	instrument, visit	1786
Object	object	skymap, tract	29
ForcedSource	object_forced_source	skymap, tract, patch	636
DiaSource	dia_source	skymap, tract	25
DiaObject	dia_object	skymap, tract	25
ForcedSourceOnDiaObject	dia_object_forced_source	skymap, tract, patch	597
SSSource	ss_source	–	1
SSObject	ss_object	–	1
Visit	visit_table	instrument	1
CcdVisit	visit_detector_table	instrument	1

ing a user security token. This token can then be used as a bearer token for [API](#) calls to the [RSP TAP](#) service. This capability is especially useful for remote data analysis using tools such as [TOPCAT](#), as well as enabling third-party systems, e.g., Community Alert Brokers, to access Rubin data. Additionally, it supports remote development, allowing for more flexible workflows and integration with external systems.

6.3. Portal Aspect

The Portal Aspect provides an interactive web-based environment for exploratory data discovery, filtering, querying, and visualization of both image and catalog data, without requiring programming expertise. It enables users to access and analyze large datasets via tools for catalog queries, image browsing, time-series inspection, and cross-matching.

The Portal is built on *Firefly* (X. Wu et al. 2019), a web application framework developed by the Infrared Processing and Analysis Center (IPAC). *Firefly* provides interactive capabilities such as customizable table views, image overlays, multi-panel visualizations, and synchronized displays linking catalog and image data.

Designed to support both exploratory data access and detailed scientific investigation, the Portal delivers an intuitive user experience, allowing users to visually analyze data while retaining access to underlying metadata and query controls.

6.4. Notebook Aspect

The Notebook Aspect provides an interactive, web-based environment built on Jupyter Notebooks, enabling users to write and execute Python code directly on Rubin and LSST data without downloading it locally. It offers programmatic access to Rubin and LSST data products, allowing users to query and retrieve datasets, manipulate and display images, compute derived properties, plot results, and reprocess data using the LSST Science Pipelines (§4.1). The environment comes pre-installed with the pipelines and a broad set of widely used astronomical software tools, supporting immediate and flexible data analysis.

6.5. Databases

The user-facing Aspects of the RSP are supported by several backend databases that store catalog data products, image metadata, and other derived datasets. The schema for DP1 and other Rubin databases are available online at <https://sdm-schemas.lsst.io>.

6.5.1. Qserv

The final 10-year LSST catalog is expected to reach 15 PB and contain measurements for billions of stars and galaxies across trillions of detections. To support efficient storage, querying, and analysis of this dataset, Rubin Observatory developed Qserv (D. L. Wang et al. 2011; F. Mueller et al. 2023) – a scalable, parallel, distributed SQL database system. Qserv partitions data over approximately equal-area regions of the celestial sphere, replicates data to ensure resilience and high availability, and uses shared scanning to reduce overall I/O load. It also supports a package of scientific user-defined functions (SciSQL: <https://smonkewitz.github.io/scisql/>) simplifying complex queries involving spherical geometry, statistics, and photometry. Qserv is built on robust production-quality components, including MariaDB (<https://www.mariadb.org/>) and XRootD (<https://xrootd.org/>). Qserv runs at the USDF and user access to catalog data is via the TAP service (§6.2.1).

This enables catalog-based analysis through both the RSP Portal and Notebook Aspects.

Although the small DP1 dataset does not require Qserv’s full capabilities, we nevertheless chose to use it for DP1 to accurately reflect the future data access environment and to gain experience with scientifically-motivated queries ahead of full-scale deployment. Qserv is open-source and available on GitHub: <https://github.com/lsst/qserv>.

7. SUPPORT FOR COMMUNITY SCIENCE

Rubin Observatory has a science community that encompasses thousands of individuals worldwide, with a broad range of experience and expertise in astronomy in general, and in the analysis of optical imaging data specifically.

Rubin’s model to support this diverse community to access and analyze DP1 emphasizes self-help via documentation and tutorials, and employs an open platform for asynchronous issue reporting that enables crowd-sourced solutions. These two aspects of community support are augmented by virtual engagement activities. In addition, Rubin supports its Users Committee to advocate on behalf of the science community, and supports the eight LSST Science Collaborations (§7.6).

All of the resources for scientists that are discussed in this section are discoverable by browsing the *For Scientists* pages of the Rubin Observatory website¹⁰⁹.

7.1. Documentation

The data release documentation for DP1¹¹⁰ provides an overview of the LSSTComCam observations, detailed descriptions of the data products, and a high-level summary of the processing pipelines. Although much of its content overlaps significantly with this paper, the documentation is presented as a searchable, web-based resource built using Sphinx¹¹¹, with a focus on enabling scientific use of the data products.

7.2. Tutorials

A suite of tutorials (NSF-DOE Vera C. Rubin Observatory 2021) that demonstrate how to access and analyze DP1 using the RSP accompanies the DP1 release¹¹². Jupyter Notebook tutorials are available via the “Tutorials” drop-down menu within the Notebook aspect of the RSP. Tutorials for the Portal and API aspects of the RSP can be found in the data release documentation.

¹⁰⁹ <https://rubinobservatory.org/for-scientists>

¹¹⁰ <https://dp1.lsst.io>

¹¹¹ <https://www.sphinx-doc.org/>

¹¹² <https://dp1.lsst.io/tutorials>

These tutorials are designed to be inclusive, accessible, clear, focused, and consistent. Their format and contents follow a set of guidelines (M. L. Graham et al. 2026) that are informed by modern standards in technical writing.

7.3. *Community Forum*

The venue for all user support is the Rubin Community Forum¹¹³. Questions about any and all aspects of the Rubin data products, pipelines, and services, including DP1, should be posted as new topics in the Support category. This includes beginner-level and “how-to” questions, advanced scientific analysis questions, technical bug reports, account and data access issues, and everything in between. The Support category of the Forum is monitored by Rubin staff, who follow an established internal workflow for following-up and resolving all reported issues.

The Rubin Community Forum is built on the open-source Discourse platform. It was chosen because, for a worldwide community of ten thousand Rubin users, a traditional (i.e., closed) help desk represents a risk to Rubin science (e.g., many users with the same question having to wait for responses). The open nature of the Forum enables self-help by letting users search for similar issues, and enables crowd-sourced problem solving (and avoids knowledge bottlenecks) by letting users help users.

The Rubin Community Forum, and the internal staff workflows for user support, were set up, tested, and refined with DP0 so that it was ready for use with DP1.

7.4. *Engagement Activities*

A variety of live virtual and in-person workshops and seminars offer learning opportunities to scientists and students working with the Rubin data products, services, and tools.

- Rubin Science Assemblies (weekly, virtual, 1 hour): alternates between hands-on tutorials based on the most recent data release and open drop-in “office hours” with Rubin staff.
- Rubin Data Academy (annual, virtual, 3-4 days): an intense set of hands-on tutorials based on the most recent data release, along with co-working and networking sessions.
- Rubin Community Workshop (annual, virtual, 5 days), a science-focused conference of contributed

posters, talks, and sessions led by members of the Rubin science community and Rubin staff.

Following the release of DP1, all of these engagement activities focused on use of DP1 by the science community. In particular, the 2025 Rubin Data Academy was run the week of the DP1 release, in order to immediately facilitate community access. The 2025 Rubin Community Workshop had several sessions to introduce people to the DP1 dataset and demonstrate how to access and analyze it with the RSP.

For schedules, connection information, zoom recordings, and associated materials, visit the *For Scientists* pages of the Rubin Observatory website¹¹⁴. Requests for custom tutorials and presentations for research groups are also accommodated.

7.5. *Users Committee*

This committee is charged with soliciting feedback from the science community, advocating on their behalf, and recommending science-driven improvements to the LSST data products and the Rubin Science Platform tools and services. Community members are encouraged to attend their virtual meetings and raise issues to their attention, so they can be included in the committee’s twice-yearly reports to the Rubin Observatory Director.

Like the Forum, the Users Committee was established and began its work with DP0, and that feedback was implemented for DP1. The community’s response to DP1 will be especially valuable input to DP2 and DR1, and the Users Committee encourages all users to interact with them. For a list of members and contact information, visit the *For Scientists* pages of the Rubin Observatory website.

7.6. *Science Collaborations*

The eight LSST Science Collaborations are independent, worldwide communities of scientists, self-organized into collaborations based on their research interests and expertise. Members work together to apply for funding, build software infrastructure and analysis algorithms, and incorporate external data sets into their LSST-based research.

The Science Collaborations also provide valuable advice to Rubin Observatory on the operational strategies and data products to accomplish specific science goals, and Rubin Observatory supports the collaborations via staff liaisons and regular virtual meetings with Rubin operations leadership.

¹¹³ <https://community.lsst.org/>

¹¹⁴ <https://rubinobservatory.org/for-scientists/events-deadlines>

The Science Collaborations have been functioning for many years, and their engagement and feedback on DP0 was implemented into the community science model for DP1, as it will for future data releases.

8. SUMMARY AND FUTURE RELEASES

Rubin Data Preview 1 offers an initial look at the first on-sky data products and access services from the Vera C. Rubin Observatory. DP1 forms part of Rubin’s Early Science Program, and provides the scientific community with an early opportunity to familiarize themselves with the data formats and access infrastructure for the forthcoming Legacy Survey of Space and Time. This early release has a proprietary period of two years, during which time it is available to Rubin data rights holders only via the cloud-based RSP.

In this paper we have described the completion status of the observatory at the time of data acquisition, the commissioning campaign that forms the basis of DP1, and the processing pipelines used to produce early versions of data products. We provide details on the data products, their characteristics and known issues, and describe the Rubin Science Platform for access to and analysis of DP1.

The data products described in this paper derive from observations obtained by LSSTComCam. LSSTComCam contains only around 5% the number of CCDs as the full LSST Science Camera (LSSTCam), yet the DP1 dataset that it has produced will already enable a very broad range of science. At 3.5 TB in size, DP1 covers a total area of $\sim 15 \text{ deg}^2$ and contains 1792 single-epoch images, 2644 deep coadded images and 2.3 million distinct astrophysical objects, including 93 new asteroid discoveries.

While some data products anticipated from the LSST are not yet available, e.g., cell-based coadds, DP1 includes several products that will not be provided in future releases. Notably, difference images are included in DP1 as pre-generated products; in future releases, these will instead be generated on demand via dedicated services. The inclusion of pre-generated difference images in DP1 is feasible due to the relatively small size of the dataset, an approach that will not scale to the significantly larger data volumes expected in subsequent releases.

The RSP is continually under development, and new functionality will continue to be deployed incrementally

as it becomes available, and independent of the future data release schedule. User query history capabilities, context-aware documentation and a bulk cutout services are just a few of the services currently under development.

Coincident with the release of DP1, Rubin Observatory begins its Science Validation Surveys with the LSST Science Camera (i.e., LSSTCam). This final commissioning phase will produce a dataset that will form the foundation for the second Rubin Data Preview, DP2. Full operations, marking the start of the LSST, are expected to commence in 2026.

ACKNOWLEDGMENTS

. This material is based upon work supported in part by the National Science Foundation through Cooperative Agreements AST-1258333 and AST-2241526 and Cooperative Support Agreements AST-1202910 and AST-2211468 managed by the Association of Universities for Research in Astronomy (AURA), and the Department of Energy under Contract No. DE-AC02-76SF00515 with the SLAC National Accelerator Laboratory managed by Stanford University. Additional Rubin Observatory funding comes from private donations, grants to universities, and in-kind support from LSST-DA Institutional Members.

This work has been supported by the French National Institute of Nuclear and Particle Physics (IN2P3) through dedicated funding provided by the National Center for Scientific Research (CNRS).

This work has been supported by STFC funding for UK participation in LSST, through grant ST/Y00292X/1.

Facilities: Rubin:Simonyi (LSSTComCam), Rubin:USDAC

Software: Rubin Data Butler (T. Jenness et al. 2022), LSST Science Pipelines (Rubin Observatory Science Pipelines Developers 2025), LSST Feature Based Scheduler v3.0 (P. Yoachim et al. 2024; E. Naghib et al. 2019) Astropy (Astropy Collaboration et al. 2013, 2018, 2022) PIFF (M. Jarvis et al. 2021), GBDES (G. M. Bernstein 2022), Qserv (D. L. Wang et al. 2011; F. Mueller et al. 2023), Slurm, HTCondor, CVMFS, FTS3, ESNset

APPENDIX

REFERENCES

- Abazajian, K., Adelman-McCarthy, J. K., Agüeros, M. A., et al. 2004, *AJ*, 128, 502, doi: [10.1086/421365](https://doi.org/10.1086/421365)
- Ahumada, R., Allende Prieto, C., Almeida, A., et al. 2020, *ApJS*, 249, 3, doi: [10.3847/1538-4365/ab929e](https://doi.org/10.3847/1538-4365/ab929e)
- Aihara, H., AlSayyad, Y., Ando, M., et al. 2022, *PASJ*, 74, 247, doi: [10.1093/pasj/psab122](https://doi.org/10.1093/pasj/psab122)
- Allbery, R. 2023, IVOA SODA implementation experience, SQuaRE Technical Note SQR-063, NSF-DOE Vera C. Rubin Observatory. <https://sqr-063.lsst.io/>
- Allbery, R. 2024, Draft IVOA SODA web service specification, SQuaRE Technical Note SQR-093, NSF-DOE Vera C. Rubin Observatory. <https://sqr-093.lsst.io/>
- AlSayyad, Y. 2018, Coaddition Artifact Rejection and CompareWarp, Data Management Technical Note DMTN-080, NSF-DOE Vera C. Rubin Observatory, doi: [10.71929/rubin/2583441](https://doi.org/10.71929/rubin/2583441)
- Ansel, J., Yang, E., He, H., et al. 2024, in 29th ACM International Conference on Architectural Support for Programming Languages and Operating Systems, Volume 2 (ASPLOS '24) (ACM), doi: [10.1145/3620665.3640366](https://doi.org/10.1145/3620665.3640366)
- Antilogus, P., Astier, P., Doherty, P., Guyonnet, A., & Regnault, N. 2014, *Journal of Instrumentation*, 9, C03048, doi: [10.1088/1748-0221/9/03/C03048](https://doi.org/10.1088/1748-0221/9/03/C03048)
- Astropy Collaboration, Robitaille, T. P., Tollerud, E. J., et al. 2013, *A&A*, 558, A33, doi: [10.1051/0004-6361/201322068](https://doi.org/10.1051/0004-6361/201322068)
- Astropy Collaboration, Price-Whelan, A. M., Sipőcz, B. M., et al. 2018, *AJ*, 156, 123, doi: [10.3847/1538-3881/aabc4f](https://doi.org/10.3847/1538-3881/aabc4f)
- Astropy Collaboration, Price-Whelan, A. M., Lim, P. L., et al. 2022, *ApJ*, 935, 167, doi: [10.3847/1538-4357/ac7c74](https://doi.org/10.3847/1538-4357/ac7c74)
- Baumann, M., Boch, T., Pineau, F.-X., et al. 2022, in *Astronomical Society of the Pacific Conference Series*, Vol. 532, *Astronomical Data Analysis Software and Systems XXX*, ed. J. E. Ruiz, F. Pierfederici, & P. Teuben, 7
- Bechtol, K., Sevilla-Noarbe, I., Drlica-Wagner, A., et al. 2025, arXiv e-prints, arXiv:2501.05739, doi: [10.48550/arXiv.2501.05739](https://doi.org/10.48550/arXiv.2501.05739)
- Berk, A., Anderson, G. P., Bernstein, L. S., et al. 1999, in *Society of Photo-Optical Instrumentation Engineers (SPIE) Conference Series*, Vol. 3756, *Optical Spectroscopic Techniques and Instrumentation for Atmospheric and Space Research III*, ed. A. M. Larar, 348–353, doi: [10.1117/12.366388](https://doi.org/10.1117/12.366388)
- Bernstein, G. M. 2022, gbdes: DECam instrumental signature fitting and processing programs,, *Astrophysics Source Code Library*, record ascl:2210.011 <http://ascl.net/2210.011>
- Bernstein, G. M., & Jarvis, M. 2002, *AJ*, 123, 583, doi: [10.1086/338085](https://doi.org/10.1086/338085)
- Bernstein, G. M., Armstrong, R., Plazas, A. A., et al. 2017, *PASP*, 129, 074503, doi: [10.1088/1538-3873/aa6c55](https://doi.org/10.1088/1538-3873/aa6c55)
- Bertin, E. 2011, in *Astronomical Society of the Pacific Conference Series*, Vol. 442, *Astronomical Data Analysis Software and Systems XX*, ed. I. N. Evans, A. Accomazzi, D. J. Mink, & A. H. Rots, 435
- Bianco, F. B., Ivezić, Ž., Jones, R. L., et al. 2022, *ApJS*, 258, 1, doi: [10.3847/1538-4365/ac3e72](https://doi.org/10.3847/1538-4365/ac3e72)
- Blum, R., & the Rubin Operations Team. 2020, Vera C. Rubin Observatory Data Policy, Data Management Operations Controlled Document RDO-013, NSF-DOE Vera C. Rubin Observatory. <https://ls.st/RDO-013>
- Boch, T., & Fernique, P. 2014, in *Astronomical Society of the Pacific Conference Series*, Vol. 485, *Astronomical Data Analysis Software and Systems XXIII*, ed. N. Manset & P. Forshay, 277
- Bonnarel, F., Dowler, P., Demleitner, M., Tody, D., & Dempsey, J. 2017, IVOA Server-side Operations for Data Access Version 1.0., IVOA Recommendation 17 May 2017 doi: [10.5479/ADS/bib/2017ivoa.spec.0517B](https://doi.org/10.5479/ADS/bib/2017ivoa.spec.0517B)
- Bonnarel, F., Fernique, P., Bienaymé, O., et al. 2000, *A&AS*, 143, 33, doi: [10.1051/aas:2000331](https://doi.org/10.1051/aas:2000331)
- Bosch, J., Armstrong, R., Bickerton, S., et al. 2018, *PASJ*, 70, S5, doi: [10.1093/pasj/psx080](https://doi.org/10.1093/pasj/psx080)
- Broughton, A., Utsumi, Y., Plazas Malagón, A. A., et al. 2024, *PASP*, 136, 045003, doi: [10.1088/1538-3873/ad3aa2](https://doi.org/10.1088/1538-3873/ad3aa2)
- Burke, D. L., Rykoff, E. S., Allam, S., et al. 2018, *AJ*, 155, 41, doi: [10.3847/1538-3881/aa9f22](https://doi.org/10.3847/1538-3881/aa9f22)
- Chambers, K. C., Magnier, E. A., Metcalfe, N., et al. 2016, arXiv e-prints, arXiv:1612.05560, doi: [10.48550/arXiv.1612.05560](https://doi.org/10.48550/arXiv.1612.05560)
- Choi, Y., Olsen, K. A. G., Carlin, J. L., et al. 2025, arXiv e-prints, arXiv:2507.01343, doi: [10.48550/arXiv.2507.01343](https://doi.org/10.48550/arXiv.2507.01343)
- de Vaucouleurs, G. 1948, *Annales d'Astrophysique*, 11, 247
- de Vaucouleurs, G. 1953, *MNRAS*, 113, 134, doi: [10.1093/mnras/113.2.134](https://doi.org/10.1093/mnras/113.2.134)
- Dowler, P., Bonnarel, F., & Tody, D. 2015, IVOA Simple Image Access Version 2.0., IVOA Recommendation 23 December 2015 doi: [10.5479/ADS/bib/2015ivoa.spec.1223D](https://doi.org/10.5479/ADS/bib/2015ivoa.spec.1223D)
- Dowler, P., Rixon, G., Tody, D., & Demleitner, M. 2019, Table Access Protocol Version 1.1., IVOA Recommendation 27 September 2019 doi: [10.5479/ADS/bib/2019ivoa.spec.0927D](https://doi.org/10.5479/ADS/bib/2019ivoa.spec.0927D)

- Eggl, S., Juric, M., Moeyens, J., & Jones, L. 2020, in AAS/Division for Planetary Sciences Meeting Abstracts, Vol. 52, AAS/Division for Planetary Sciences Meeting Abstracts, 211.01
- Esteves, J. H., Utsumi, Y., Snyder, A., et al. 2023, PASP, 135, 115003, doi: [10.1088/1538-3873/ad0a73](https://doi.org/10.1088/1538-3873/ad0a73)
- Euclid Collaboration, Romelli, E., Kümmel, M., et al. 2025, arXiv e-prints, arXiv:2503.15305, doi: [10.48550/arXiv.2503.15305](https://doi.org/10.48550/arXiv.2503.15305)
- Fagreluis, P., & Rykoff, E. S. 2025, Rubin Observatory Baseline Calibration Plan, Commissioning Technical Note SITCOMTN-086, NSF-DOE Vera C. Rubin Observatory, doi: [10.71929/rubin/2583850](https://doi.org/10.71929/rubin/2583850)
- Ferguson, P. S., Rykoff, E. S., Carlin, J. L., Saunders, C., & Parejko, J. K. 2025, The Monster: A reference catalog with synthetic ugrizy-band fluxes for the Vera C. Rubin observatory, Data Management Technical Note DMTN-277, NSF-DOE Vera C. Rubin Observatory, doi: [10.71929/rubin/2583688](https://doi.org/10.71929/rubin/2583688)
- Fernique, P., Allen, M. G., Boch, T., et al. 2015, A&A, 578, A114, doi: [10.1051/0004-6361/201526075](https://doi.org/10.1051/0004-6361/201526075)
- Fernique, P., Allen, M., Boch, T., et al. 2017, HiPS - Hierarchical Progressive Survey Version 1.0., IVOA Recommendation 19 May 2017 doi: [10.5479/ADS/bib/2017ivoa.spec.0519F](https://doi.org/10.5479/ADS/bib/2017ivoa.spec.0519F)
- Finkbeiner, D. P., Davis, M., & Schlegel, D. J. 1999, The Astrophysical Journal, 524, 867, doi: [10.1086/307852](https://doi.org/10.1086/307852)
- Fortino, W. F., Bernstein, G. M., Bernardinelli, P. H., et al. 2021, AJ, 162, 106, doi: [10.3847/1538-3881/ac0722](https://doi.org/10.3847/1538-3881/ac0722)
- Gaia Collaboration, Montegriffo, P., Bellazzini, M., et al. 2023a, A&A, 674, A33, doi: [10.1051/0004-6361/202243709](https://doi.org/10.1051/0004-6361/202243709)
- Gaia Collaboration, Vallenari, A., Brown, A. G. A., et al. 2023b, A&A, 674, A1, doi: [10.1051/0004-6361/202243940](https://doi.org/10.1051/0004-6361/202243940)
- Górski, K. M., Hivon, E., Banday, A. J., et al. 2005, ApJ, 622, 759, doi: [10.1086/427976](https://doi.org/10.1086/427976)
- Graham, A. W., & Driver, S. P. 2005, PASA, 22, 118, doi: [10.1071/AS05001](https://doi.org/10.1071/AS05001)
- Graham, M., Plante, R., Tody, D., & Fitzpatrick, M. 2014, PyVO: Python access to the Virtual Observatory,, Astrophysics Source Code Library, record ascl:1402.004
- Graham, M. L., Carlin, J. L., Adair, C. L., et al. 2026, Guidelines for User Tutorials, Technical Note RTN-045, NSF-DOE Vera C. Rubin Observatory, doi: [10.71929/rubin/2584020](https://doi.org/10.71929/rubin/2584020)
- Gray, B. 2025, find_orb: Orbit determination from observations, https://github.com/Bill-Gray/find_orb
- Guy, L. P., Bechtol, K., Bellm, E., et al. 2026, Rubin Observatory Plans for an Early Science Program, Technical Note RTN-011, NSF-DOE Vera C. Rubin Observatory, doi: [10.71929/rubin/2584021](https://doi.org/10.71929/rubin/2584021)
- Heinze, A., Eggl, S., Juric, M., et al. 2022, in AAS/Division for Planetary Sciences Meeting Abstracts, Vol. 54, AAS/Division for Planetary Sciences Meeting Abstracts, 504.04
- Heinze, A., Juric, M., & Kurlander, J. 2023, heliolineX: Open Source Solar System Discovery Software, <https://github.com/heliolineX/heliolineX>
- Hirata, C., & Seljak, U. 2003, MNRAS, 343, 459, doi: [10.1046/j.1365-8711.2003.06683.x](https://doi.org/10.1046/j.1365-8711.2003.06683.x)
- Holman, M. J., Payne, M. J., Blankley, P., Janssen, R., & Kuindersma, S. 2018, AJ, 156, 135, doi: [10.3847/1538-3881/aad69a](https://doi.org/10.3847/1538-3881/aad69a)
- Howard, J., Reil, K., Claver, C., et al. 2018, in Society of Photo-Optical Instrumentation Engineers (SPIE) Conference Series, Vol. 10700, Ground-based and Airborne Telescopes VII, ed. H. K. Marshall & J. Spyromilio, 107003D, doi: [10.1117/12.2312684](https://doi.org/10.1117/12.2312684)
- Illingworth, G., Magee, D., Bouwens, R., et al. 2016, arXiv e-prints, arXiv:1606.00841, doi: [10.48550/arXiv.1606.00841](https://doi.org/10.48550/arXiv.1606.00841)
- Ingraham, P., Fagreluis, P., Stubbs, C. W., et al. 2022, in Society of Photo-Optical Instrumentation Engineers (SPIE) Conference Series, Vol. 12182, Ground-based and Airborne Telescopes IX, ed. H. K. Marshall, J. Spyromilio, & T. Usuda, 121820R, doi: [10.1117/12.2630185](https://doi.org/10.1117/12.2630185)
- Ivezić, Ž., Kahn, S. M., Tyson, J. A., et al. 2019a, ApJ, 873, 111, doi: [10.3847/1538-4357/ab042c](https://doi.org/10.3847/1538-4357/ab042c)
- Ivezić, Ž., Kahn, S. M., Tyson, J. A., et al. 2019b, ApJ, 873, 111, doi: [10.3847/1538-4357/ab042c](https://doi.org/10.3847/1538-4357/ab042c)
- Jarvis, M., et al. 2021, Mon. Not. Roy. Astron. Soc., 501, 1282, doi: [10.1093/mnras/staa3679](https://doi.org/10.1093/mnras/staa3679)
- Jenness, T., & Dubois-Felsmann, G. P. 2025, IVOA Identifier Usage at the Rubin Observatory, Data Management Technical Note DMTN-302, NSF-DOE Vera C. Rubin Observatory, doi: [10.71929/rubin/2583848](https://doi.org/10.71929/rubin/2583848)
- Jenness, T., Voutsinas, S., Dubois-Felsmann, G. P., & Salnikov, A. 2024, arXiv e-prints, arXiv:2501.00544, doi: [10.48550/arXiv.2501.00544](https://doi.org/10.48550/arXiv.2501.00544)
- Jenness, T., Bosch, J. F., Salnikov, A., et al. 2022, in Society of Photo-Optical Instrumentation Engineers (SPIE) Conference Series, Vol. 12189, Software and Cyberinfrastructure for Astronomy VII, 1218911, doi: [10.1117/12.2629569](https://doi.org/10.1117/12.2629569)

- Jones, R. L., Yoachim, P., Ivezić, Ž., Neilsen Jr., E. H., & Ribeiro, T. 2021, Survey Strategy and Cadence Choices for the Vera C. Rubin Observatory Legacy Survey of Space and Time (LSST), Project Science Technical Note PSTN-051, NSF-DOE Vera C. Rubin Observatory, doi: [10.71929/rubin/2584084](https://doi.org/10.71929/rubin/2584084)
- Juric, M. 2025, mpsky: Multi-purpose sky catalog cross-matching, <https://github.com/mjuric/mpsky>
- Jurić, M., Ciardi, D., Dubois-Felsmann, G., & Guy, L. 2019, LSST Science Platform Vision Document, Systems Engineering Controlled Document LSE-319, NSF-DOE Vera C. Rubin Observatory, doi: [10.71929/rubin/2587242](https://doi.org/10.71929/rubin/2587242)
- Jurić, M., Axelrod, T. S., Becker, A. C., et al. 2023, Data Products Definition Document, Systems Engineering Controlled Document LSE-163, NSF-DOE Vera C. Rubin Observatory, doi: [10.71929/rubin/2587118](https://doi.org/10.71929/rubin/2587118)
- Kannawadi, A. 2025, Consistent galaxy colors with Gaussian-Aperture and PSF photometry, Data Management Technical Note DMTN-190, NSF-DOE Vera C. Rubin Observatory, doi: [10.71929/rubin/2583849](https://doi.org/10.71929/rubin/2583849)
- Kron, R. G. 1980, ApJS, 43, 305, doi: [10.1086/190669](https://doi.org/10.1086/190669)
- Kuijken, K. 2008, A&A, 482, 1053, doi: [10.1051/0004-6361:20066601](https://doi.org/10.1051/0004-6361:20066601)
- Lange, T., Nordby, M., Pollek, H., et al. 2024, in Society of Photo-Optical Instrumentation Engineers (SPIE) Conference Series, Vol. 13096, Ground-based and Airborne Instrumentation for Astronomy X, ed. J. J. Bryant, K. Motohara, & J. R. D. Vernet, 130961O, doi: [10.1117/12.3019302](https://doi.org/10.1117/12.3019302)
- Léget, P. F., Astier, P., Regnault, N., et al. 2021, A&A, 650, A81, doi: [10.1051/0004-6361/202140463](https://doi.org/10.1051/0004-6361/202140463)
- Lim, K.-T. 2023, Proposal and Prototype for Prompt Processing, Data Management Technical Note DMTN-219, NSF-DOE Vera C. Rubin Observatory, doi: [10.71929/rubin/2585429](https://doi.org/10.71929/rubin/2585429)
- Louys, M., Tody, D., Dowler, P., et al. 2017, Observation Data Model Core Components, its Implementation in the Table Access Protocol Version 1.1., IVOA Recommendation 09 May 2017 doi: [10.5479/ADS/bib/2017ivoa.spec.0509L](https://doi.org/10.5479/ADS/bib/2017ivoa.spec.0509L)
- LSST Dark Energy Science Collaboration (LSST DESC), Abolfathi, B., Alonso, D., et al. 2021, ApJS, 253, 31, doi: [10.3847/1538-4365/abd62c](https://doi.org/10.3847/1538-4365/abd62c)
- Lupton, R., Blanton, M. R., Fekete, G., et al. 2004, PASP, 116, 133, doi: [10.1086/382245](https://doi.org/10.1086/382245)
- Lust, N. B., Jenness, T., Bosch, J. F., et al. 2023, arXiv e-prints, arXiv:2303.03313, doi: [10.48550/arXiv.2303.03313](https://doi.org/10.48550/arXiv.2303.03313)
- Mandelbaum, R., Hirata, C. M., Seljak, U., et al. 2005, MNRAS, 361, 1287, doi: [10.1111/j.1365-2966.2005.09282.x](https://doi.org/10.1111/j.1365-2966.2005.09282.x)
- Megias Homar, G., Kahn, S. M., Meyers, J. M., Crenshaw, J. F., & Thomas, S. J. 2024, The Astrophysical Journal, 974, 108, doi: [10.3847/1538-4357/ad6cdc](https://doi.org/10.3847/1538-4357/ad6cdc)
- Megias Homar, G., Tighe, R., Thomas, S., et al. 2024, in Ground-based and Airborne Telescopes X, ed. H. K. Marshall, J. Spyromilio, & T. Usuda, Vol. 13094, International Society for Optics and Photonics (SPIE), 130943C, doi: [10.1117/12.3019031](https://doi.org/10.1117/12.3019031)
- Melchior, P., Moolekamp, F., Jerdee, M., et al. 2018, Astronomy and Computing, 24, 129, doi: [10.1016/j.ascom.2018.07.001](https://doi.org/10.1016/j.ascom.2018.07.001)
- Mueller, F., et al. 2023, in ASP Conf. Ser., Vol. TBD, ADASS XXXII, ed. S. Gaudet, S. Gwyn, P. Dowler, D. Bohlender, & A. Hincks (San Francisco: ASP), in press. <https://dmtn-243.lsst.io>
- Naghieb, E., Yoachim, P., Vanderbei, R. J., Connolly, A. J., & Jones, R. L. 2019, The Astronomical Journal, 157, 151, doi: [10.3847/1538-3881/aafece](https://doi.org/10.3847/1538-3881/aafece)
- NSF-DOE Vera C. Rubin Observatory. 2021, Rubin Observatory LSST Tutorials [Computer Software], NSF-DOE Vera C. Rubin Observatory, doi: [10.11578/rubin/dc.20250909.20](https://doi.org/10.11578/rubin/dc.20250909.20)
- NSF-DOE Vera C. Rubin Observatory. 2025a, Legacy Survey of Space and Time Data Preview 1 [Data set], NSF-DOE Vera C. Rubin Observatory, doi: [10.71929/RUBIN/2570308](https://doi.org/10.71929/RUBIN/2570308)
- NSF-DOE Vera C. Rubin Observatory. 2025b, Legacy Survey of Space and Time Data Preview 1: raw dataset type [Data set], NSF-DOE Vera C. Rubin Observatory, doi: [10.71929/RUBIN/2570310](https://doi.org/10.71929/RUBIN/2570310)
- NSF-DOE Vera C. Rubin Observatory. 2025c, Legacy Survey of Space and Time Data Preview 1: visit_image dataset type [Data set], NSF-DOE Vera C. Rubin Observatory, doi: [10.71929/RUBIN/2570311](https://doi.org/10.71929/RUBIN/2570311)
- NSF-DOE Vera C. Rubin Observatory. 2025d, Legacy Survey of Space and Time Data Preview 1: template_coadd dataset type [Data set], NSF-DOE Vera C. Rubin Observatory, doi: [10.71929/RUBIN/2570314](https://doi.org/10.71929/RUBIN/2570314)
- NSF-DOE Vera C. Rubin Observatory. 2025e, Legacy Survey of Space and Time Data Preview 1: difference_image dataset type [Data set], NSF-DOE Vera C. Rubin Observatory, doi: [10.71929/RUBIN/2570312](https://doi.org/10.71929/RUBIN/2570312)
- NSF-DOE Vera C. Rubin Observatory. 2025f, Legacy Survey of Space and Time Data Preview 1: Source searchable catalog [Data set], NSF-DOE Vera C. Rubin Observatory, doi: [10.71929/RUBIN/2570323](https://doi.org/10.71929/RUBIN/2570323)

- NSF-DOE Vera C. Rubin Observatory. 2025g, Legacy Survey of Space and Time Data Preview 1: Object searchable catalog [Data set], NSF-DOE Vera C. Rubin Observatory, doi: [10.71929/RUBIN/2570325](https://doi.org/10.71929/RUBIN/2570325)
- NSF-DOE Vera C. Rubin Observatory. 2025h, Legacy Survey of Space and Time Data Preview 1: ForcedSource searchable catalog [Data set], NSF-DOE Vera C. Rubin Observatory, doi: [10.71929/RUBIN/2570327](https://doi.org/10.71929/RUBIN/2570327)
- NSF-DOE Vera C. Rubin Observatory. 2025i, Legacy Survey of Space and Time Data Preview 1: DiaSource searchable catalog [Data set], NSF-DOE Vera C. Rubin Observatory, doi: [10.71929/RUBIN/2570317](https://doi.org/10.71929/RUBIN/2570317)
- NSF-DOE Vera C. Rubin Observatory. 2025j, Legacy Survey of Space and Time Data Preview 1: DiaObject searchable catalog [Data set], NSF-DOE Vera C. Rubin Observatory, doi: [10.71929/RUBIN/2570319](https://doi.org/10.71929/RUBIN/2570319)
- NSF-DOE Vera C. Rubin Observatory. 2025k, Legacy Survey of Space and Time Data Preview 1: ForcedSourceOnDiaObject searchable catalog [Data set], NSF-DOE Vera C. Rubin Observatory, doi: [10.71929/RUBIN/2570321](https://doi.org/10.71929/RUBIN/2570321)
- NSF-DOE Vera C. Rubin Observatory. 2025l, Legacy Survey of Space and Time Data Preview 1: SSOBJECT searchable catalog [Data set], NSF-DOE Vera C. Rubin Observatory, doi: [10.71929/RUBIN/2570335](https://doi.org/10.71929/RUBIN/2570335)
- NSF-DOE Vera C. Rubin Observatory. 2025m, Legacy Survey of Space and Time Data Preview 1: SSSource searchable catalog [Data set], NSF-DOE Vera C. Rubin Observatory, doi: [10.71929/RUBIN/2570333](https://doi.org/10.71929/RUBIN/2570333)
- NSF-DOE Vera C. Rubin Observatory. 2025n, Legacy Survey of Space and Time Data Preview 1: CcdVisit searchable catalog [Data set], NSF-DOE Vera C. Rubin Observatory, doi: [10.71929/RUBIN/2570331](https://doi.org/10.71929/RUBIN/2570331)
- NSF-DOE Vera C. Rubin Observatory. 2025o, Legacy Survey of Space and Time Data Preview 1: survey property dataset type [Data set], NSF-DOE Vera C. Rubin Observatory, doi: [10.71929/RUBIN/2570315](https://doi.org/10.71929/RUBIN/2570315)
- Oke, J. B., & Gunn, J. E. 1983, *ApJ*, 266, 713, doi: [10.1086/160817](https://doi.org/10.1086/160817)
- O'Mullane, W., Economou, F., Huang, F., et al. 2024a, in *Astronomical Society of the Pacific Conference Series*, Vol. 535, *Astronomical Data Analysis Software and Systems XXXI*, ed. B. V. Hugo, R. Van Rooyen, & O. M. Smirnov, 227, doi: [10.48550/arXiv.2111.15030](https://doi.org/10.48550/arXiv.2111.15030)
- O'Mullane, W., AlSaiyad, Y., Chiang, J., et al. 2024b, in *Society of Photo-Optical Instrumentation Engineers (SPIE) Conference Series*, Vol. 13101, *Software and Cyberinfrastructure for Astronomy VIII*, ed. J. Ibsen & G. Chiozzi, 131012B, doi: [10.1117/12.3018005](https://doi.org/10.1117/12.3018005)
- Onken, C. A., Wolf, C., Bessell, M. S., et al. 2019, *PASA*, 36, e033, doi: [10.1017/pasa.2019.27](https://doi.org/10.1017/pasa.2019.27)
- Park, H. Y., Nomerotski, A., & Tsybychev, D. 2017, *Journal of Instrumentation*, 12, C05015, doi: [10.1088/1748-0221/12/05/C05015](https://doi.org/10.1088/1748-0221/12/05/C05015)
- Petrosian, V. 1976, *ApJL*, 210, L53, doi: [10.1086/18230110.1086/182253](https://doi.org/10.1086/18230110.1086/182253)
- Plazas, A. A., Shapiro, C., Smith, R., Huff, E., & Rhodes, J. 2018, *Publications of the Astronomical Society of the Pacific*, 130, 065004, doi: [10.1088/1538-3873/aab820](https://doi.org/10.1088/1538-3873/aab820)
- Plazas Malagón, A. A., Digel, S. W., Roodman, A., et al. 2026, *LSSTCam and LSSTComCam Focal Plane Layouts*, Camera Technical Note CTN-001, NSF-DOE Vera C. Rubin Observatory, doi: [10.71929/rubin/2584019](https://doi.org/10.71929/rubin/2584019)
- Plazas Malagón, A. A., Waters, C., Broughton, A., et al. 2025, *Journal of Astronomical Telescopes, Instruments, and Systems*, 11, 011209, doi: [10.1117/1.JATIS.11.1.011209](https://doi.org/10.1117/1.JATIS.11.1.011209)
- Porter, M. N., Tucker, D. L., Smith, J. A., & Adair, C. L. 2026, *Photometric Transformation Relations for the LSST Data Preview 1*, Technical Note RTN-099, NSF-DOE Vera C. Rubin Observatory, doi: [10.71929/rubin/3006074](https://doi.org/10.71929/rubin/3006074)
- Refregier, A. 2003, *ARA&A*, 41, 645, doi: [10.1146/annurev.astro.41.111302.102207](https://doi.org/10.1146/annurev.astro.41.111302.102207)
- Reiss, D. J., & Lupton, R. H. 2016, *Implementation of Image Difference Decorrelation*, Data Management Technical Note DMTN-021, NSF-DOE Vera C. Rubin Observatory, doi: [10.71929/rubin/2586490](https://doi.org/10.71929/rubin/2586490)
- Roodman, A., Rasmussen, A., Bradshaw, A., et al. 2024, in *Society of Photo-Optical Instrumentation Engineers (SPIE) Conference Series*, Vol. 13096, *Ground-based and Airborne Instrumentation for Astronomy X*, ed. J. J. Bryant, K. Motohara, & J. R. D. Vernet, 130961S, doi: [10.1117/12.3019698](https://doi.org/10.1117/12.3019698)
- Rubin, V. C., & Ford, Jr., W. K. 1970, *ApJ*, 159, 379, doi: [10.1086/150317](https://doi.org/10.1086/150317)
- Rubin, V. C., Ford, Jr., W. K., & Thonnard, N. 1980, *ApJ*, 238, 471, doi: [10.1086/158003](https://doi.org/10.1086/158003)
- Rubin Observatory Science Pipelines Developers. 2025, *The LSST Science Pipelines Software: Optical Survey Pipeline Reduction and Analysis Environment*, Project Science Technical Note PSTN-019, NSF-DOE Vera C. Rubin Observatory, doi: [10.71929/rubin/2570545](https://doi.org/10.71929/rubin/2570545)
- Rubin's Survey Cadence Optimization Committee, Bauer, F. E., Brough, S., et al. 2022, *Survey Cadence Optimization Committee's Phase 1 Recommendation*, Project Science Technical Note PSTN-053, NSF-DOE Vera C. Rubin Observatory, doi: [10.71929/rubin/2584276](https://doi.org/10.71929/rubin/2584276)

- Rubin's Survey Cadence Optimization Committee, Bauer, F. E., Bianco, F. B., et al. 2023, Survey Cadence Optimization Committee's Phase 2 Recommendations, Project Science Technical Note PSTN-055, NSF-DOE Vera C. Rubin Observatory, doi: [10.71929/rubin/2585249](https://doi.org/10.71929/rubin/2585249)
- Rubin's Survey Cadence Optimization Committee, Bianco, F. B., Jones, R. L., et al. 2025, Survey Cadence Optimization Committee's Phase 3 Recommendations, Project Science Technical Note PSTN-056, NSF-DOE Vera C. Rubin Observatory, doi: [10.71929/rubin/2585402](https://doi.org/10.71929/rubin/2585402)
- Rykoff, E. S., Tucker, D. L., Burke, D. L., et al. 2023, arXiv e-prints, arXiv:2305.01695, doi: [10.48550/arXiv.2305.01695](https://doi.org/10.48550/arXiv.2305.01695)
- Saunders, C. 2024, Astrometric Calibration in the LSST Pipeline, Data Management Technical Note DMTN-266, NSF-DOE Vera C. Rubin Observatory, doi: [10.71929/rubin/2583846](https://doi.org/10.71929/rubin/2583846)
- Schutt, T., Jarvis, M., Roodman, A., et al. 2025, The Open Journal of Astrophysics, 8, 26, doi: [10.33232/001c.132299](https://doi.org/10.33232/001c.132299)
- Sérsic, J. L. 1963, Boletín de la Asociación Argentina de Astronomía La Plata Argentina, 6, 41
- Sersic, J. L. 1968, Atlas de Galaxias Australes (Cordoba, Argentina: Observatorio Astronomico)
- Shanks, T., Metcalfe, N., Chehade, B., et al. 2015, MNRAS, 451, 4238, doi: [10.1093/mnras/stv1130](https://doi.org/10.1093/mnras/stv1130)
- SLAC National Accelerator Laboratory, & NSF-DOE Vera C. Rubin Observatory. 2024, LSST Commissioning Camera, SLAC National Accelerator Laboratory (SLAC), Menlo Park, CA (United States), doi: [10.71929/RUBIN/2561361](https://doi.org/10.71929/RUBIN/2561361)
- Slater, C. T., Ivezić, Ž., & Lupton, R. H. 2020, AJ, 159, 65, doi: [10.3847/1538-3881/ab6166](https://doi.org/10.3847/1538-3881/ab6166)
- Smith, G. E. 2010, Rev. Mod. Phys., 82, 2307, doi: [10.1103/RevModPhys.82.2307](https://doi.org/10.1103/RevModPhys.82.2307)
- Stalder, B., Reil, K., Claver, C., et al. 2020, in Society of Photo-Optical Instrumentation Engineers (SPIE) Conference Series, Vol. 11447, Ground-based and Airborne Instrumentation for Astronomy VIII, ed. C. J. Evans, J. J. Bryant, & K. Motohara, 114470L, doi: [10.1117/12.2561132](https://doi.org/10.1117/12.2561132)
- Stalder, B., Reil, K., Aguilar, C., et al. 2022, in Society of Photo-Optical Instrumentation Engineers (SPIE) Conference Series, Vol. 12184, Ground-based and Airborne Instrumentation for Astronomy IX, ed. C. J. Evans, J. J. Bryant, & K. Motohara, 121840J, doi: [10.1117/12.2630184](https://doi.org/10.1117/12.2630184)
- Stalder, B., Munoz, F., Aguilar, C., et al. 2024, in Society of Photo-Optical Instrumentation Engineers (SPIE) Conference Series, Vol. 13094, Ground-based and Airborne Telescopes X, ed. H. K. Marshall, J. Spyromilio, & T. Usuda, 1309409, doi: [10.1117/12.3019266](https://doi.org/10.1117/12.3019266)
- Swinbank, J. D., Axelrod, T. S., Becker, A. C., et al. 2020, Data Management Science Pipelines Design, Data Management Controlled Document LDM-151, NSF-DOE Vera C. Rubin Observatory, doi: [10.71929/rubin/2587108](https://doi.org/10.71929/rubin/2587108)
- Taranu, D. S. 2025, The MultiProFit astronomical source modelling code, Data Management Technical Note DMTN-312, NSF-DOE Vera C. Rubin Observatory, doi: [10.71929/rubin/2584108](https://doi.org/10.71929/rubin/2584108)
- Taylor, M. 2011, TOPCAT: Tool for OPERations on Catalogues And Tables,, Astrophysics Source Code Library, record ascl:1101.010
- Thomas, S., Connolly, A., Crenshaw, J. F., et al. 2023, in Adaptive Optics for Extremely Large Telescopes (AO4ELT7), 67, doi: [10.13009/AO4ELT7-2023-069](https://doi.org/10.13009/AO4ELT7-2023-069)
- Tonry, J. L., Denneau, L., Heinze, A. N., et al. 2018, PASP, 130, 064505, doi: [10.1088/1538-3873/aabadf](https://doi.org/10.1088/1538-3873/aabadf)
- Wainer, T. M., Davenport, J. R. A., Bellm, E. C., et al. 2025, Research Notes of the American Astronomical Society, 9, 171, doi: [10.3847/2515-5172/adecef](https://doi.org/10.3847/2515-5172/adecef)
- Wang, D. L., Monkewitz, S. M., Lim, K.-T., & Becla, J. 2011, in State of the Practice Reports, SC '11 (New York, NY, USA: ACM), 12:1–12:11, doi: [10.1145/2063348.2063364](https://doi.org/10.1145/2063348.2063364)
- Waters, C. Z., Magnier, E. A., Price, P. A., et al. 2020, ApJS, 251, 4, doi: [10.3847/1538-4365/abb82b](https://doi.org/10.3847/1538-4365/abb82b)
- Whitaker, K. E., Ashas, M., Illingworth, G., et al. 2019, ApJS, 244, 16, doi: [10.3847/1538-4365/ab3853](https://doi.org/10.3847/1538-4365/ab3853)
- Wu, X., Roby, W., Goldian, T., et al. 2019, in Astronomical Society of the Pacific Conference Series, Vol. 521, Astronomical Data Analysis Software and Systems XXVI, ed. M. Molinaro, K. Shortridge, & F. Pasian, 32
- Xin, B., Claver, C., Liang, M., et al. 2015, ApOpt, 54, 9045, doi: [10.1364/AO.54.009045](https://doi.org/10.1364/AO.54.009045)
- Yoachim, P. 2022, Survey Strategy: Rolling Cadence, Project Science Technical Note PSTN-052, NSF-DOE Vera C. Rubin Observatory, doi: [10.71929/rubin/2584109](https://doi.org/10.71929/rubin/2584109)
- Yoachim, P., Jones, L., Eric H. Neilsen, J., & Becker, M. R. 2024, lsst/rubin_scheduler: v3.0.0, v3.0.0 Zenodo, doi: [10.5281/zenodo.13985198](https://doi.org/10.5281/zenodo.13985198)
- Zhang, T., Almoubayyed, H., Mandelbaum, R., et al. 2023, MNRAS, 520, 2328, doi: [10.1093/mnras/stac3350](https://doi.org/10.1093/mnras/stac3350)